INVESTIGATING THE ORIGINS OF LONG PERSISTENCE IN STRONTIUM ALUMINATE PHOSPHORS BY NANOSCALE RESOLVED IMAGING AND SPECTROSCOPY

by

GÜLİZ İNAN AKMEHMET

Submitted to the Graduate School of Engineering and Natural Sciences
in partial fulfillment of
the requirements for the degree of
Doctor of Philosophy

Sabancı University

Spring 2015

INVESTIGATING THE ORIGINS OF LONG PERSISTENCE IN STRONTIUM ALUMINATE PHOSPHORS BY NANOSCALE RESOLVED IMAGING AND SPECTROSCOPY

APPROVED BY:

Assoc. Prof. Dr. Cleva Ow-Yang.....
(Thesis Supervisor)

Assoc. Prof. Dr.Mehmet Ali Gülgün.....

Assoc. Prof. Dr Saso Sturm .....

Assoc. Prof. Dr. Burç Mısırlıoğlu.....

Prof. Dr.Ender Suvacı.....

DATE OF APPROVAL: 28/07/2015

INVESTIGATING THE ORIGINS OF LONG PERSISTENCE IN STRONTIUM ALUMINATE PHOSPHORS BY NANOSCALE RESOLVED IMAGING AND SPECTROSCOPY

GÜLİZ İNAN AKMEHMET

MAT, Doctor of Philosophy Thesis, 2015

Thesis Advisor: Assoc. Prof Cleva Ow-Yang

Keywords: Strontium Aluminate Phosphors, Scanning Transmission Electron Microscopy, Long Persistence, Nano-Scale Annular Dark/Bright Field Imaging, Boron.

Abstract

With a remarkable capacity to temporarily store and release light, long persistence phosphors are an exciting material for energy-saving applications. The objective of this work is to elucidate the role of B in dramatically extending persistence in strontium aluminate doped with Eu, Dy from the order of minutes to > 8 hours. Previous work neglected nanoscale effects. Computational models and experimental evidence, limited to indirect, global analysis, suggested that the extended afterglow may be due to the clustering of ionic point defects, although the results are inconclusive. However, in recognizing that high spatial resolution techniques of transmission electron microscopy (TEM) offer a game-changing advantage for localized analysis, this dissertation is devoted to the application of techniques with spatial resolution at the nanoscale and atomic scale for correlating the material structure with optical properties.

To set the stage, the processing of ceramic phosphor powders by a modified Pechini process was methodically studied. After global characterization of the powder structure optical properties, we have defined the atomic resolution TEM experimental techniques and simulation tools that will be necessary for quantitatively elucidating the defect clustering model. Our key results demonstrate that B, entering the compound in trigonal coordination, facilitates dominance of the long persistence $Sr_4Al_{14}O_{25}$ phase in the developing microstructure and promotes a more uniform distribution of divalent Eu onto the Sr sub-lattice. With such unprecedented correlation between structure and optical properties at the nanoscale, our results invite revision to existing models of persistence in strontium aluminate phosphors.

STRONSİYUM ALÜMİNAT FOSFORLARINDA ISRARLI-IŞILDAMANIN KÖKENLERİNİN NANO-ÖLÇEK ÇÖZÜNÜRLÜKTE GÖRÜNTÜLEME VE SPEKTROSKOPİ YOLUYLA İNCELENMESİ

GÜLİZ İNAN AKMEHMET

MAT, Doktora Tezi, 2015

Tez Danışmanı: Doç. Dr. Cleva Ow-Yang

Anahtar Kelimeler: Stronsiyum Alüminat Fosforlar, Geçirimli Taramalı Elektron Mikroskobu, Israrlı-ışıldama, Nano-ölçekte Anüler Karanlık/Aydınlık Alan Görüntüleme, Bor.

Özet

Israrlı-ışıldama sergileyen fosforlar ışığı geçici olarak depolama ve yayma özellikleri sayesinde enerji tasarruf uygulamalarında kullanılabilecek malzemelerdir. Bu çalışmanın hedefi, Eu ve Dy katkılı stronsiyum aluminat bileşiklerinde dakikalarla sınırlı olan ısrarlı-ışıldama süresinin borun eklenmesiyle birlikte 8 saatten uzun sürelere ulaşması ve borun bu olguya etkisini aydınlatmaya çalışmaktır. Önceki çalışmalar nano-ölçekteki etkileri gözardı etmiştir. Deneysel ve sayısal modellemelerden elde edilen dolaylı ve global analizlere dayalı kanıtlar, uzatılmış fosfor-ışıllığın iyonik nokta hatalara dayandığını önermekte ancak sonuçlar açıklamaya yetersiz kalmıştır. Ancak, geçirimli elektron mikroskobunun sunduğu yüksek uzaysal çözünürlük teknikleri, bu tezin üzerine adanmış olduğu nano-ölçek ve atomik-ölçekte çözünürlük sağlayan teknikler kullanılması, yapısal ve optik özelliklerin birbiriyle ilişkilendirilmesini sağlayarak bölgesel analiz anlamında ezber bozan avantajlar sunmaktadır.

Seramik tozların modifiye Pechini süreciyle sentezlenmesi metodik bir şekilde çalışılmış ve çalışmanın zemini oluşturulmuştur. Tozların yapsının ve optik özelliklerinin global karakterizasyonu sonrasında, hata kümelenmesi modelini nicel olarak değerlendirmek için

gerekli olan atomik çözünürlükte deneysel TEM teknikleri ve simülasyon araçlarını belirledik. Elde edilen ana sonuçların göstermiş olduğu üzere, bor bileşiğin yapısına trigonal koordinasyon yaparak yerleşmekte, uzun ısrarlı-ışıldama sergileyen Sr4Al14O25 fazının oluşmakta olan mikroyapıda baskın olmasına yardımcı olmakta ve Sr yerine yerleşen iki değerlikli Eu iyonunun daha homojen bir şekilde mikroyapıda dağılmasını teşvik etmektedir. Nano ölçekte gözlenen yapısal ve optik özellikler arasında eşi görülmemiş bir ilişki olduğunu ortaya çıkaran sonuçlarımız, stronsiyum alüminat fosforlarında görülen ısrarlı-ışıldama oluşumunu açıklayan mevcut modellerin gözden geçirilmesi gerekliliğine işaret etmektedir.

ACKNOWLEDGEMENTS

I would like to thank all those people who made this thesis possible by supporting and encouring me for the last couple of years.

First of all, I would like thank my advisor, mentor Cleva Ow-Yang for her endless support and guidance throughout my doctoral journey. I am deeply grateful to her for taking care every detail inhesitantly and with absolutely great care. I have learned a lot from her through these years, and I appreciate it deeply. I consider myself lucky to meet her and to work with her. It has been a joy to know her as a person and a privilige to be her PhD student.

I would like thank Mehmet Ali Gülgün (Mali) Hoca for his useful advices and insightful discussions about science and life. He has such a cheerful sense of humour which made everybody around him instantly smile. I hope that he would never lose his enthusiasm and joy in life. He has been a great teacher to me, I am grateful.

I would like to thank Saso Sturm, for his great support during the course of my thesis. I am grateful to him for putting up with my endless questions and e-mails. He never avoided his help, quite the contrary he was always very open and instructive. I am grateful to him for his helpfulness.

I also would like to thank my thesis comitee members, Burç Mısırlıoğlu and Ender Suvacı for their insightful comments and critics which helped me to improve this work further.

I'm grateful to Turgay Gönül, who has brought positive energy and motivation since the first time he arrived. Knowing that he would be in the lab to help, to discuss work, and even daily concerns, have always been a motivation for me and I have learned a lot from him. His enthusiasm will be always be an inspiration to me.

I would like to thank Meltem Sezen and Bojan Ambrozic for spending hours to prepare us excellent FIB specimens, I'm more than grateful.

I would like to thank Mustafa Atilla Yazıcı and Özge Berber for helping me with the ICP analysis. I am thankful to them for being so helpful.

I would like to thank Bahadır Barut from IC for helping us to find the unreacheable papers and books instantly. I also would like to thank Onur Kanyılmaz and Nilüfer Coşkuner from project office for their helps.

I would like to thank my group members Sirous, Ali and Hasan for their friendship and insightfull discussions.

I have made many good friends here; Murat Eskin, Melike Mercan Yıldızhan, Ece Alpaslan, Hasan Kurt, Gülcan Çorapcıoğlu, Canhan Şen, Mustafa Baysal, Ezgi Dündar Tekkaya, Tuğçe Akkaş, Meltem Sezen, Feray Bakan, Shalima Shawuti and many others. I am thankful to each of them for making these years enjoyable with their support and friendship. I would like thank especially to my dear friend Ayça Ürkmez for her friendship and support. She embesllished the time I had spent here in Sabanci. I'm so glad to meet her. Although I did not name each of them here, I thank all my friends in Sabanci for bringing good memories to my life.

I would like to thank all SU MAT family for accepting me as a member of their family.

I especially thank my mom, dad, and sister. They gave me unconditional love and support throughout my life and I can't thank them enough. My sister and my friend, Melis who always supported me and believed in me even at times I didn't, I'm grateful.

I'm most grateful to my best friend, my husband Celal, who motivated me with his support and love through these years. I'm so grateful to him for being very calm, understanding even at times I'm the opposite. He is the person who motivated me and encouraged me to start a career in academia. I am such a lucky person to meet him, and share my life with him, and I love him deeply.

Finally, I would like to acknowledge TÜBİTAK (project no 212T177, 112M360) for funding this work.

TABLE OF CONTENTS

LIST OF FIGURES

LIST OF TABLES

LIST OF ABBREVIATIONS

ABF	Annular Bright Field
ADF	Annular Dark Field
AGG	Abnormal Grain Growth
Al	Aluminium
Ar	Argon
AR-STEM	Atomically Resolved Scanning Transmission Electron Microscope
B	Boron
CL	Cathodoluminescence
DP	Diffraction Pattern
DTA	Differential Thermal Analysis
Dy	Dysprosium
DW	Debye-Waller
EDXS	Energy Dispersive X-ray Spectroscopy
EELS	Electron Energy Loss Spectroscopy
ELNES	Energy Loss Near Edge Spectrum
Eu	Europium
FIB	Focused Ion Beam
HAADF	High Angle Annular Dark Field
HRTEM	High Resolution Transmission Electron Microscope
ICP-OES	Inductively Coupled Optical Emission Spectroscopy
ICDD	International Centre forl Diffraction Data
ICSD	Inorganic Crystal Structure Database
JEMS	Java Electron Microscopy Software
O	Oxygen
PL	Photoluminescence
QSTEM	Quantitative TEM/STEM Simulations

RGB	Red, Blue, Green Additive Color Mixing
ROI	Region of Interest
SA phosphors	Strontium Aluminate phosphors
S_xA_yEDB	Strontium Aluminate co-doped with Europium and Dysprosium with Boron
SA	$SrAl_2O_4$
SA_2	$SrAl_4O_7$
SA6	$SrAl_{12}O_{19}$
S_4A_7	$Sr_4Al_{14}O_{25}$
SAEDP	Selected Area Electron Diffraction Pattern
SEM	Scanning Electron Microscope
STEM	Scanning Transmission Electron Microscope
TEM	Transmission Electron Microscope
TDS	Thermal Diffuse Scattering
TG	Thermogravimetry
XRD	X-Ray Diffraction
ZA	Zone Axis

LIST OF SYMBOLS

at%	Atomic Percentage
C_S	Astigmatism
C_C	Coma
min	Minutes
mrad	Miliradian
mol%	Mole Percentage
nm	Nanometer
ppm	Parts Per Million
Rexp	Expected R-factor
Rwp	Weighted Profile R-factor
wt%	Weight Percentage
Å	Ångstrom
°C	Celsius Degrees
τ	Afteglow Decay Lifetime

CHAPTER 1:

MOTIVATION FOR INVESTIGATING THE ORIGINS OF LONG PERSISTENCE IN STRONTIUM ALUMINATE PHOSPHORS BY NANOSCALE RESOLVED IMAGING AND SPECTROSCOPY

Strontium aluminate compounds (SA) serve as efficient and stable long persistence host materials, when co-doped with Eu^{2+} and Dy^{3+} rare earth metals[1-3]. As the Eu ion incorporates into the SA host lattice, it is an optically active center and luminesces in the visible region upon UV excitation[4]; doping with Dy ions further extends luminescence duration to the order of minutes.[5] Several mechanisms have been proposed to explain the afterglow mechanism in Eu^{2+}, Dy^{3+} co-doped strontium aluminates. The first model proposed by Matsuzawa[1] showed that Dy^{3+} in sufficient spatial proximity assisted the delay in de-excitation, subsequently numerous groups attempted to clarify the role of Dy and B. Although, the mechanism behind the extremely long afterglow of B-doped SA has yet to be fully understood, the most widely accepted mechanism of extended persistence was ionic defect aggregation—of rare-earth co-dopants, oxygen vacancy assisted trap level formation

in cation (Sr) sub-lattice, and B induced point defects.[6-9] This model presumes sufficient spatial and energetic proximity between trap levels (formed by oxygen vacancy defects, for example) for obtaining direct energy transfer between energy levels. Because computational models suggest that the clustering of point defects may be a necessary condition for persistent luminescence in the boron-doped SAED phosphors, the goal of this dissertation work is to investigate the correlation between the distribution of the ionic defects and the nature of persistent luminescence.

Boron has been extensively used as a sintering flux during solid state synthesis of SAED phosphors, and it has been observed to extend the afterglow duration from minutes to several hours and enhanced afterglow intensity.[10, 11] Although the mechanism behind the extended persistence behavior has not been fully explained, several groups have studied the effect of boron incorporation on the phase formation kinetics during the synthesis of strontium aluminate phosphors[5, 12-16]. As previously reported, the incorporation of boron is lowering the processing temperature of SA phases[15, 16] and facilitates the formation of the most efficiently luminescing $Sr_4Al_{14}O_{25}$[17] phosphors compound in the SA family.

In this work, we used both global and local characterization techniques in order to evaluate the effect of boron on the microstructural evolution and optical properties of $Sr_4Al_{14}O_{25}$ compounds. The techniques used for globally averaged properties included: i) thermal analysis, ii) x-ray diffraction, iii) inductively coupled plasma optical emission spectroscopy, iii) photoluminescence spectroscopy, and iv) afterglow decay measurements. For localized analysis, which is the main contribution of this dissertation to the state-of-the-art, we used advanced TEM techniques in order to evaluate the microstructural evolution of $Sr_4Al_{14}O_{25}$ phosphors by boron incorporation.

Previous studies showed that boron facilitates phase formation of the sub-stoichiometric S_4A_7 phase by lowering the energy barrier for the orthorhombic S_4A_7 phase to form, which enables one to obtain this phase at lower temperatures.[18,19] However, a detailed examination is necessary to determine the thermodynamics and kinetics of the SA phase formation; therefore, we performed thermal studies accompanied by structural investigations. To identify the processing conditions of and microstructural evolution in the Eu^{2+} and Dy^{3+} co-activated $Sr_4Al_{14}O_{25}$ phosphor compound, we performed

thermogravimetric and differential thermal analysis (TG-DTA) investigations, which is also called as simultaneous thermal analysis (STA), and for determining the crystal structure of the bulk powder we carried out powder x-ray diffraction (XRD) investigations. Ceramic phosphor compounds that have undergone thermal treatment were then analyzed by XRD in order to analyze the phase composition in the final product. Determination of the final phase composition of the compounds, we performed Rietveld phase quantification method.

Although Eu^{2+} and Dy^{3+} co-activated $Sr_4Al_{14}O_{25}$ phosphors exhibit phosphorescence behavior, it only lasts in the order of minutes, however, incorporation of boron extends the duration of phosphorescence duration up to several hours, which is also referred as persistent luminescence. In order to identify the optical characteristics of the obtained phosphors, we performed two type investigations at the bulk level: persistent luminescence characterization by afterglow decay measurements and spectral characterization of luminescence by photoluminescence (PL) spectroscopy.

As we hypothesized, when boron enters SA structure afterglow persistence behavior is enhanced due to point defect clustering at the nano and sub-angstrom scale. To investigate the effect of boron into local ionic defect distribution, we used advanced microscopy techniques: z-contrast imaging, high resolution microscopy, HRTEM, collecting selected area electron diffraction pattern (SADP), electron energy-loss spectroscopy (EELS), energy dispersive x-ray analysis (EDS) and cathodoluminescence (CL) spectroscopy. Selected area diffraction patterns were indexed by scanning/transmission electron microscopy (S/TEM) imaging and simulation software called JEMS[20] (The Java Electron Microscopy Software), and we performed quantitative STEM image simulations by QSTEM (Quantitative TEM/STEM image simulations).[21]

CHAPTER 2:

STRONTIUM ALUMINATE PHOSPHOR SYNTHESIS AND THERMAL ANALYSIS

2.1. Introduction

After synthesizing the S_4A_7 ceramic phosphor powders by a modified Pechini process, we investigated the effect of boron on the formation of the equilibrium strontium aluminate phase by differential thermal analysis to determine the thermal processing conditions, and used powder x-ray diffraction techniques to characterize its crystal structure. In order to quantify the phases formed, we applied the Rietveld phase quantification method to the x-ray diffractograms[22]. To verify the stoichiometry of the SA compounds, we analyzed the amounts of Eu, Dy, Al, Sr and B inside the overall compound, by using inductively coupled plasma optical emission spectroscopy (ICP-OES). The radiative transition between the $4f^6 5d^1 \rightarrow 4f^7$ levels of Eu^{2+} is inherently dependent on its environment in the host matrix, and contains structural information. Therefore we also characterized the luminescence behavior of SAEDB compounds by photoluminescence spectroscopy. Finally, we evaluated

the afterglow persistence duration and the decay lifetime of luminescence as a function of boron content.

2.2. Experimental

2.2.1. Chemical Processing of Strontium Aluminate Phosphors

The strontium aluminate compounds were synthesized by a modified sol-gel Pechini synthesis method[18], which is a solution polymerization technique. This approach involves the addition of precursors to boiling deionized water, enabling all the chemical constituents to be dissolved and mixed homogenously at the molecular level. All of the chemicals that have been used for synthesizing the SA phosphors are tabulated in Table 1.

Table 1 Precursors that have been used during modified Pechini sol-gel synthesis of strontium aluminate phosphors.

Precursor name	**Chemical Formula**	**Provider /Purity**
Aluminium nitrate nonahydrate	$Al(NO_3)_3 \cdot 9H_2O$	Merck / 99.9%
Strontium nitrate anhydrous	$Sr(NO_3)_2$	Merck / Extra pure
Europium (III) nitrate hexahydrate	$Eu(NO_3)_3 \cdot 6H_2O$	Alfa Aesar / 99.99%
Dysprosium (III) nitrate pentahydrate	$Dy(NO_3)_3 \cdot 5H_2O$	Alfa Aesar / 99.99%
Boron trioxide	B_2O_3	Alfa Aesar / 99.98%
Citric acid monohydrate	$C_6H_8O_7$	Merck / 99.5%
Ethylene glycol	$C_2H_6O_2$	Carlo Erba/ 99.5%

The solution was stirred for 15 minutes until the precursors became fully dissolved and properly mixed. Then the mixture solution was placed into a box furnace maintained at

110°C for 24 hours, *i.e.*, until the water content was completely vaporized. At the end of the process, a foam-like amorphous substance was produced, consisting of a low density porous structure. We then ground it into a powder prior to thermal treatment, which was performed in order for the grains of SA phase to crystallize.

As the TG-DTA investigations revealed, a three-step thermal treatment procedure was necessary, in order to obtain a fully crystalline SA compounds. The procedure that has been followed is listed below.

I. Dried and ground amorphous mixture was placed in a box furnace in air, heated up to to 600°C from room temperature with a heating rate of 10°C min^{-1}, and held at 600°C for 6 hours to burn off the organic moieties (*e.g.*, ethylene glycol).

II. Then, the temperature was then raised to the target calcination temperature, T_{cal}, with a heating rate of 10°C/min. To allow the equilibrium structure to form, the powders were kept at T_{cal} (*e.g.* at 1150°C to have S_4A_7 phase) for 10 hours and immediately quenched to room temperature.

III. To maximize the compositional homogeneity of the powders, intermediate grinding was performed before second heat treatment cycle. The final processing step was reduction of Eu^{3+} to Eu^{2+} for enabling the energy transfer between $4f^6 5d^1 \rightarrow 4f^7$ levels of Eu ions. The reduction process was applied at the target T_{cal} in a reducing atmosphere, which consists of 96 wt% Ar and 4 wt% H_2. The flow rate was set to 120 mL/min through the reduction process.

At the end of the heat treatment cycle, a yellowish-white powder was obtained. The boron-free powders could be reduced at much shorter times, approximately in 1 hour, although they only exhibited short afterglow. By contrast, powders containing boron could be reduced in 3 hours independent of the boron content, and they exhibited much longer persistence. If the reduction duration was exaggerated and applied for longer than 3 hours (*e.g.*, 4 or 5 hours), the density of oxygen vacancies could be increased too much, such that the powders turn into black instead of a yellowish white color.

2.2.2. Thermal Processing

Investigations on the phase stability of two strontium aluminate compounds having very close stoichiometry,[12-14] $SrAl_4O_7$ (SA_2) and $Sr_4Al_{14}O_{25}$ (S_4A_7), revealed that SA_2 has the lower Gibbs free energy of formation at 900°C, when it starts to form as a pure phase, until 1000°C. Because it is the most stable phase in this temperature range and has slow kinetics of formation, it can be obtained in pure form under extremely slow heating rates (*e.g.* 0.5-1°C min^{-1}). However, the S_4A_7 phase is thermodynamically metastable in this range, although it has the lowest Gibbs free energy at temperatures above 1100°C, where it can form at faster heating rates, and where SA_2 is no longer stable[13]. Therefore, applying a fast heating rate and calcining at 1100°C allows the $Sr_4Al_{14}O_{25}$ (S_4A_7) phase to dominate[14], although $SrAl_2O_4$ (SA) and $SrAl_{12}O_{19}$ (SA_6) phases can still form, along with S_4A_7.

As it has been previously reported by various studies, boron reduces the processing temperature that stabilizes the formation of S_4A_7 phase in solid-state reactions.[11, 17] Thus we investigated the effect of boron into crystallization and to formation of the S_4A_7 phase.

Moreover, because one of the goals of this study is to investigate boron-induce modification in the electronic structure of S_4A_7EDB, we aimed to obtain single-phase compounds of the long-persistence S_4A_7 phase, thus we have investigated the optimal thermal processing conditions by using thermogravimetric and differential thermal analysis (TG-DTA). 1 mol% Eu and Dy co-doped, $(SrO)_4(Al_2O_3)_7$ stoichiometric amorphous precursors with nominal, 10, 20, and 30 mol% B_2O_3 content were prepared by a sol-gel synthesis method to be used at TG-DTA measurements, where different heating rates were applied to observe the kinetics of the phase formation of different SA phases.

2.2.3. X-ray Diffraction Characterization

The effect of boron on phase formation was investigated by x-ray diffraction (XRD) method by using a Bruker D8 Advanced diffractometer. Primary analysis of XRD patterns were carried out by comparing the experimental diffraction patterns powder diffraction files with those from the ICDD database—, Diffrac plus the *Eva* program (AXS Bruker, Germany). Patterns from the Inorganic Crystal Structure Database (ICSD)[23], which is available in the Find IT software database, have also been used for further analysis of the structure for confirmation of the existing phases in the compounds. The phase information obtained through XRD measurements were then evaluated by Rietveld[22] phase quantification method.

To evaluate the effect of boron on formation of SA phases, we used modified Pechini sol-gel synthesized[18, 24] SA phosphor powders with S_4A_7 and SA_2 stoichiometry having different amounts of boron (0, 10, 20, 30 mol% B_2O_3). XRD patterns of powders were collected between 2θ = 10-70° with a Cu-K_α source (λ = 1.54056 Å), having a step size of 0.01°, and 1 second per step.

In this part of the work, we investigated *i)* the effect of starting stoichiometry and calcination temperature on the final stoichiometry of the compound, ii) the effect of boron on crystallization of S_4A_7 phase.

2.2.4. Elemental Analysis

To assess the elemental stoichiometry of synthesized SA phosphors with varying amounts of boron content, we used inductively coupled optical emission spectroscopy ICP-OES (Varian Vista-Pro) technique. The analyzed phosphor compounds were prepared with $(SrO)\bullet(Al_2O_3)_2$ and $SrO\bullet(Al_2O_3)_6$ $(SrO)_4\bullet(Al_2O_3)_7$ stoichiometry with 1 mol% Eu, 1 mol% Dy, and having different amounts of boron. The samples to be analyzed by this technique required dissolving the analytes in a solvent. The analyte preparation followed these steps:

1. 0.1 g of powder sample was weighed and poured into 2 mL of nitric acid and 6 mL of HCl (1:3 ratio should be maintained) acid solution to be dissolved.
2. The dissolved solution was placed into a microwave oven that is maintained at 200°C and kept there for one hour to let them fully dissolved.
3. Then, dissolved sample solution was diluted by adding 50 mL extra pure deionized water.
4. The solution obtained was diluted once more, by taking 1 mL from diluted solution and pouring it into 10 mL of pure water to be mixed.
5. At the final step, a reference standard solution was prepared, which contains the elements to be analyzed (*e.g.* Al, Sr, Eu, Dy, B,...) The purpose for preparing the standards was to create a calibration curve to determine concentration of the measured samples.

Before starting the measurements, an estimation of the expected concentration of each element should be selected from the ICP software, *i.e.*, the experimental conditions were defined. The spectral range of the optical emissions should be estimated for each element. This must be calculated by estimating the expected amount of the element to be analyzed. Because the intensity of the emission is proportional to the concentration of the element of interest, if the estimation this emission range would be too far off; the device will not yield any result, and thus an error message of "uncalculated" will be displayed. After we entered the appropriate ranges to the device software, we may proceed with the measurements.

The solution was injected into inductively coupled (argon) plasma by a nebulizer. The temperature of the initial radiation zone is ~ 6800K, enabling (i) dissolution of precursor, (ii) vaporization of the residual salt, (iii) dissociation of the gas atoms, (iv) ionization of the atoms, and (v) excitation of the ions.

Measurements began with the reference standards for determining a calibration curve for each element of interest, using difference concentrations and recording their emission intensity. Then we began to analyze the unknown samples (*i.e.*, analytes). Analytes were excited to different atomic and/or ionic states, and the emission spectra are collected. For quantitative analysis of the amounts of each element present, the emission intensity of each peak detected from the analyte is compared to the calibration curve for the element of

interest. The calibration curve will indicate the concentration of element in units of g/mL. The results are converted into wt% and then to at% for data analysis.

ICP analyses have been performed on two different set of samples, which both have been synthesized by a modified Pechini sol-gel process. However one set of specimen were thermal treated in a box furnace at air first then reduced in a tube furnace under a varigon (96% Ar, 4% H_2) atmosphere. The second set of specimen were heat treated by TG-DTA in both air and N_2, using the same thermal treatment steps as other set, after which the final products were collected for analysis by ICP-OES .

Samples were prepared with $(Sr_4Al_{14}O_{25})_{0.98-x}:(B)_x,Eu_{0.01},Dy_{0.01})$ stoichiometry and subjected to TG-DTA analysis. Preparations made for the samples to be analyzed and thermal cycle that was used during TG-DTA measurements can be listed as followed:

a. Before starting the TG-DTA analysis, amorphous precursors with different amounts of B content were synthesized using a sol-gel technique (a modified Pechini process) having the S_4A_7 stoichiometry. These samples were heated up to 600°C in a furnace for 6 hours, until the organic moieties were burnt off. The specimen were thus ready for TG-DTA analysis.
b. In order to investigate the structural and chemical evolution during ceramic powder processing, we evaluated the effect of heating rate and calcination ambient on yielding a fully crystallized S_4A_7 phosphor compound:
    i. Heating up from room temperature up to 600°C with 1°C/min, 5°C/min, and 10°C/min heating rates and under both air and N_2 ambient until all remaining organics have been removed from the specimen.
    ii. Heating up to 1150°C with the same set of heating rates as in part *i*, but maintaining the product at this temperature for 10 hours to allow complete crystallization.

To determine the stoichiometric amounts of Al, Sr, Eu, Dy and B, we collected two sets of samples; the first set was prepared with SA_2 and S_4A_7 stoichiometry, and thermal treatment was applied. Specimens that were collected after TG-DTA measurements were subjected to ICP-OES elemental analysis, and the results are given.

2.2.5. Photoluminescence Spectroscopy

Another optical characterization method, photoluminescence spectroscopy, was used to identify the luminescence behavior of S_4A_7 phosphors. Emission spectra of the samples with S_4A_7 and SA_2 stoichiometry were measured using a custom-built, bench-top photoluminescence set-up consisting of an Ocean Optics USB 4000 miniature fiber optic spectrometer coupled with an integrating sphere and Kimmon He-Cd type UV laser as an illumination source. Luminescence emission spectra were recorded with the following procedure:

i. The UV laser excited phosphor powders for 30 minutes, and emission spectra were recorded while the excitation source is still on.
ii. Illumination source was turned off after 30 minutes and emission spectra were recorded.

However, this system contained only one type of illumination source, thus we also carried out measurements by a Cary Eclipse Fluorescence Spectrophotometer with a mercury lamp source, which had a very wide range of excitation and emission wavelength capacity (200-1100 nm). However, there was not a solid sample holder thus samples were prepared as a suspension with fixed concentration. Prior to mixing, powders were ground for 30 minutes to prevent the sedimentation of the powders. From each sample, we weighed 0.05 g of powder and dispersed it in 2.5 mL of pure ethanol to be mixed and photoluminescence emission spectra were recorded for Eu^{2+}, Dy^{3+} co-doped S_4A_7 compounds with varying amounts of boron, under 270 and 300 nm excitation wavelengths.

2.2.6. Afterglow Persistence

Boron incorporation during the synthesis of SA compounds has been shown to facilitate the long-persistent $Sr_4Al_{14}O_{25}:Eu^{2+},Dy^{3+}$. In order to characterize the effect of boron in S_4A_7 compounds, the afterglow persistence of the powder S_4A_7 compounds with varying amounts of boron was measured by a home-made optical set up consist of a 325 nm UV

light source as illumination and photomultiplier tube head (Hamamatsu, H7421) coupled with a photon counting unit (Hamamatsu, C 8855). The photoluminescence set up is consisted of an Ocean Optics USB 4000 miniature fiber optic spectrometer coupled with a fiber optic cable. The measurement procedure was the following: each SAED compound with varying amounts of boron content (boron-free, 10, 20, and 30 mol% B_2O_3) were illuminated with the UV light (325 nm, 6 kW lamp energy) for 10 minutes. Immediately after the illumination source was extinguished, samples were placed to a holder, which was positioned 0.5 cm away from the photomultiplier head entrance, and the afterglow intensity decay was recorded for 14 hours.

2.3. Results

2.3.1. Thermal Analysis of SA Phosphors

We started to investigate the crystallization onset temperatures with a boron-free S_4A_7 compound heated with 10°C/min heating rate up to 1400°C (Figure 1), to determine the regions where phase change reactions take place

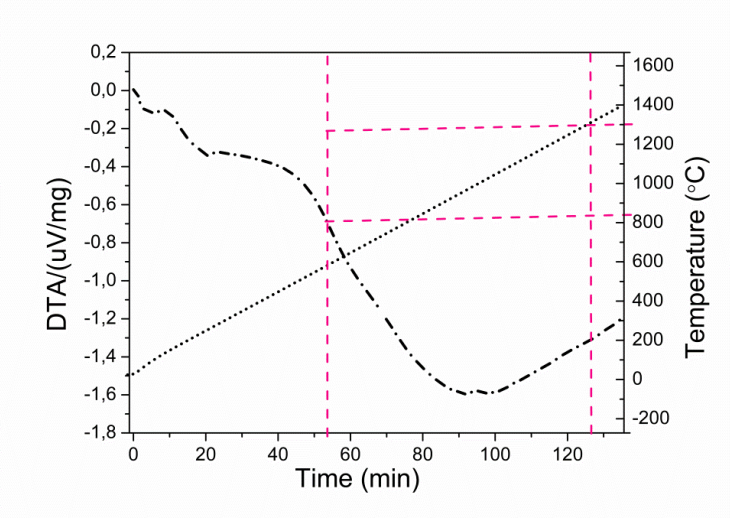

Figure 1 DTA curve of boron-free S_4A_7 compound obtained with 10°C/min heating rate from room temperature up to 1400°C, at air.

A broad exothermic region was observed, starting at *ca.* 800°C and continuing up to *ca.* 1200°C. The S_4A_7 phase was expected to form above 1100°C and was known to be stable up to 1500°C.[13] Therefore, we wanted to analyze that region in more detail, so we performed TG-DTA (Netzsch Jupiter 449, simultaneous thermal analyzer) measurements both in air and pure N_2 atmosphere with 1°C min^{-1}, 5°C min^{-1}, 10°C min^{-1} heating rates. After analyzing the TG-DTA curves we came up with the following heat treatment procedure:

i. Samples for TG-DTA analysis were prepared by sol-gel synthesis, which has been explained in detail in section 2.2.1. Samples were calcined at 600°C for 6 hours to burn off the organic content and left as amorphous precursor for analysis. However, there was still a dramatic decrease in mass loss around 600°C; thus samples were kept at this temperature an additional 2 hours.
ii. Then, the samples were heated up to 1150°C with the same heating rate applied in previous step.
iii. After reaching 1150°C, the samples were kept at this temperature to allow complete crystallization.

We have conducted thermal analysis with different heating rates having isothermal step and with different amounts of B content to analyze the effect of boron on crystallization of the equilibrium phase. TG-DTA curves of S_4A_7 compounds obtained at air and N_2 are given in Figure 2, Figure 3, and Figure 4 with 1°C/min, 5°C/min, and 10°C/min heating rates, respectively. The shift in exothermic onset with B content was summarized in Figures 2-5 and, including the impact of heating rate and processing ambient in Table 2 and Table 3. The dotted line represents the temperature variation over time, where it is plotted to the secondary (right) y-axis.

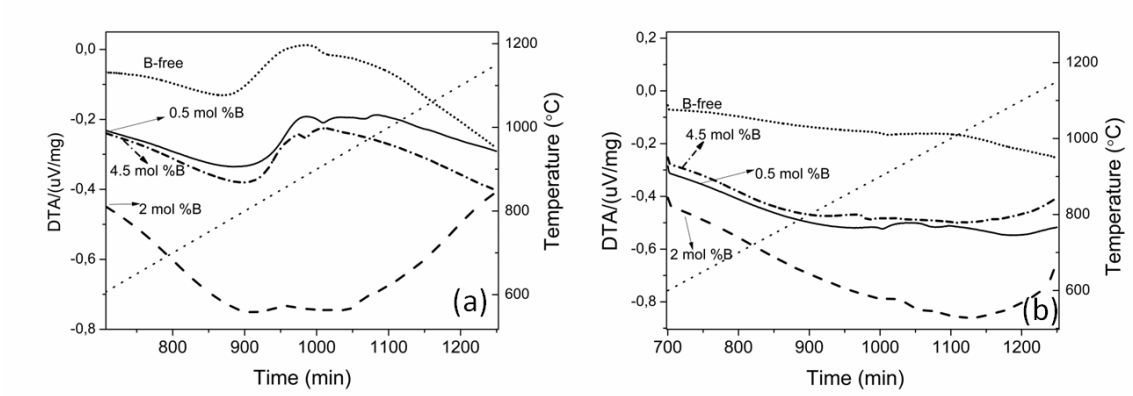

Figure 2 DTA curves of S_4A_7 stoichiometric phosphor compounds at 1°C/min heating rate under (a) air and (b) pure N_2.

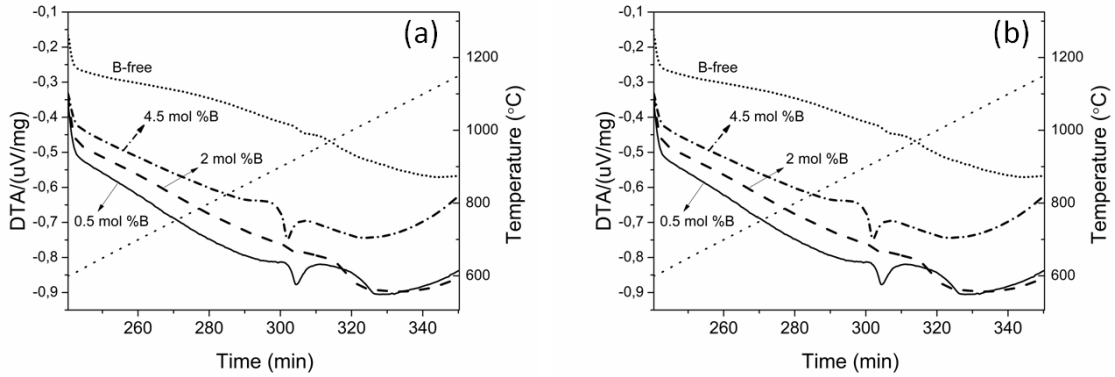

Figure 3 DTA curves of S_4A_7 stoichiometric phosphor compounds at 5°C/min heating rate under (a) air and (b) pure N_2.

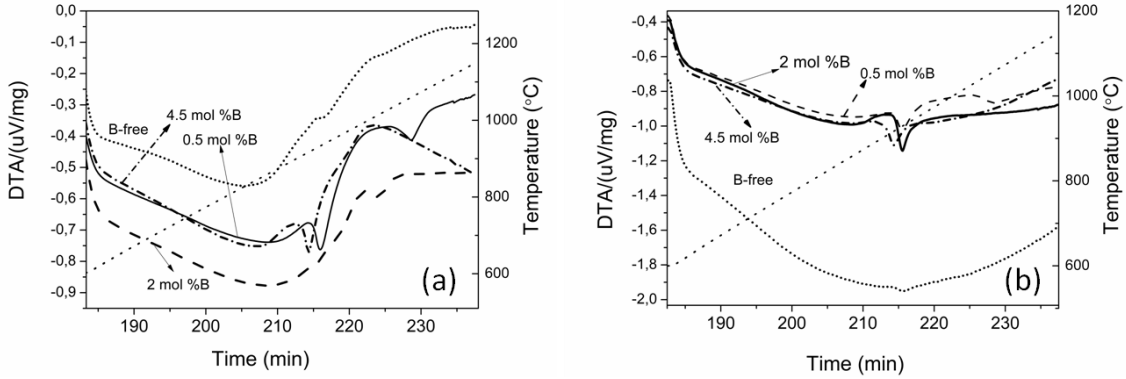

Figure 4 DTA curves of S_4A_7 stoichiometric phosphor compounds at 10°C/min heating rate under (a) air and (b) pure N_2.

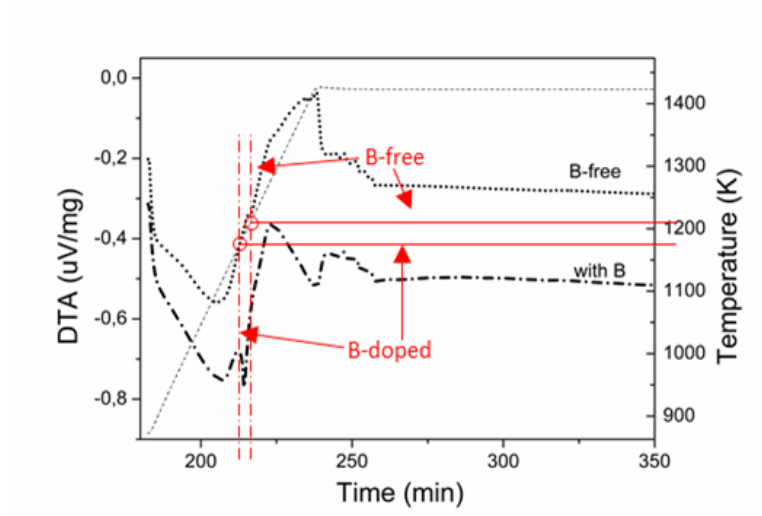

Figure 5 TG-DTA of boron-doped (black dot-dash line) and boron-free (black dotted line) S_4A_7ED compounds, obtained using a 10°C/min heating rate in air environment; corresponding time-temperature plot (gray dotted line). Onset of crystallization estimated from the time of the inflection in the first derivative, indicated by the dot-dash red line, and the corresponding temperature, indicated by the solid red line.

Table 2 Change in crystallization exotherms of S_4A_7 phosphors with different boron content, obtained with different heating rates in air and N_2 atmospheres.

Boron Content	**Exotherm (ºC) (crystallization)**					
(mol% B_2O_3 addition)	1°/min		5°/min		10°/min	
	Air	N_2	Air	N_2	Air	N_2
0	899	901	920	914	923	932
10	897	898	917	912	922	914
20	869	927	984	976	919	917
30	880	874	899	904	910	905

* Starting material mass has an error 81±1 mg.

Table 3 Duration required for complete crystallization investigated for different boron composition, by TG-DTA analysis with different heating rates in air and N_2 atmospheres.

Boron Content	**Isotherm (min)**					
(mol% B_2O_3 addition)	1°C/min		5°C/min		10°C/min	
	Air	N_2	Air	N_2	Air	N_2
0	--	1810	--	788	--	443
10	--	--	--	584	--	459
20	--	--	--	472	--	403
30	--	--	-	474	--	356

We observed that exotherm onset temperatures change with boron composition in all three different heating rates. An isothermal onset, which implies the duration of crystallization, also decreases with increasing boron amount. The isothermal onset could not be observed for the 1°C/min heating rates and in the air environment.

In order to correlate the effect of B with the phase formation temperature, we have conducted XRD measurements on the DTA products.

2.3.2. Structural Analysis by X-ray Diffraction

To determine the effect of starting stoichiometry on phase purity of S_4A_7 compound, we synthesized $(SrAl_4O_7)_{0.98-x}:(Eu)_{0.01}:(Dy)_{0.01}:B_x$ (SA_2ED) and $(Sr_4Al_{14}O_{25})_{0.98-x}:(Eu)_{0.01}$, $(Dy)_{0.01}:B_x$ stoichiometric compounds and observed the formation of SA phases with different amounts of boron content that were calcined at air and reduced varigon (96% Ar, 4% H_2 mixture) at 1150°C and XRD patterns were collected. Following powder diffraction files (PDF) were used during preliminary phase determination: 01-074-1810 (S_4A_7), 00-034-0379 (SA), 00-025-1289 (SA2), and 01-070-0947 (SA6). We have quantified the amounts of each phase present in the final product by Rietveld phase quantification method by using these files obtained from database. Compounds with SA_2 and S_4A_7 as the nominal starting stoichiometry were analyzed, in order to investigate the impact of the starting stoichiometry on the final equilibrium phase (see Figure 6). The main objective was to obtain a phase pure S_4A_7 compound, which is expected to form above 1100°C (*e.g.* 1150°C). Therefore, both compounds, containing 4.5 mol%B, were calcined at 1150°C for 10 hours and quenched to room temperature to maintain the metastable S_4A_7 phase. According to preliminary observed XRD patterns (see Figure 6), both methods yielded the S_4A_7 phase.. The quenched phosphor samples were then sintered under reducing atmosphere (96% Ar+4% H_2) for 5 hours, and Rietveld refinement was applied to identify the phases and quantify their amounts. Rietveld analysis results for the sample with SA_2 starting stoichiometry gave 96.34 wt% S_4A_7 and 3.66 wt% of SA_6. Calculated errors of the fitting operation were R_p=21.36, R_{wp}=28.94, R_{exp}=28.94 with 1.18 *goodness of fit* value. Quantification results of the sample with S_4A_7 stoichiometry gave 87.6 wt% S_4A_7, 12.4 wt% of SA_2. Calculated errors of the fitting operation were, *Rp*=21.34, *Rwp*=30.04, *Rexp*=24.35 with 1.23 *goodness of fit (GOF)* value. GOF value is considered to be good as it reaches to 1.00.[25] Figure 7 shows an example of the results of Rietveld analysis of the S_4A_7 phase, forming from a starting stoichiometry SA_2, including original XRD pattern, calculated pattern and error.

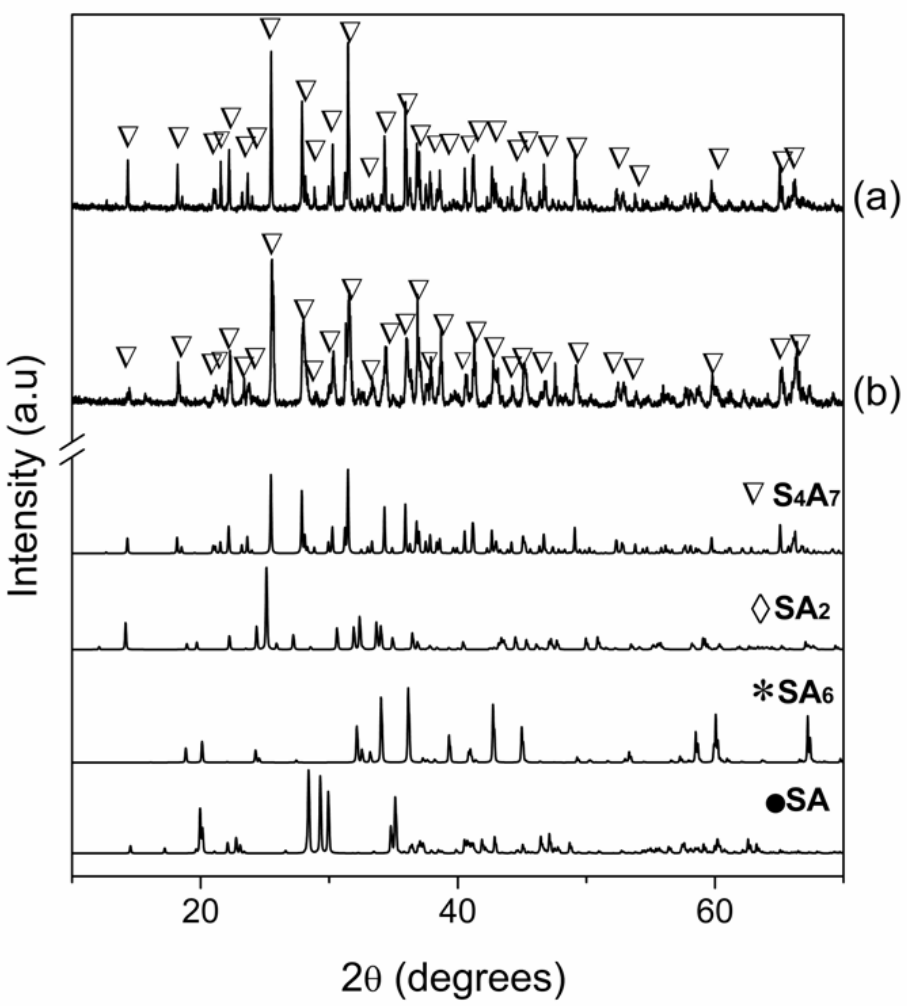

Figure 6 XRD pattern of S_4A_7 phase yielded compound with **(a)** SA_2 and (b) S_4A_7 starting stoichiometry.

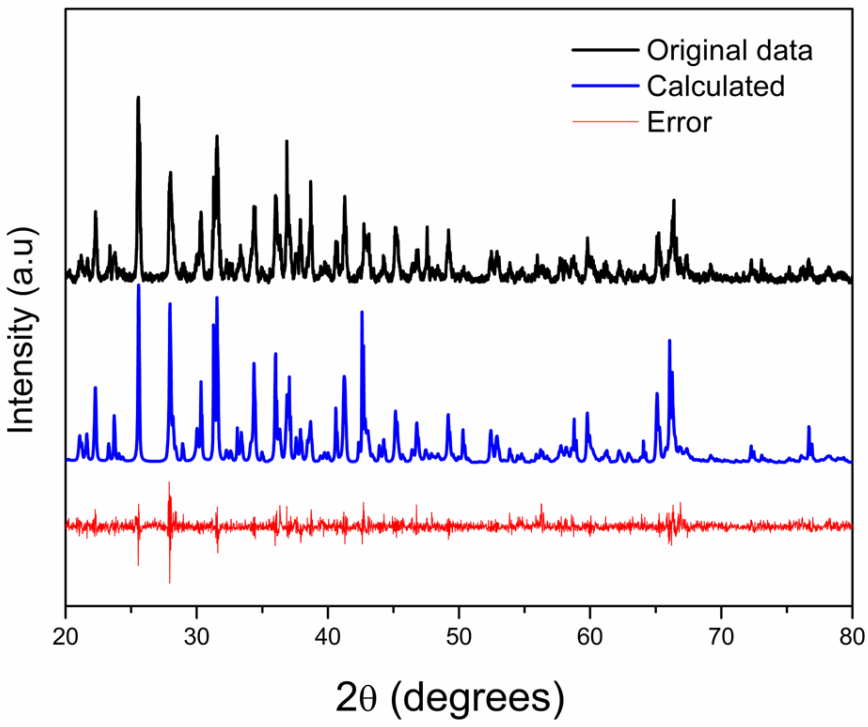

Figure 7 Rietveld analysis result of S_4A_7 phase compound having a SA_2 starting stoichiometry.

To obtain high purity S_4A_7 phase compounds, we conducted a thermal analysis experiment at critical points during the powder synthesis process and collected the samples for XRD analysis. DTA investigations showed that crystallization began ca. 910-930°C (see Figure 4) and shifted to lower temperatures with boron content. Therefore, to observe the overall crystallization of strontium aluminate compounds, we interrupted heat treatment before and after crystallization, and analyzed their XRD patterns. The stop points were designated to be at 900°C, at 960°C, at 1150°C for 2 hours, and at 1150°C for 5 hours. XRD results of the collected samples are shown in Figure 8. Rietveld phase quantification showed that the sample calcined at 1150°C for 2 hours contained of 79.63% S_4A_7, 12.39% SA_2, and 7.97% SA_6 phases, whereas the sample calcined for 5 hours 1150°C contained of 88.55% S_4A_7, 0.71% SA_2, and 10.74% SA_6.

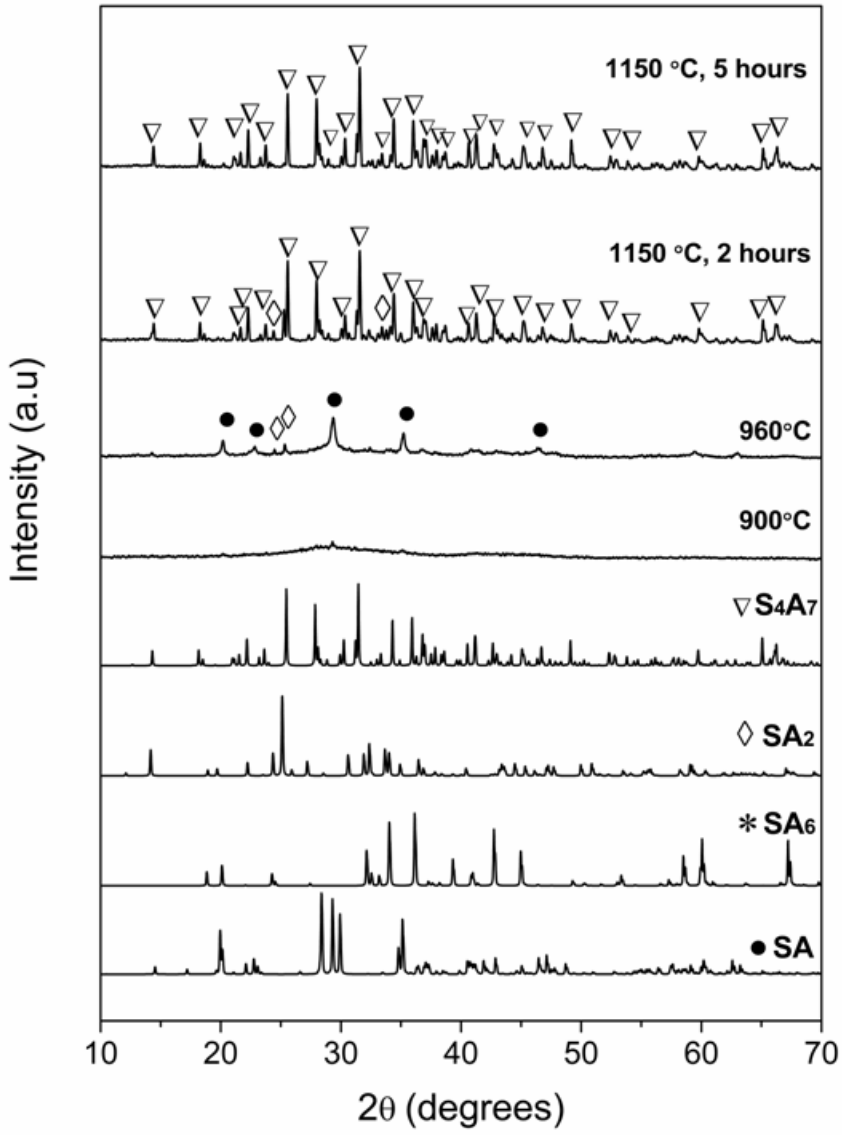

Figure 8 Powder x-ray diffraction pattern of an amorphous precursor, calcined at 900°C, 960°C, 1150°C for 2 hours, and 1150°C for 5 hours. The amorphous precursor was pre-calcined at 600°C for 8 hours to first burn off the organic moieties.

Further TG-DTA analysis was performed with boron-free, 0.5, 2, and 4.5 mol% B containing S_4A_7ED compounds, comparing the influence of an air and a N_2 atmosphere. The results of XRD analysis of the powders are shown in Figure 9.

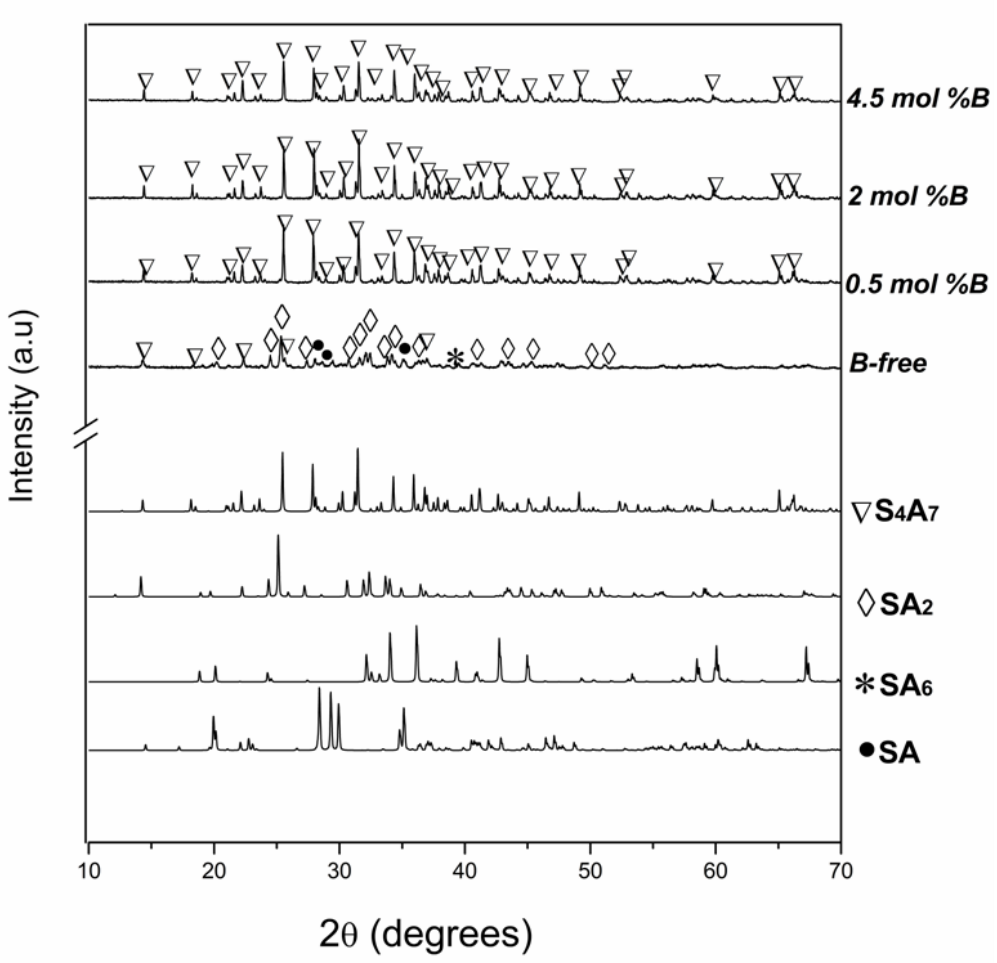

Figure 9 XRD patterns obtained after TG-DTA analysis with 10°C/min heating rate at N_2 atmosphere with changing boron content as determined by ICP-OES.

To quantify the amounts of phases in the final product, we performed Rietveld analysis, and the results were listed on Table 4.

Table 4 Phase composition revealed by Rietveld analysis of the XRD data from the S_4A_7ED compounds with boron content as determined by ICP-OES.

Boron content (mol%)	S_4A_7 (wt%)	SA_6 (wt%)	SA_2 (wt%)	SA (wt%)
0	53.95	2.89	11.32	31.75
0.5	98.41	0.66	0.94	0
2	98.26	1.16	0.61	0
4.5	99.46	0	0.54	0

Compounds with non-zero boron content were dominated by the S_4A_7 phase, whereas the boron-free compound consisted of four different phases, S_4A_7, SA_2, SA, and SA_6, with the S_4A_7 phase still dominant, albeit to a lesser extent. Finally, in order to determine if boron merely lowers the energy barrier for the formation of S_4A_7, we calcined a boron-free powder at a much higher temperature, 1300°C. The XRD spectra (Figure 10) showed an increase in the phase percentage of S_4A_7. Thus we conclude that B is not necessary for the formation of the high temperature equilibrium phase S_4A_7 and only lowers the energy barrier for phase formation.

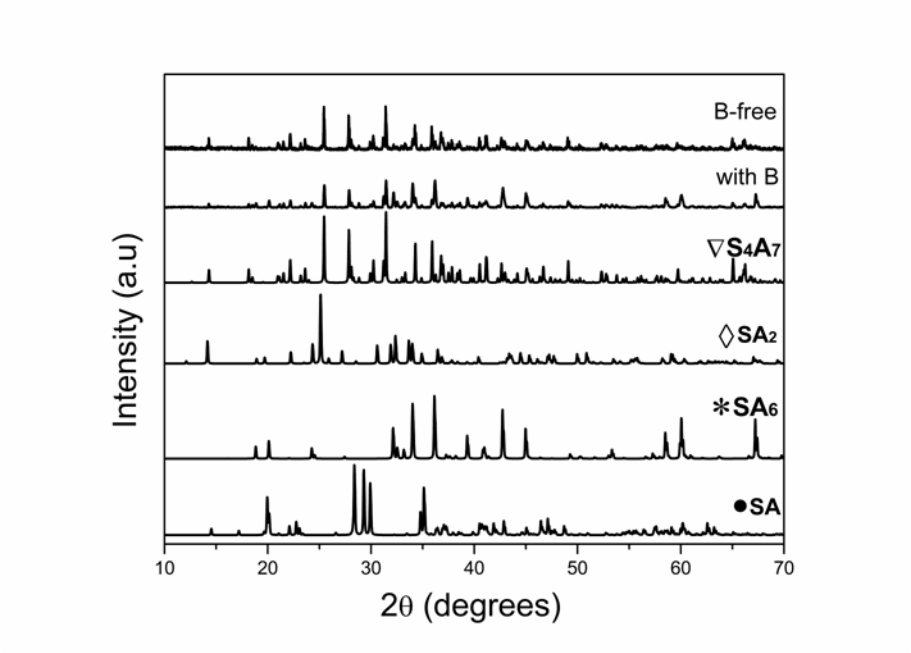

Figure 10 XRD pattern of boron-free and 4.5 mol%B containing S_4A_7:Eu^{2+}, Dy^{3+} compound calcined at 1300°C.

2.3.3. ICP-OES Elemental Analysis

In order to determine the content of Sr, Al, Eu, Dy, and B in $(SrO)_4•(Al_2O_3)_7$:Eu^{2+},Dy^{3+} phosphors compounds with no boron, 10, 20, 30 mol% B, we collected samples after TG-DTA measurements carried out by 1, 5, and 10°C/min heating rate in air and N_2 , and performed elemental analysis by ICP-OES. Three measurements were collected for each data point, and their average values and standard deviations are shown in Figure 11 below and Table A1-A3 in the appendix.

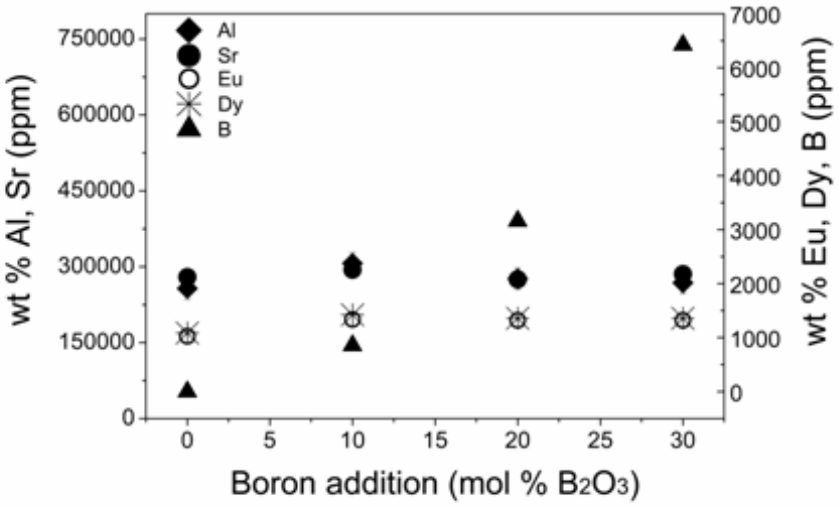

Figure 11 Concentration (mg/kg) of Eu, Dy, B, Al, and Sr elements in S_4A_7EDB compounds collected after DTA analysis with 10°C min^{-1} heating rates, obtained by ICP-OES measurement.

According to Figure 11, an increase in boron content was observed. This implies that boron was incorporated into the compound. The concentrations reported are bulk concentration, as boron could be present either inside or on the surface of the bulk particle. In order to estimate approximate values of boron content in at%, or mol%, we performed conversion calculations according to Equation 1:

$$at\%A = \frac{\frac{wt\%A}{at.wt.A}}{\frac{wt\%A}{at.wt.A} + \frac{wt\%B}{at.wt.B} + \frac{wt\%C}{at.wt.C}\frac{wt\%D}{at.wt.D} + \frac{wt\%E}{at.wt.E}} \qquad \text{Equation 1}$$

,where *at. wt.* (*e.g. at.wt.A*) corresponds to the atomic weight of the element, to be converted to atomic percent. Applying this formula for each element, estimated mol% values were calculated and given in Table 5.

Table 5 Atomic percent calculations obtained for $((SrO)_4 \bullet (Al_2O_3)_7)_{0.98-x}Eu_{0.01}Dy_{0.01}B_x$, where the incorporated B amount was varied from none, 10, 20, and 30 mol% B_2O_3.

			Atomic%				
Boron Content (mol% B_2O_3)	Heating rate/Atmosphere	Sample No	Eu	Dy	B	Al	Sr
Boron-free	10°C min^{-1}/N_2	1	0.062	0.059	0.000	74.964	24.915
Boron-free	10°C min^{-1}/air	2	0.059	0.059	0.000	74.824	25.058
Boron-free	5°C min^{-1}/N_2	3	0.062	0.059	0.000	75.259	24.621
Boron-free	5°C min^{-1}/air	4	0.060	0.059	0.000	74.832	25.049
Boron-free	1°C min^{-1}/N_2	5	0.063	0.059	0.000	75.780	24.098
Boron-free	1°C min^{-1}/air	6	0.061	0.059	0.000	75.963	23.916
10	10°C min^{-1}/N_2	7	0.066	0.065	0.501	76.610	22.758
10	10°C min^{-1}/air	8	0.065	0.066	0.534	76.681	22.653
10	5°C min^{-1}/N_2	9	0.065	0.065	0.553	76.630	22.687
10	5°C min^{-1}/air	10	0.064	0.065	0.611	76.506	22.754
10	1°C min^{-1}/N_2	11	0.065	0.065	0.517	76.815	22.537
10	1°C min^{-1}/air	12	0.064	0.065	0.639	76.659	22.572
20	10°C min^{-1}/N_2	13	0.072	0.067	2.175	74.853	22.834
20	10°C min^{-1}/air	14	0.069	0.067	2.137	74.785	22.941
20	5°C min^{-1}/N_2	15	0.073	0.068	2.002	74.375	23.483
20	5°C min^{-1}/air	16	0.071	0.068	1.918	74.628	23.315
20	1°C min^{-1}/N_2	17	0.070	0.068	2.009	74.455	23.398
20	1°C min^{-1}/air	18	0.070	0.067	2.065	74.828	22.970
30	10°C min^{-1}/N_2	19	0.092	0.087	4.234	71.324	24.263
30	10°C min^{-1}/air	20	0.079	0.083	4.299	71.959	23.580
30	5°C min^{-1}/N_2	21	0.076	0.082	4.487	71.803	23.553
30	5°C min^{-1}/air	22	0.089	0.086	4.278	71.581	23.967
30	1°C min^{-1}/N_2	23	0.081	0.086	4.370	71.831	23.632
30	1°C min^{-1}/air	24	0.083	0.088	4.501	71.449	23.879

According to the calculated values in terms of atomic percentages, the Eu and Dy amounts were observed to be close to expected amount, ranging between *ca.* 0.6-0.9%, instead of 1%. However, the measured values of B fell substantially short of the nominal B_2O_3 amount. Because the powders analyzed by ICP-OES were collected from the crucible and ground prior to specimen preparation for ICP analysis, this discrepancy may be attributed to unincorporated B having remained behind as a glassy coating in the alumina crucible, and, to a lesser extent, having volatized during heat treatment.

The theoretical Sr and Al cation ratio for the S_4A_7 stoichiometric compound is (Al/Sr) = (14/4) = 3.5. Table 6 lists the corresponding cation ratios for the ICP-OES results presented in Table 5. Cation ratio calculated for each different sample (see Table 5) ranges between 2.94-3.41.

Table 6 Al to Sr ratio of S_4A_7 stoichiometric compounds for various boron incorporation, calculated by ICP-OES values**.**

Sample No	Heating rate/Atmosphere	Boron Content (mol% B2O3)	Al (at%)	Sr (at%)	Al/Sr ratio
1	10°C $min^{-1/}N_2$	Boron-free	74.96	24.91	3.01
2	10°C min^{-1}/air	Boron-free	74.82	25.06	2.99
3	5°C min^{-1}/N_2	Boron-free	75.26	24.62	3.06
4	5°C min^{-1}/air	Boron-free	74.83	25.05	2.99
5	1°C min^{-1}/N_2	Boron-free	75.78	24.10	3.14
6	1°C min^{-1}/air	Boron-free	75.96	23.92	3.18
7	10°C min^{-1}/N_2	10	76.61	22.76	3.37
8	10°C min^{-1}/air	10	76.68	22.65	3.38
9	5°C min^{-1}/N_2	10	76.63	22.69	3.38
10	5°C min^{-1}/air	10	76.51	22.75	3.36
11	1°C min^{-1}/ N_2	10	76.82	22.54	3.41
12	1°C min^{-1}/air	10	76.66	22.57	3.40
13	10°C min^{-1}/ N_2	20	74.85	22.83	3.28
14	10°C min^{-1}/air	20	74.79	22.94	3.26
15	5°C min^{-1}/ N_2	20	74.37	23.48	3.17
16	5°C min^{-1}/air	20	74.63	23.31	3.20
17	1°C min^{-1}/ N_2	20	74.45	23.40	3.18
18	1°C min^{-1}/air	20	74.83	22.97	3.26
19	10°C min^{-1}/ N_2	30	71.32	24.26	2.94
20	10°C min^{-1}/air	30	71.96	23.58	3.05
21	5°C min^{-1}/ N_2	30	71.80	23.55	3.05
22	5°C min^{-1}/air	30	71.58	23.97	2.99
23	1°C min^{-1}/ N_2	30	71.83	23.63	3.04
24	1°C min^{-1}/air	30	71.45	23.88	2.99

2.3.4. Photoluminescence Spectroscopy Analysis

Optical characterization of the S_4A_7 phosphors with and without boron was performed by photoluminescence spectroscopy technique. Measurements were carried out 2 ways: 1) by using a Cary Eclipse fluorescence spectrophotometer with mercury lamp source, and 2) by using a custom-built, bench-top photoluminescence set-up consisting of an Ocean Optics USB 4000 miniature fiber optic spectrometer coupled with an integrating sphere and Kimmon He-Cd type UV laser (power) as the illumination source. The measurement procedure was described in Section 2.2.5

Under 325 nm wavelength excitation, the PL spectra of boron-free and 4.5 mol%B containing S_4A_7 phosphors were compared (Figure 12), and both show two broad emission peaks located at *ca.* 405 nm and at *ca.* 492 nm. These results are consistent with reports in the literature attributing these two peaks to Eu^{2+} emission in S_4A_7 host lattice.[5, 26, 27] There are two crystallographically non-equivalent Sr^{2+} sites in S_4A_7 crystal structures, where the Eu atom may replace Sr atoms. These two non-equivalent Sr^{2+}sites, which have been replaced by Eu^{2+}ions, have emission peaks that have been attributed to $4f^6 5d^1 \rightarrow 4f^7$transitions in Eu^{2+} ions located in the two crystal environments of different crystal field.

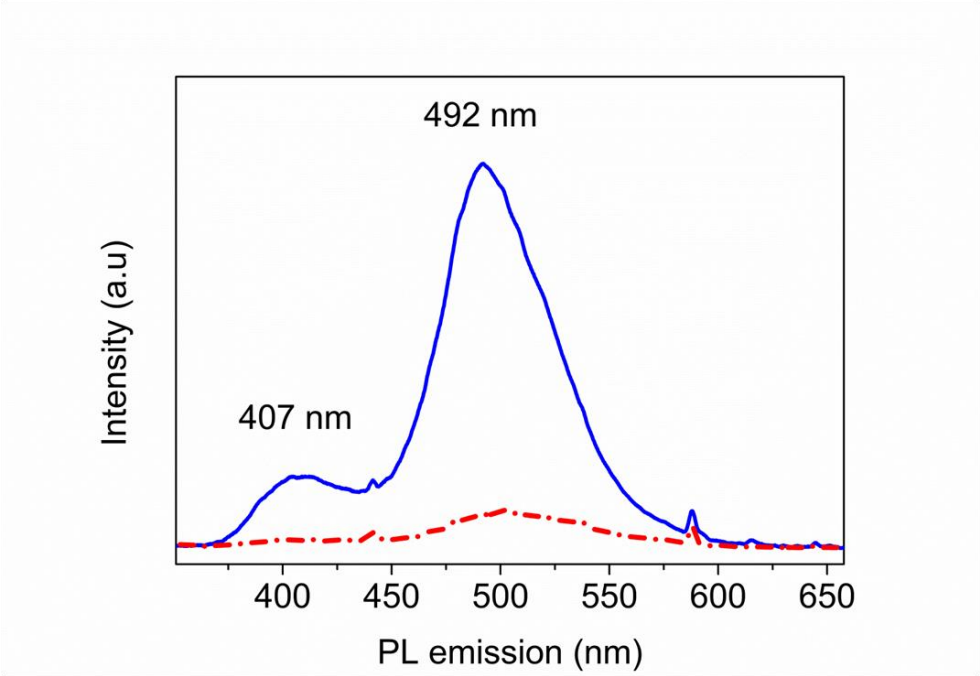

Figure 12 PL emission spectra of S_4A_7 phosphor with 4.5 mol%B presented with solid blue line, and no boron shown under 325 nm excitation wavelengths.

In order to access excitation at other wavelengths, we investigated photoluminescence behavior further with the Cary Eclipse fluorescence spectrophotometer under 270 and 300 nm excitation wavelengths and the results are shown in Figure 13. We observed that as boron amount increases, there is an increase in the 405 nm emission corresponding to a decrease in emission at 492 nm under both 270 and 300 nm excitation wavelengths.

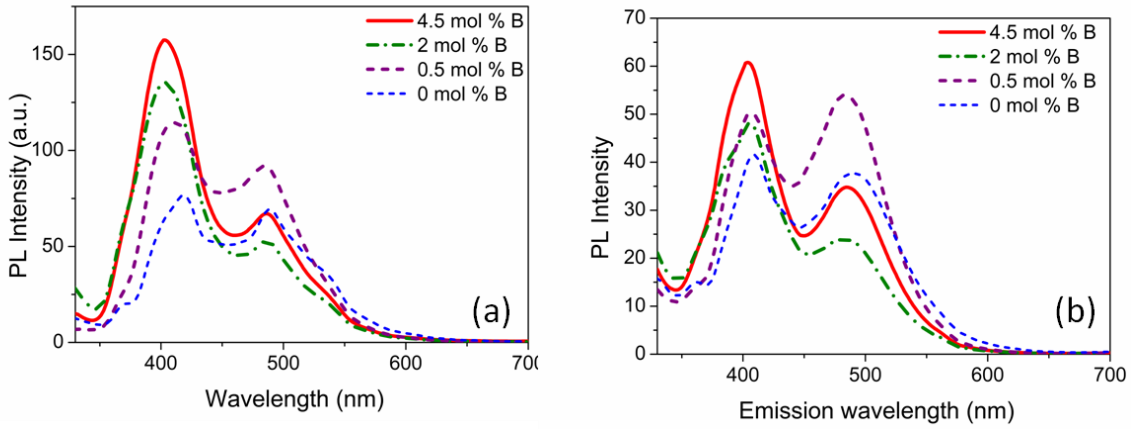

Figure 13 PL emission spectra of S_4A_7 phosphors with changing boron amounts obtained under (a) 270 nm excitation, and (b) 300 nm excitation wavelengths.

2.3.5. Afterglow Persistence Characterization

To quantify the impact of boron in extending persistence, we measured the afterglow decay of the emission at 490 nm of the S_4A_7 phosphors under ambient conditions. S_4A_7 powders both with and without boron exhibited persistent luminescence The afterglow decay characteristics of S_4A_7 phosphor compounds were measured by using a custom-built optical bench PL system as described in Section 2.2.6. The boron-containing samples luminesced for longer than 14 hours, after being illuminated with a UV light source (365 nm) for 10 minutes, whereas, the persistence duration of the boron-free compounds lasted only a few minutes (Figure 14). These decay characteristics are consistent with other work reported in the literature[11]. S_4A_7 powders both with and without boron exhibited persistent luminescence in a two-step decay mechanism: a fast decay in intensity followed by a much slower decay profile, as shown in Figure 14.

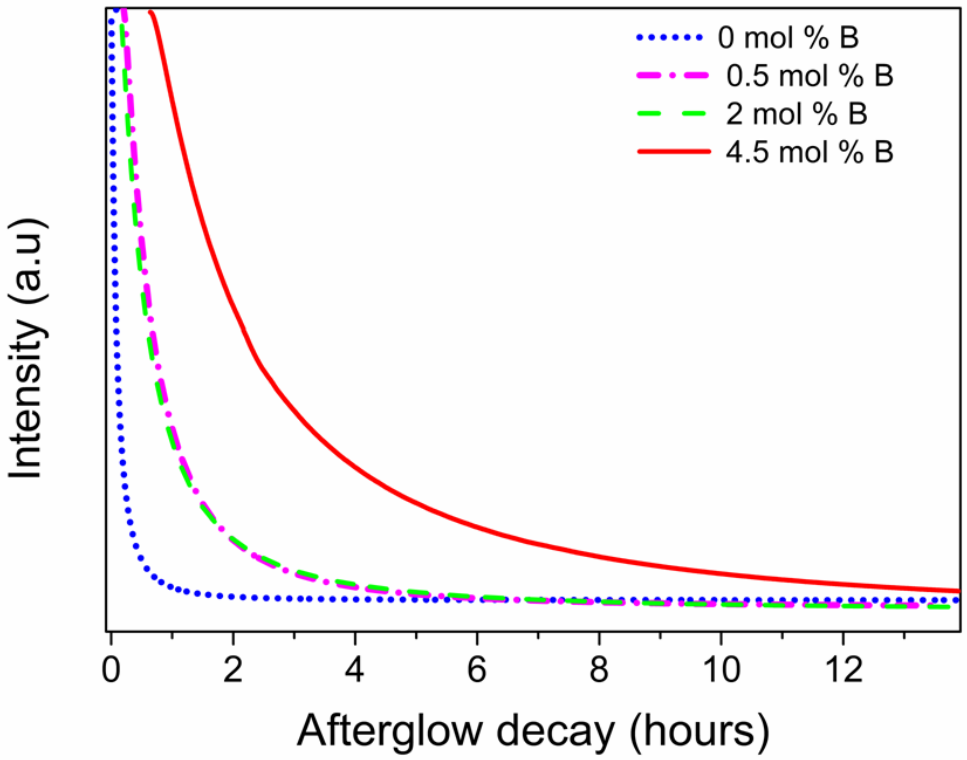

Figure 14 Afterglow intensity decay of S_4A_7 phosphors calcined at 1150°C, containing no boron, 0.5, 2, and 4.5 mol% B as determined by ICP-OES analysis

The two obvious slopes in the decay curves suggested that there must two independent de-trapping mechanisms. Curve-fitting, using Equation 2, enabled quantification of the decay parameters of the two mechanisms controlling the afterglow decay in the SAEDB compounds. The decay constant parameters that were extracted by curve-fitting are listed in Table 7.

$$I/I_0 = A_1 \exp(-t/\tau_1) + A_2 \exp(-t/\tau_2) \qquad \text{Equation 2}$$

Table 7 Decay lifetimes of Eu^{2+} and Dy^{3+} co-doped S_4A_7 compounds with varying amounts of boron incorporation.

B content (mol%)	Decay lifetime(hours)	
	τ_1	τ_2
B-free	0.39	0.08
0.5 mol% B	0.44	1.71
2.0 mol% B	1.89	0.41
4.5 mol% B	1.23	4.69

As described in the previous section 2.3.2 (see Figure 10), boron-free samples yielded S_4A_7 phase if calcination was performed at 1300°C. Therefore, we have performed afterglow decay measurements with boron-free and 4.5 mol% B containing S_4A_7 compounds that were calcined at 1300°C. Because the extended afterglow was much longer in the B-doped compound, we conclude that the dominance of the S_4A_7 phase alone is insufficient for long persistence. Instead, these results unequivocally emphasize the B incorporation is necessary for extending persistence in S_4A_7ED phosphors.

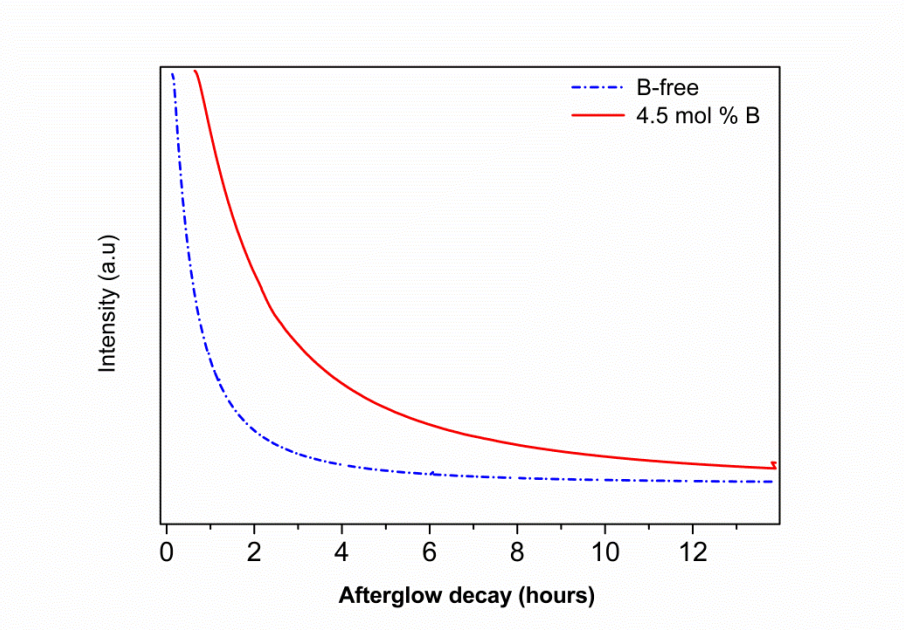

Figure 15 Afterglow decay curve of boron-free and boron-containing S_4A_7 phosphors obtained at 1300°C calcination temperature.

2.4. Disscussion

To elucidate the effect of boron, we first evaluated its impact on processing and the equilibrium crystal structure. Phase analysis by XRD showed that presence of boron facilitates the formation of a slightly sub-stoichiometric S_4A_7ED equilibrium phase. ICP revealed that Al/Sr ratio is consistent with the actual stoichiometric ratio of S_4A_7. The difference between the calculated cation ratios and the theoretical cation ratio could be due to preparation of the samples for ICP analysis. Complete dissolution of the powders may have not achieved during sample preparation and this might lead to inaccurate results by means of cation ratio. On the other hand, heat treatment was carried out by DTA using alumina crucibles, where B and Al might be incorporated into. On the other hand, the Eu and Dy amounts varied between *ca.* 0.6 -0.9 mol%, which is also close to the nominal value, 1 mol%.

Correlated thermal and phase investigations showed that incorporation of boron during synthesis facilitates the formation of S_4A_7 as the dominant equilibrium phase. According to thermograms obtained at 10°C min^{-1}heating rate (see Figure 1), there is a large exothermic region starts around 800°C and continues up to *ca.* 1200°C. To estimate the crystallization temperature of the S_4A_7 phase, we designated thermal stop points before and after the sharp exotherm at *ca.* 930°C. At 1150°C, we began to see the formation of the S_4A_7 phase, along with small fractions of SA_2 and SA_6. Rietveld analysis showed that the S_4A_7 content was 79.63% after 2 hours calcination, 88.55% after 5 hours and 99.46% after 10 hours of calcination duration. This result showed that 10 hours of calcination is necessary for complete crystallization of S_4A_7. It was also observed that, in the absence of the boron, the formation of the S_4A_7ED phase can only be achieved at 1300°C.

Phase determination of the samples obtained during TG-DTA investigations showed that the boron-containing powders contained *ca.* 99% S_4A_7 phase, whereas the boron-free sample contained only *ca.* 54% S_4A_7 phase, along with SA, SA_2 and SA_6. This is clear evidence that boron is facilitating the S_4A_7 phase formation by lowering the kinetic energy barrier.

Photoluminescence spectra of the compounds showed the typical features of S_4A_7 host lattice. The spectra were consistent with ones, for which two crystallographically non-equivalent Sr^{2+} sites were replaced by Eu^{2+}. Afterglow decay curves revealed that there are at least two trapping mechanisms, which controls the persistent luminescence duration. On the other hand, persistence luminescence of the S_4A_7 phosphors showed enhanced persistence behavior as boron amount was increased. However, without boron, luminescence could still be obtained, but persistence couldn't be observed.

2.5. Conclusions

Thermal and structural investigations showed that boron is necessary to obtain the S_4A_7 phase at lower processing temperatures of the modified Pechini method. Although the ICP results revealed that the Sr:Al ratio of the compound produced was consistent with the

theoretical stoichiometric value, the actual B content differed from the nominal value. The presence of B is necessary for significant afterglow persistence, although its presence alone does not ensure afterglow. Afterglow decay measurements reveal that the afterglow intensity was observable for ~14 hours in S_4A_7ED phosphors doped with boron and produced by the modified Pechini process.

CHAPTER 3:

A CRYSTAL STRUCTURE INVESTIGATION OF LONG PERSISTENCE B, Eu, Dy CO-DOPED $Sr_4Al_{14}O_{25}$ WITH ATOMIC SCALE RESOLUTION

3.1. Introduction

Among the different phases in strontium aluminate phosphors, two of them, the $SrAl_2O_4$ and the $Sr_4Al_{14}O_{25}$ ($4(SrO)\bullet 7(Al_2O_3)$, or S_4A_7) phase show extremely long persistence, in excess of 14 hours, when doped with Eu^{2+}, Dy^{3+}, and B. Much experimental work and some computational studies have been devoted to understanding what enables the extended afterglow. The current consensus is that the long persistence is due to the clustering of point defects. However, only global measurements of the structure and properties of these compounds have been performed. To image the point defects, we take advantage of the sub-angstrom probe in a spherical aberration-corrected scanning transmission electron microscope (STEM) to peer into the atomic arrangements. In this report, we present the results of atomic resolution annular dark-field and annular bright-field imaging in the STEM, showing the crystal structure and dopant positions.

The $Sr_4Al_{14}O_{25}$ compound is a low symmetry structure of Pmma/51 space group. Its orthorhombic unit cell has parameters of a = 24.7451 Å, b = 8.4735 Å, and c = 4.8808 Å with $\alpha = \beta = \gamma = 90°$. As shown in Figure 16, the structure is defined by parallel columns of AlO_4 and AlO_6 units. Cavities in this network are provided charge balance by Sr^{2+} cations. There are two non-equivalent Sr^{2+} sites, which are distorted octahedra: a 4*i* Wyckoff position (Sr1) and a 4*j* Wyckoff position (Sr2).[5, 28-30] The average Sr-O interatomic distance of Sr2 is 2.7561 Å and of Sr1 is 2.6356 Å. Their individual distances are 2.8735, 2.6734, 2.7923, 2.6542, 2.7541 Å, and 2.6079, 2.5118, 2.4936, 2.8309, 2.6982 Å, respectively. Ionic radii of Sr1 and Sr2 sites are 1.26 and 1.21 Å respectively[31]. In the S4A7 unit cell, there are also six crystallographically non-equivalent Al^{3+} sites, where Al1, Al2, Al3 makes distorted tetrahedra having average interatomic distances of 1.7347, 1.7377, 1.7494 Å , respectively, and Al4, Al5, Al6 sites makes distorted octahedra with 1.9108, 1.9003, and 1.9938 Å interatomic average distances. The individual Al-O distances and Wyckoff positions of each site are listed in Table 8.

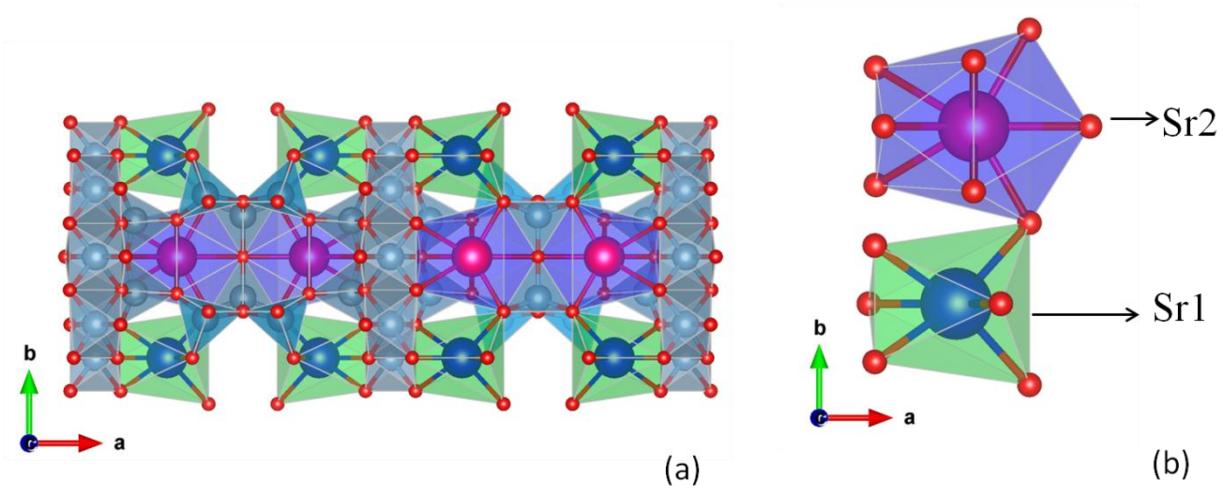

Figure 16 (a) $Sr_4Al_{14}O_{25}$ unit cell projected on (001) axis. (b) Individual Sr1 and Sr2 polyhedra shown on (001) projection.[32]

Table 8 Average and individual Al-O distances, coordination number and Wyckoff positions of 6 different Al^{3+} sites in S_4A_7 unit cell.

	Average Bond Length	CN	A-O bond distance	Wyckoff Site
Al1	1.7347 Å	4	(A1-O2) = 1.69131 (A1-O7) = 1.74205 (A1-O3) = 1.75772 (A1-O4) = 1.74788	8l
Al2	1.7377 Å	4	(A2-O1) = 1.71319 (A2-O2) = 1.77549 (A2-O8) = 1.72742 (A2-O6) = 1.73470	8l
Al 3	1.7494 Å	4	(A3-O4) = 1.79809 (A3-O3) = 1.72832 (A3-O3) = 1.72832 (A3-O9) = 1.74307	4k
Al4	1.9108 Å	6	(A4-O5) = 1.88101 (A4-O8) = 1.93084 (A4-O1) = 1.92046 (A4-O1) = 1.92046 (A4-O5) = 1.88101 (A4-O8) = 1.93084	4g
Al5	1.9003 Å	6	(A5-O1) = 1.92867 (A5-O1) = 1.92867 (A5-O5) = 1.84352 (A5-O1) = 1.92867 (A5-O1) = 1.92867 (A5-O5) = 1.84352	2c
Al6	1.9938 Å	6	(A6-O8) = 1.91781 (A6-O8) = 1.91781 (A6-O6) = 2.14569 (A6-O8) = 1.91781 (A6-O6) = 2.14569 (A6-O8) = 1.91781	2b

High angle annual dark field (HAADF) imaging at the atomic resolution gives direct chemical information on the projected atomic columns and the structure. The inherently high contrast in such images is due to the fact that the strength of scattering of incident electrons strongly correlates to the atomic number of the constituent atoms of the specimen. Thus, strong scatterers appear as bright spots, whereas weaker scatterers appear darker. In the case of HAADF imaging, the contrast in the image stems from the chemical nature of the atomic mass, as well as the density of atoms in an atomic column. Moreover, most of the electrons collected at high angles have been thermally scattered, which is one of the factors that is affecting the image contrast. Since local variations in the structure will be reflected by the intensity and its variation (*i.e.*, contrast) of the images, it is an advantageous technique for probing dopant atoms. However, HAADF enables one to probe heavier atoms in the structure, while being less sensitive to the lighter atoms. Annular bright field (ABF) imaging enables the simultaneous detection of light and heavier atoms at the same time. The ABF detector is positioned with the inner rim on the outer edge of the direct-scattering cone, *i.e.* the incident beam disk, collecting the outermost signals from the low solid-angle scattering region. This configuration allows the collection of low-angle scattered electrons from low-*Z* atoms.

However, a major difference between ABF-STEM images and HAADF-STEM images lies in the physics of image formation. While HAADF image contrast scales directly with atomic number, ABF-STEM image contrast arises from two components—coherent interference resulting in thickness-dependent phase variation and incoherent, inelastic scattering—, and the dependence of Z becomes more complicated. To understand this qualitatively, a relatively simple conceptual model was proposed by Findlay *et al.*[33] The probe positioned over the inter-columnar space passes directly through the hole in the ABF detector, serving as the specimen-free reference. The probe positioned over a column of light elements results in channeling of the electrons in the specimen-free, inter-columnar space, focusing the intensity in the forward direction through the hole in the ABF detector. In this case, the light-atom column appears darker than the background. On the other hand, the probe positioned over a column of heavy elements is strongly scattered over high angles, and is thus more susceptible to thermal diffuse scattering. The signal intensity is

thus also decreased below that of the background, although due to a wholly different mechanism.

ABF images can also be directly interpreted as HAADF images, such that intensity variations corresponding to atomic columns can be identified in terms of structure and chemistry. While thickness and defocus variations have limited effect over a wide solid-angle range in HAADF imaging, there is a somewhat stronger dependence in annular bright field image formation, thereby mandating image simulations for correct interpretation of experimental ABF images.[34]

In order to elucidate the crystal structure of Eu, Dy, and B co-doped S_4A_7, we adopted the following methodology: i) synthesize phase-pure S_4A_7EDB—verified by globally averaged analysis using Rietveld refined phase analysis of x-ray diffractograms; ii) analyze the theoretical crystal structure to identify optimal zone axes for imaging the distinct sub-lattices; iii) tilt onto low-index zone axes of interest; iv) record experimental images in AR-STEM; v) interpret the experimentally acquired images by simulating AR-STEM images from theoretical crystal structure models and instrumental parameters.

3.2. Experimental

3.2.1. Processing and Phase Determination of SA Phosphors

$((SrO)_4 \bullet (Al_2O_3)_7)_{0.98-x}Eu^{2+}_{0.01}Dy^{3+}_{0.01}B_x$ stoichiometric compounds with 4.5 mol% B and without boron, were synthesized by a modified sol-gel process, as described in detail in Chapter 2.

To determine, at the global level, the phases in the powder produced, we performed XRD measurements which have been described in Chapter 2. Rietveld phase analysis was performed on the XRD data for quantifying the phases present in boron-free and boron-

containing S_4A_7 compounds, and these results have already been discussed in detail in Section 2.3.2.

3.2.2. S/TEM Image Simulation by QSTEM

In order to determine the conditions of imaging and quantifying the microstructure $Sr_4Al_{14}O_{25}$ phosphors, we carried out quantitative image simulations by QSTEM[21], an image simulation software. This image simulation software gives control over both the crystal structure model and imaging conditions of the microscope.[21] The crystal structure file was obtained from FindIt software, contains the crystal structure information from the ICSD

Resolving ionic sub-lattices that may contain boron will explain the role of boron in extended persistence. Preliminary work for S/TEM experiments shall be planned rigorously beforehand, as it serves as a road map during microscopy session. Therefore, we have developed a four-step methodology*:* i) Determination of projection axes to resolve ionic sub-lattices, ii) S/TEM image simulations on determined zone axes, iii) tilting the crystal structure onto low indexed zone axes, and finally iv) S/TEM imaging of Sr, Al and O sub-lattices.

The ideal candidates would be along a low-index zone axis, where the Sr, Al, and O atoms are sufficiently separated, such that they would be distinguishable. No single axis was suitable for simultaneous imaging of all 3 sub-lattices. Instead, a {01*l*}-type of lattice was best for the Sr cation sub-lattice, while a {001} was more appropriate for resolving the sub-lattices of the lighter elements, Al and O.

As shown in Figure 17b, in the (001)-projection, Sr atoms are well aligned, and with Sr1-Sr1 inter-atomic distances *ca.* 5.548 Å, Sr2-Sr2 6.384 Å and they should be resolvable along this ZA using a *ca.* 1 Å-diameter probe. However, Al and O atom positions are close to each other, even they seem to overlap, thus, it would be difficult to resolve these sub-lattices.

In the (010)-projection (Figure 17a), Al and O atomic positions are more separated, *i.e.* more "resolvable", compared to other projection axis which makes it preferred over the other projection axis (see Figure 17a,b)

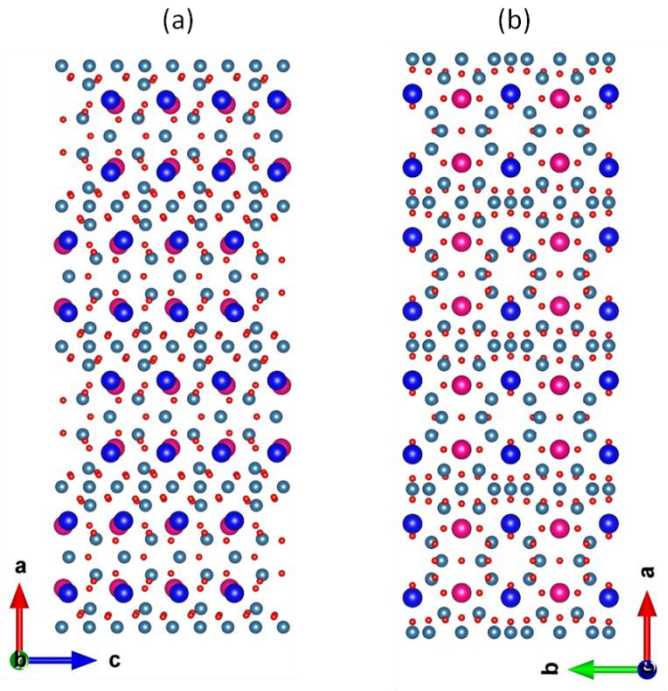

Figure 17 Projections obtained on (010) and (001) for the S_4A_7 unit cell.

In the (001)-projection, the Sr sub-lattice has a regular orientation, thus it is possible to resolve them clearly in this projection with *Z*-contrast imaging techniques. According to the ICSD database, there are two different Sr sites present in S_4A_7 phase, and we were expecting to resolve the difference between these two sites. Due to the fact that each different Sr site coordinates with a different arrangement of O ions, each has a different Debye-Waller factor, which defines their thermal vibrations with respect to its position in the crystal structure. Due to having well separated Sr columns in the (001) projection, tilting onto the <001>-zone axis is suitable for resolving the Sr sub-lattice by *Z*-contrast imaging.

In the (010)-projection, we aimed to resolve the Al and O ionic sub-lattices. In this projection, Al and O ions are positioned with sufficient separation from each other, in

contrast to other projections, which makes this projection ideal for resolving these sub-lattices. It should be noted that the two different Sr sites (indicated by pink and dark blue atoms) are slightly offset and form rows of Sr couples oriented in parallel in the projection plane, with alternating rows tilted in parallel with mirror symmetry, *i.e.*, with a mirror plane defined by the *b*- and *c*-axes. Although the Al and O sub-lattices do not show substantial differences, the slightly offset Sr atoms may be an advantage as they appear elliptical in projection. In the *Z*-contrast images, they would appear as bright elliptical features assembled in rows of alternating orientation.

Figure 18 shows (012)- and (013)-projections of S_4A_7 structure. Note that in the (012)-projection, columns of Sr cations are also aligned. However, in the (013)-projection, the Sr1 and Sr2 atomic positions are also resolvable, being positioned slightly further apart (see Figure 18b). Moreover, in the (013)-projection, an alternating periodicity in interatomic spacing between two neighboring Sr atoms has a distinct symmetry, facilitating identification of the zone-axis for aligning the crystal in the STEM, in addition to facilitating the atomically resolved imaging.

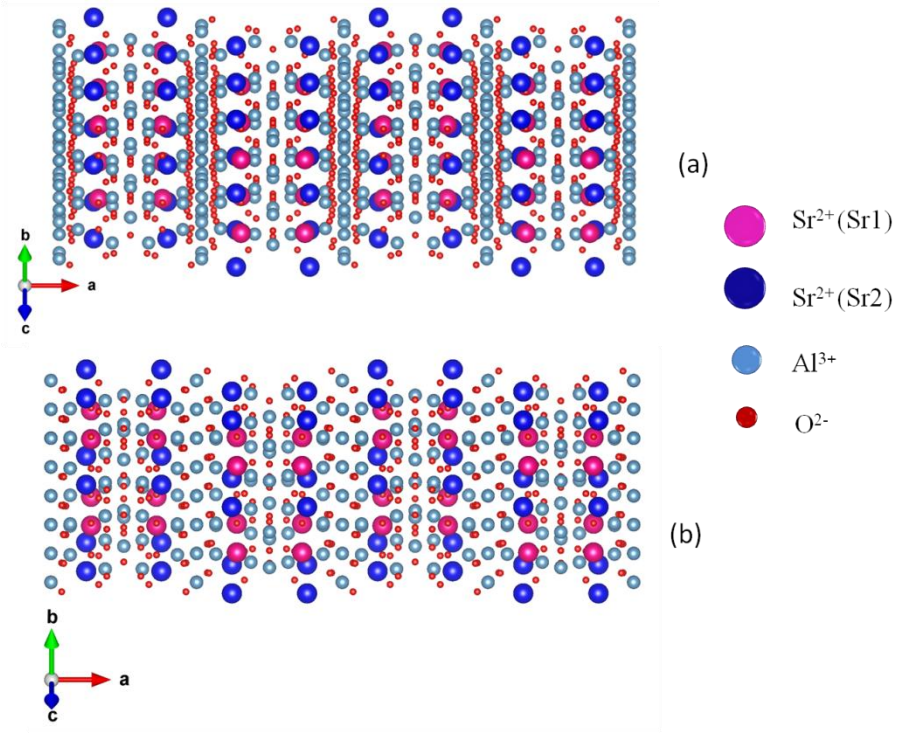

Figure 18 S_4A_7 supercell structure (a) in the (012)- and (013)-projections.

After we have defined the candidate zone axes determination in the previous step, we continued with quantitative S/TEM (scanning/transmission electron microscopy) image simulations of the S_4A_7 crystal structure. Simulation via QSTEM consists of three main steps: entering the crystal structure model, the image formation parameters, and the microscope settings. The QSTEM configuration window for STEM image simulation is shown in Figure 19.

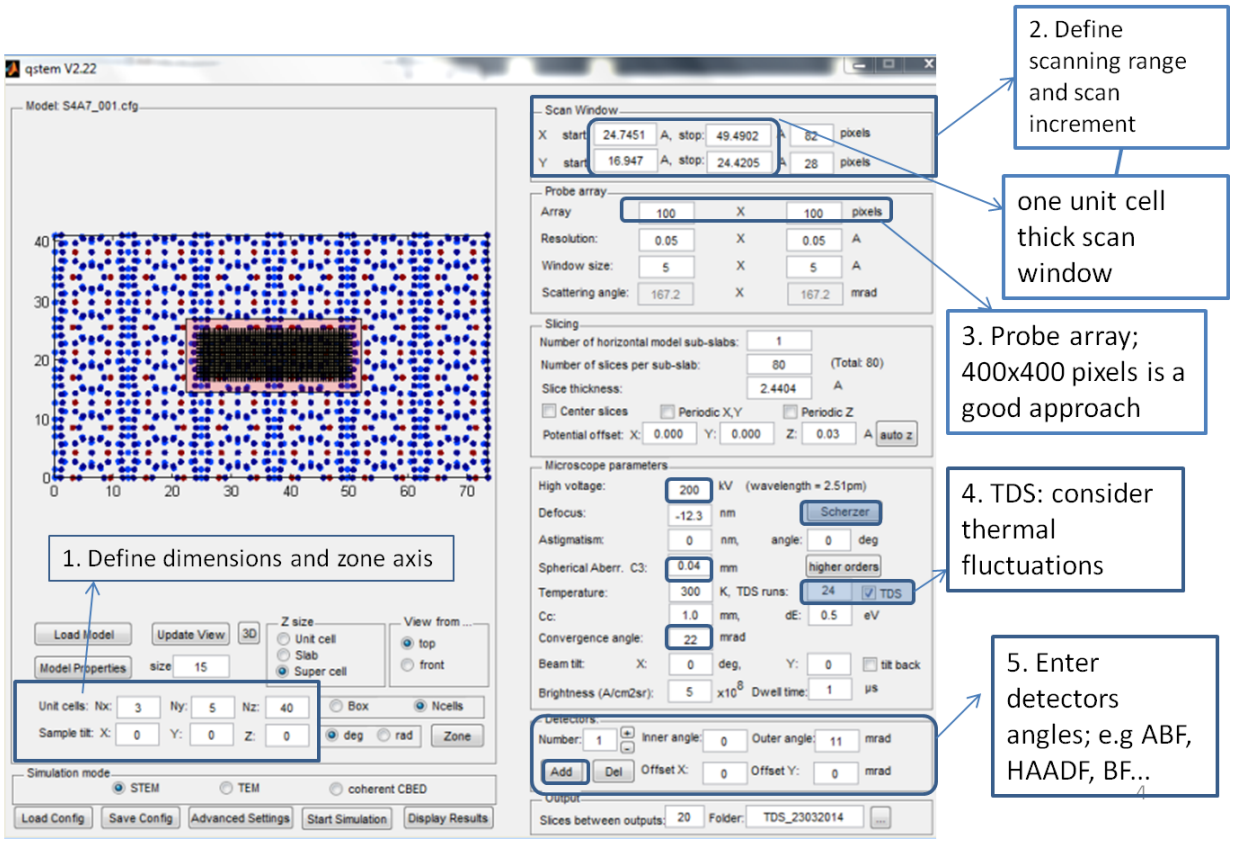

Figure 19 QSTEM image simulation: the configuration window annotated for showing the image simulation parameter sections for crystal structure, simulated image resolution, and actual microscope settings.

The crystal structure to be analyzed in QSTEM should be prepared in a special text file format, *.cfg, which is shown in Figure 20. This file contains the spatial atomic coordinates (x, y, z positions), the Debye-Waller factor, which defines the thermal vibration of an atom

relative to its position in the lattice and defines the effect of its coordination with the neighboring atoms, and the occupancy of each lattice position (see Figure 20). In part *a*, the structural model should be loaded and supercell parameters, such as size of the number of unit cell (the boundary of one supercell), can be adjusted. The next step is to define the boundaries of the scanning area, which we do in part *b*, where we define the scanning area of the probe and the probe resolution. The pixel size should be adjusted, such that each pixel forms a square (*e.g.* 0.3x0.3 $Å^2$). Boundaries of the scanning area should be adjusted such that each scan area equals to one unit cell dimension. This kind of sorting enables duplication of the simulated image, after quantitative image simulation finishes. As a final step (part *c*), the actual microscope configuration used during experimental image collection should be defined. All quantitative image simulations were obtained by the following microscope conditions: *32 mrad convergence angle, C_S=0.04 mm, C_C=1.4 mm*. These are defined to be the closest values to the actual configuration of our JEOL ARM 200CF TEM. Quantitative image simulations were carried out for 4 different zone axes: <001>, <010>, <012>, <013> and thermal diffuse scattering (TDS) was considered at each simulation for individual Sr, Al, and O ions. At larger scattering angles, the thermal diffuse scattering of electron waves involves large momentum transfer, resulting in transitions between Bloch states. Practically speaking, the observable effects are changes image contrast. Thermal diffuse scattering was accounted in the simulation by using Debye-Waller (DW) factors: 0.8228 and 0.464 for Sr1 and Sr2, respectively; 0.7525, 0.39, 0.6043, 0.4336, 0.4592, and 0.3223 for Al1, Al2, Al3, Al4, Al5 and Al6, respectively.[35]

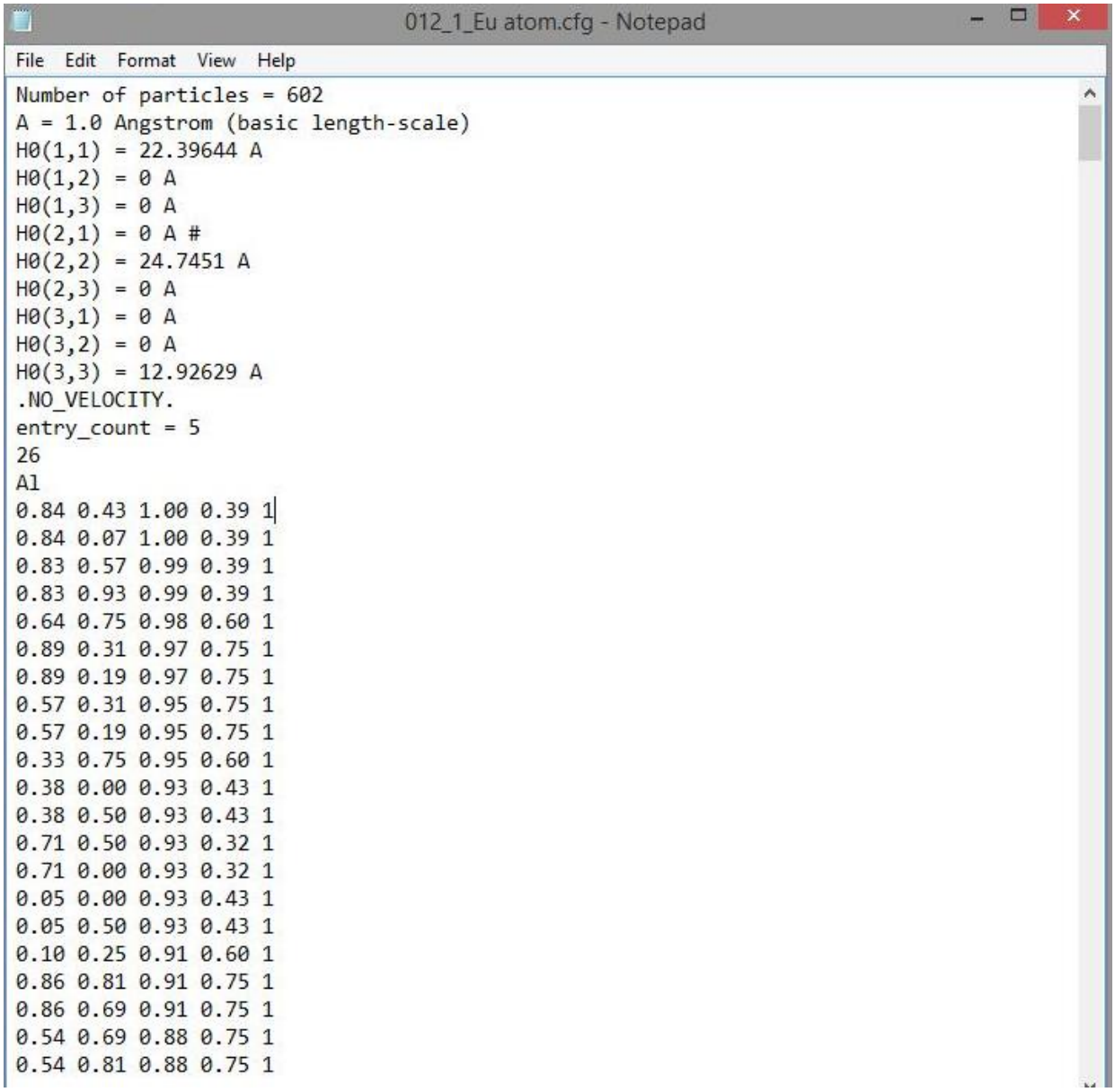

Figure 20 The crystal structure file in CFG format showing a supercell oriented along <012> zone axis.

STEM image simulations were performed with various detectors: BF, ABF, and HAADF detectors, in total eight different types of detectors were listed in Table 9. The sample thickness was increased from *ca.* 5 nm up to *ca.* 20 nm, in order to determine its effect on optimal imaging conditions such as image contrast, for resolving individual ionic sub-lattices.

Table 9 Detector types and corresponding inner/outer radius values used during quantitative image simulations.

Detector number/type	Inner radius (mrad)	Outer radius (mrad)
1 / BF	0	11
2 / BF	0	23
3 / ABF	20	80
4 / HAADF	90	170
5 / HAADF	45	180
6 / ABF	11	22
7 / HAADF	70	175
8 / HAADF	70	135

3.2.3. Imaging of S_4A_7 Phosphors at Atomic Resolution

After we simulated HAADF- and ABF-STEM images on the pre-determined zone axes, we generated a diffraction-space road map using Kikuchi patterns to help us on atomic resolution microscopy investigations. Our JEOL ARM 200CF is equipped with an ultra-high resolution pole piece, meaning that specimen tilting is limited to ±20°. With this limitation, we also identified the Kikuchi patterns for the zone axes nearby the ones of interest. Moreover, atomic resolution imaging would be performed on extremely thin regions, ones in which only spot diffraction patterns could be generated. These spot patterns would facilitate fine-tuning the tilting to as close along the zone axis direction as possible. In order to determine the zone axis geometry of the experimental diffraction patterns and HR/STEM images, we indexed the spot diffraction patterns using JEMS[20] software, which enables both the simulation of diffraction patterns from a known crystal structure at a specific zone axis.

To prepare a suitable specimen for atomically resolved STEM imaging, a lamella was cut from a single S_4A_7EDB particle using focused ion beam milling. High quality FIB-thinned lamellae are essential, with sufficiently and uniformly thin (*i.e*, 10 to 50 nm in thickness)

regions free of artifacts and with minimal processing-induced damage (i.e. amorphous areas). In the TEM, a sufficiently thin region was located on the FIB lamella, and the specimen was tilted onto a low-indexed zone axis which does not exceed the physical tilting limitation of the microscope.

3.2.3.1. Electron Diffraction Pattern Catalog and Indexing Experimental Diffraction Patterns

In order to simulate diffraction patterns on different zone axes, we first retrieved the crystal structure information from the ICSD database. The crystal structure information file contains the spatial position of each atomic site, the site occupancy, the Debye-Waller, Wyckoff position, etc. Upon retrieval of crystal information file from the ICSD database, it was uploaded into JEMS as shown in Figure 21.

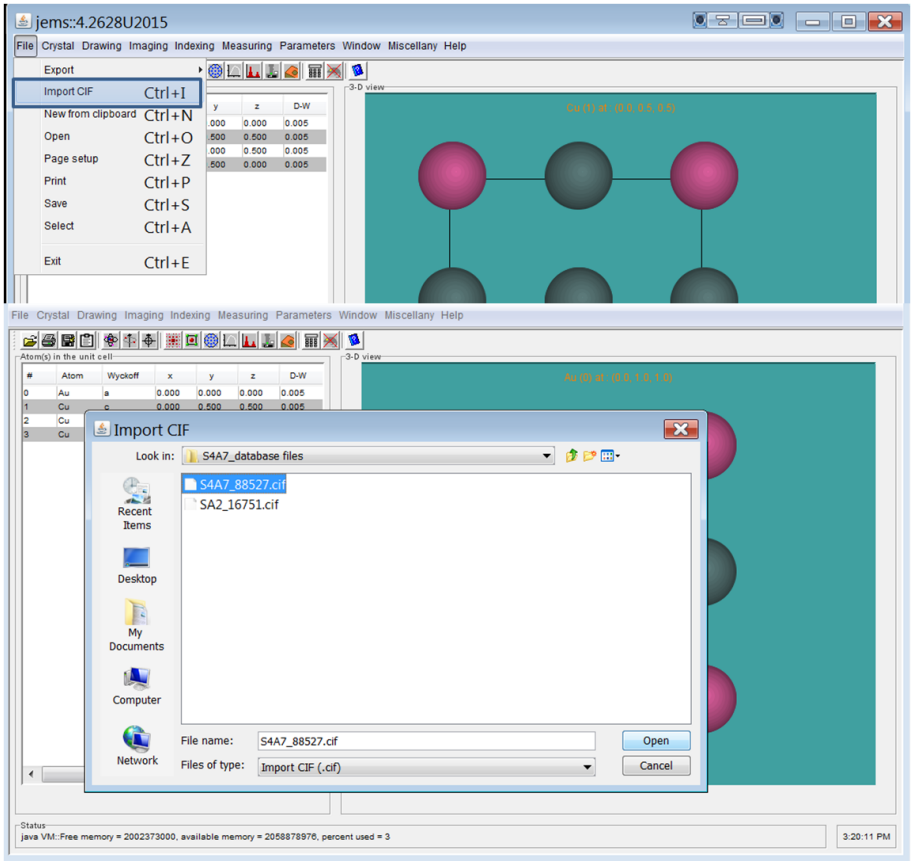

Figure 21 Loading the crystal information file and visualization of the unit cell.

After the structure was defined, we generated an electron diffraction pattern of the uploaded structure, viewed along a particular zone axis—typically, this would be one that is accessible for our specimen. By selecting “draw diffraction pattern” under the “diffraction” tab, we obtained a list of all reflections. This tool necessitated going through each zone axis reflection until a good match was found. This task was often done prior to commencing the microscopy sessions, in order to facilitate identification of location in the diffraction space.

In addition, we may also use the spot pattern indexing tool. It requires defining the distances between spots of the same order and angle between the two spots. Once the characteristics of the pattern to be indexed are defined, the database is checked for a match.

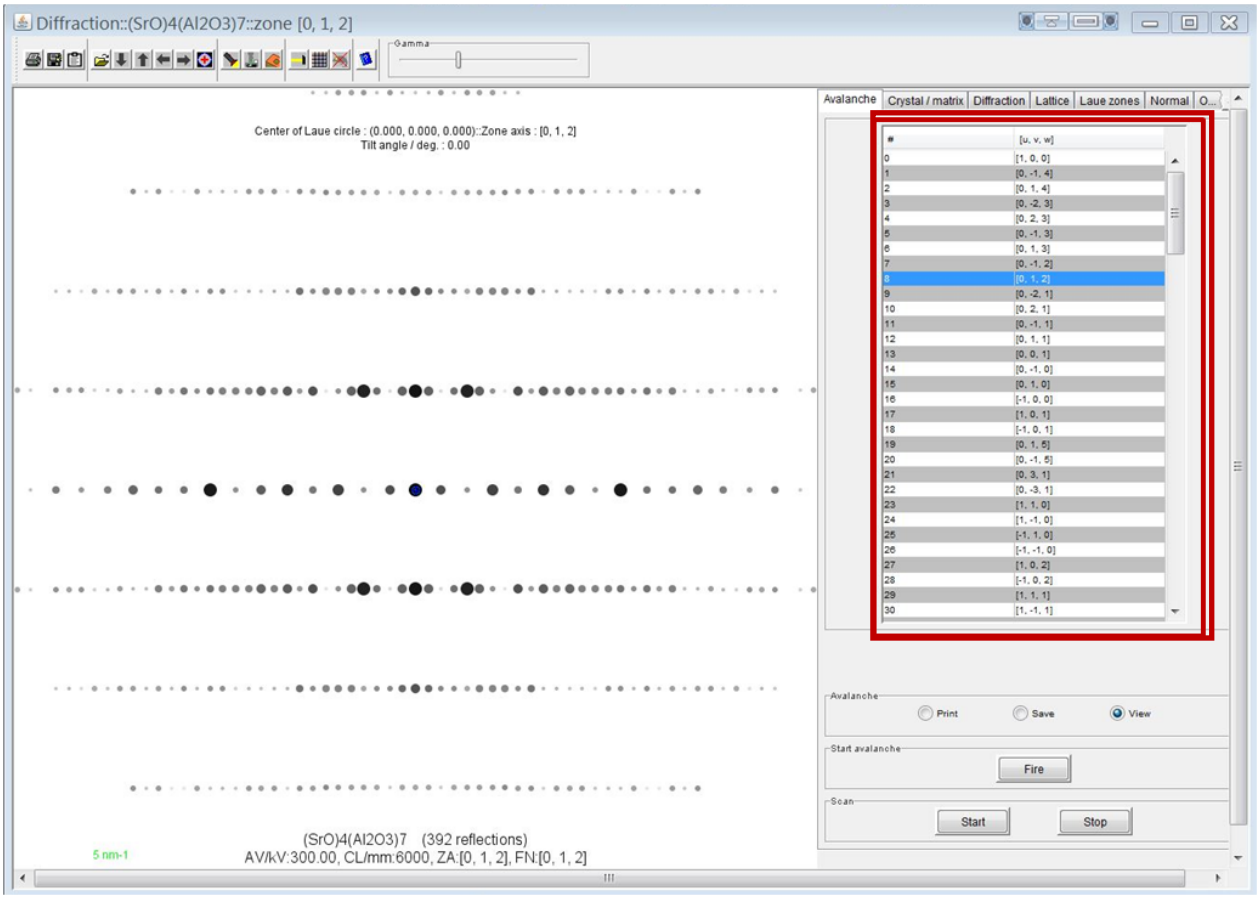

Figure 22 Experimental diffraction pattern and a list of possible reflections on different zone axes, highlighted with a red window.

Images of the experimental diffraction patterns (DP) obtained during microscopy sessions were uploaded to JEMS software to be analyzed and indexed. First, the image was uploaded as shown in Figure 23. Next, the microscope configuration parameters, such as accelerating voltage, camera length, were defined. The scaling of the diffraction pattern was additionally defined. Then, the two basis vectors that define the interplanar distances for the entire crystal (d, nm^{-1}) were chosen simply by centering the origin and dragging the arrow heads onto diffraction spots as demonstrated in Figure 24. Angles and distances can be manually corrected, along with the order of the diffracted spot. Once a mask has been displayed to confirm the definition of the crystal structure (*i.e.*, basis vector lengths and angles) and microscope conditions, the diffraction pattern indexing routine was launched. This tool enabled an automated search in the DP database and suggested the best-matching DPs to the user.

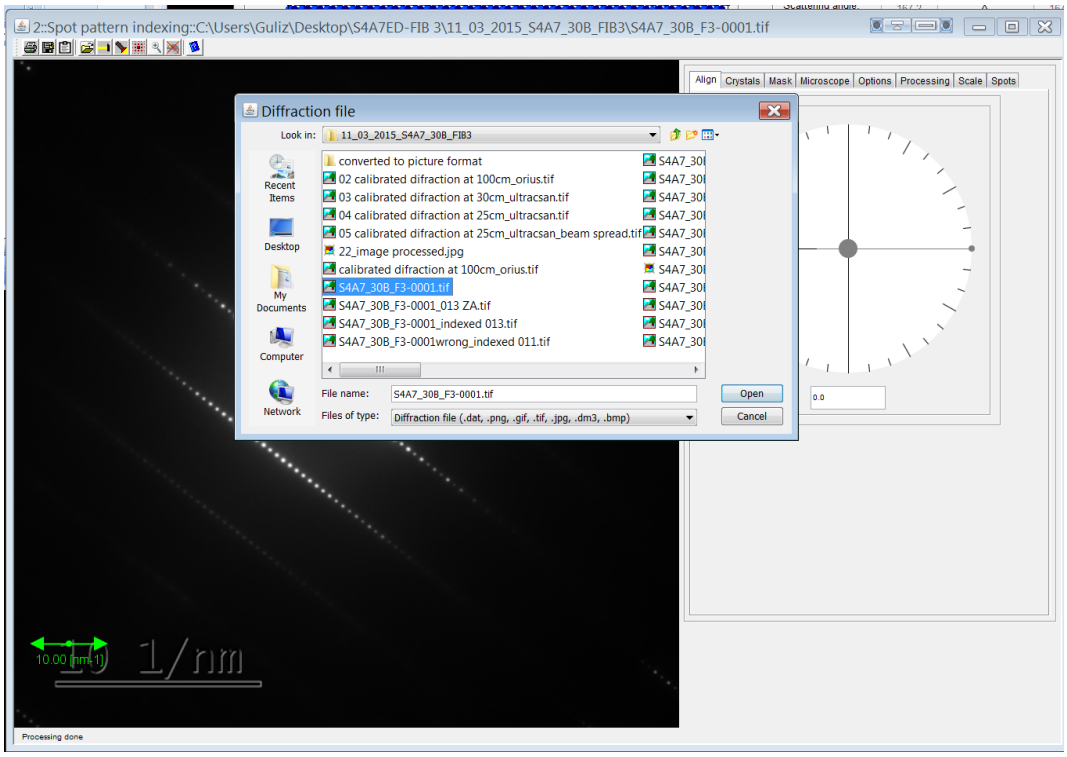

Figure 23 Uploading an experimental electron diffraction spot pattern on JEMS.

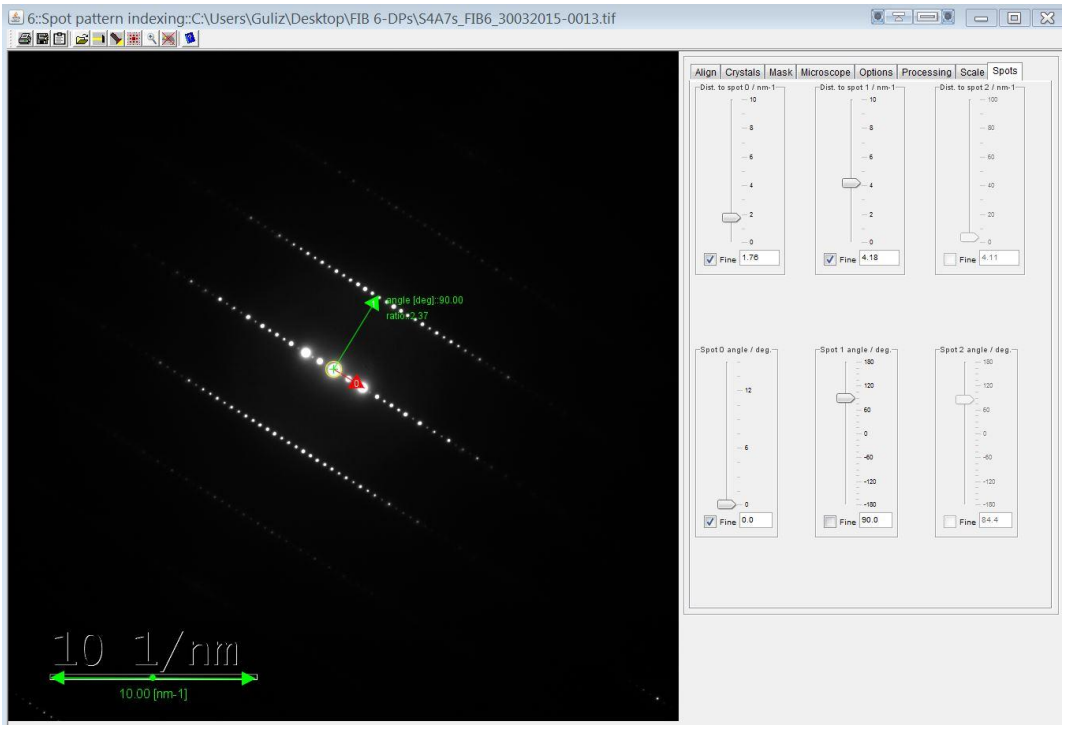

Figure 24 Defining interplanar spacing vectors and scale of the experimental spot diffraction pattern.

Each electron diffraction spot pattern obtained during the course of the work was indexed by using the procedure described above.

After we tilted onto the low-index zone axes <012> and <013>, we recorded atomic-resolution STEM images using a 1-Å probe size, a 50-µm condenser lens aperture, and a 3-mm bright field aperture.

Each HRTEM image was recorded with its corresponding diffraction pattern, in order to determine the ZA and to assess how close we were tilted onto the ZA. If the specimen was not tilted to exactly along a zone axis, the HRTEM/STEM images would not be interpretable via simulations. The optimal specimen prepared by FIB technique offered large regions of uniformly thin area for imaging of the crystal lattices under high spatial resolution with an interpretable contrast transfer function.

After we tilted the specimen onto the <012> zone axis and formed high resolution TEM images, we switched to scanning TEM (STEM) mode and continued to analyze the specimen. In this imaging mode, the specimen was scanned with a fine probe size (2.5 pm). Using different detector configurations such as bright field and dark field detectors, it would be possible to obtain chemical information from the crystal structure at the atomic level.

In this course of the work, we used two different annular detectors for image formation: the annular bright field detector (ABF) and high angle annular dark field (HAADF) detector.

3.3. Results

Lamella samples were prepared by focused ion beam (FIB) thinning from a single powder particle. Single powder particle and its FIB thinned lamella were given in Figure 25a and 25b, respectively.

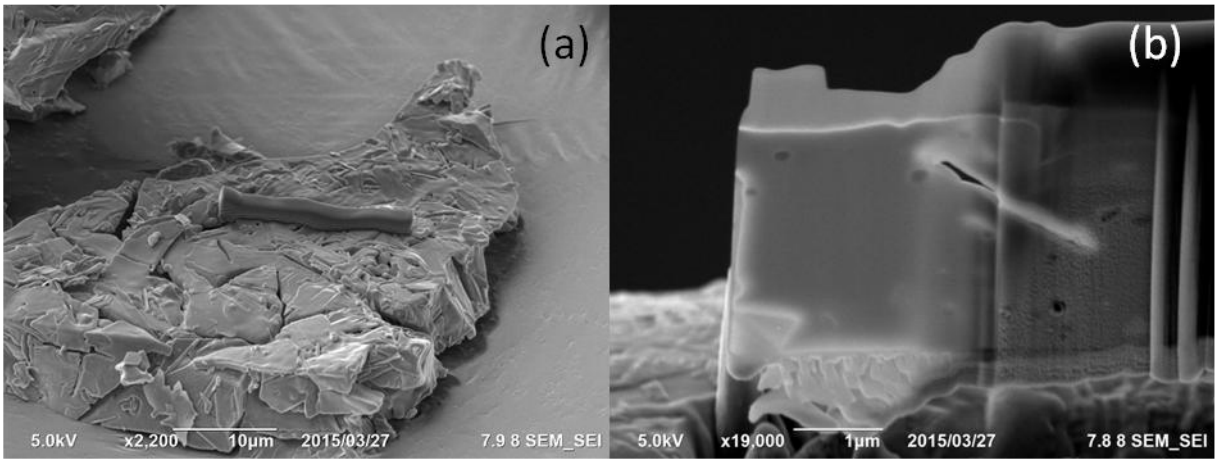

Figure 25 **(a)** Boron-free Eu^{2+}, Dy^{3+}co-doped S_4A_7 powder particle and (b) FIB thinned lamella prepared from powder particle.

HRTEM images and corresponding diffraction patterns of S_4A_7 phosphors with and without B specimen were given in Figure 26.

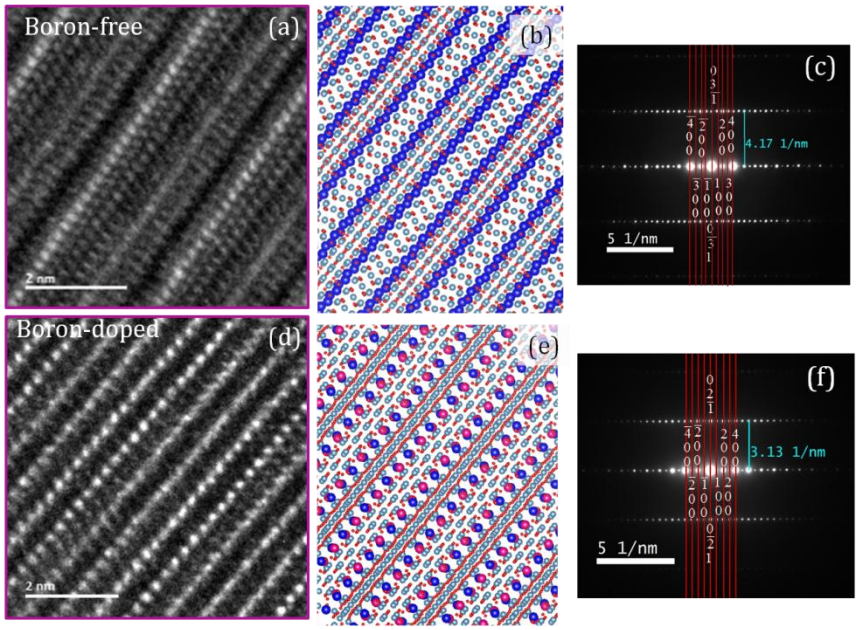

Figure 26 HRTEM image of S_4A_7 specimen **(a)** without B (b) its simulated structure with its diffraction pattern for the **(c)** <013>-zone axis. (d) B-containing S_4A_7 specimen's HRTEM image, along the <012> zone axis, (e) its simulated structure and (f) diffraction pattern

An overview image of the specimen imaged with ABF is shown in Figure 27a, and the corresponding HAADF image is shown in Figure 27b. For these images, we used an 8-cm camera length with a 30-micron condenser lens aperture and a 3-mm BF aperture.

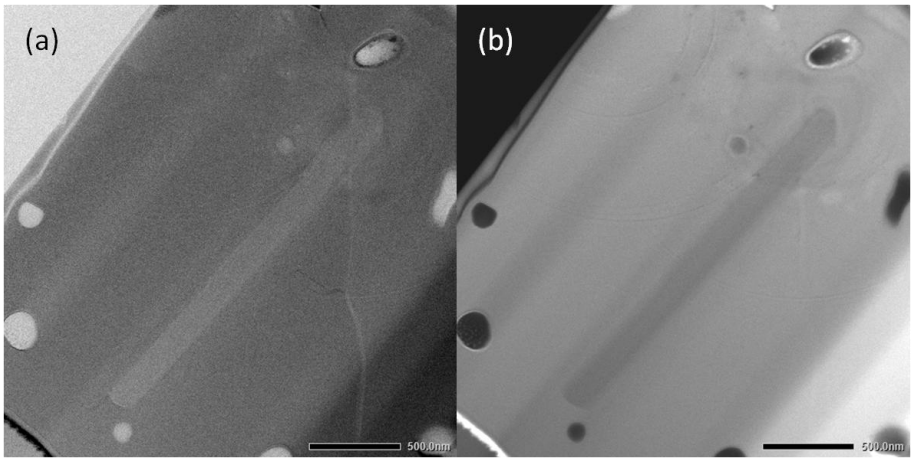

Figure 27 Overall view of boron-free FIB thinned specimen obtained by (a) ABF and (b) HAADF detectors.

Imaging and diffraction analysis in the TEM showed that without B present, the SA particles consisted of aggregates of many grains, including some plate-like grains (see Figure 28 the grain labelled "1"). However, when B is present, such plate-like grains were not observed. Indexing the selected area diffraction pattern from the more equiaxed grains (the grains labelled "2" and "3" in Figure 28) revealed that these were of the orthorhombic S_4A_7 phase, consistent with spot electron diffraction patterns of boron-doped $Sr_4Al_{14}O_{25}:Eu^{2+},Dy^{3+}$ (see Figure 26).

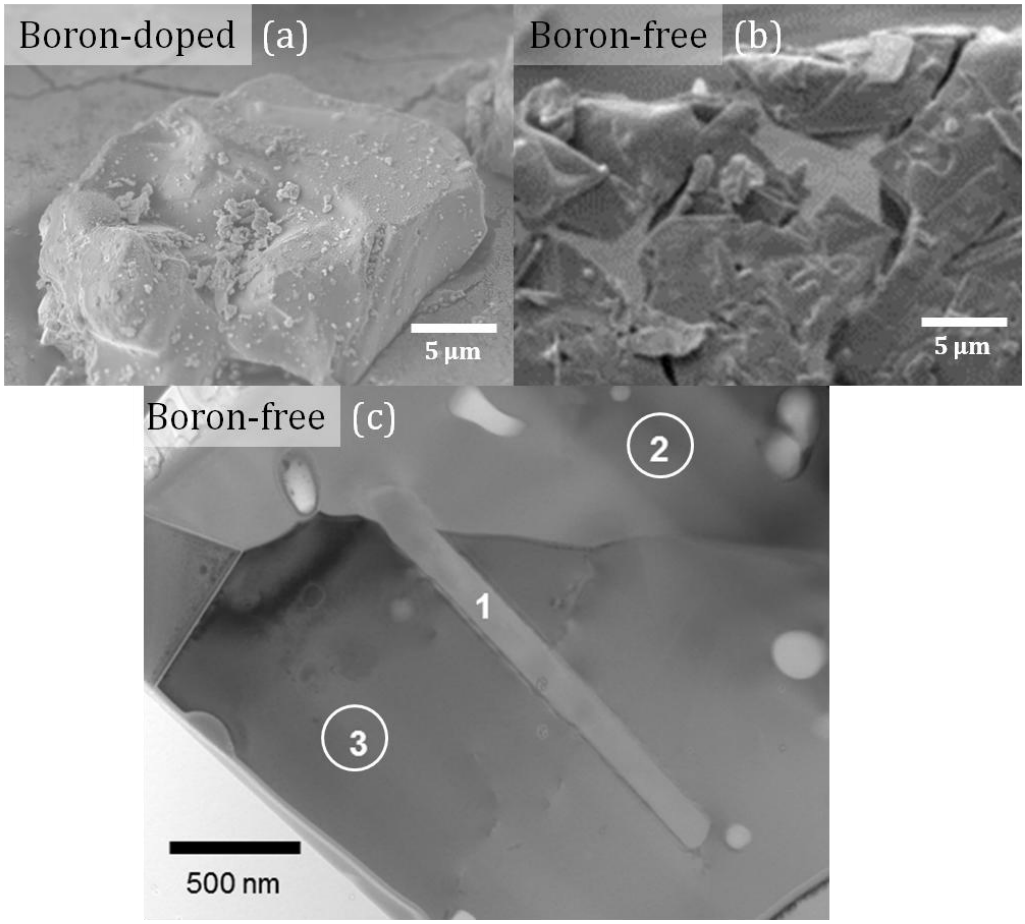

Figure 28 (a) An SEM image of B-doped and (b) B-free S_4A_7ED particles. (c) A bright-field TEM image showing the polycrystalline microstructure of the boron-free S_4A_7ED compound. Note the plate-like grain 1, which is not present in B-doped specimen; the equiaxed S_4A_7 grains at points 2 and 3.

In order to interpret the experimentally obtained AR-STEM images, we performed quantitative AR-STEM image simulations for each of the following axes: <001>, <010>, <012>, and <013> zone axes. The detector settings are summarized in Table 9. We varied sample thicknesses and detector solid angles, in order to determine the optimal imaging conditions for resolving each ionic sub-lattice. The crystal structure model was prepared by importing the crystal information file, which was exported from the ICSD database as a *.cif file. Then, the structure file was imported to the JEMS software, and the zone axis orientation was determined (*i.e.*,<012>). At the end of this process, an orthogonal supercell was generated, and saved using a *.cfg file format (see Figure 20). Annular bright field and

high angle annular dark field (*Z*-contrast) simulations obtained for <001> and <010> zone axes are presented in Figure 29 and 30 By using the HAADF detector over a collection solid angle range of 90-170 mrad, we expected to be able to resolve the Sr sub-lattice. For the Al-O sub-lattice, we simulated images formed from ABF detected signals over a collection solid angle range of 11-12 mrad. The conditions used for simulating the images, including thermal diffused scattering, were 32 mrad convergence angle, C_S = 0.04 mm, C_C= 1.4 mm, -12.3 nm Scherzer defocus, 0.5 eV energy resolution, and a 200 Kev accelerating voltage.

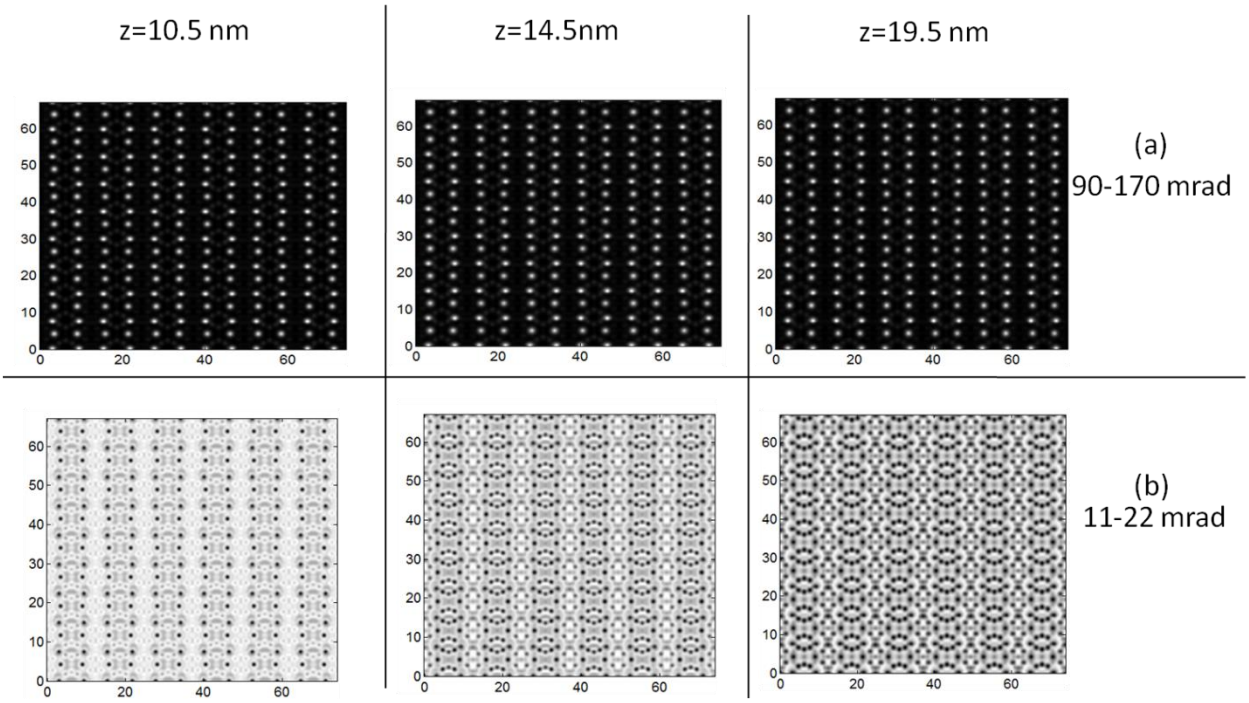

Figure 29 STEM image simulations for S_4A_7 along <001> zone axis from signals collected by (a) the high angle annular dark field detector with 90-170 mrad angle and (b) the annular bright field detector with 11-22 mrad.

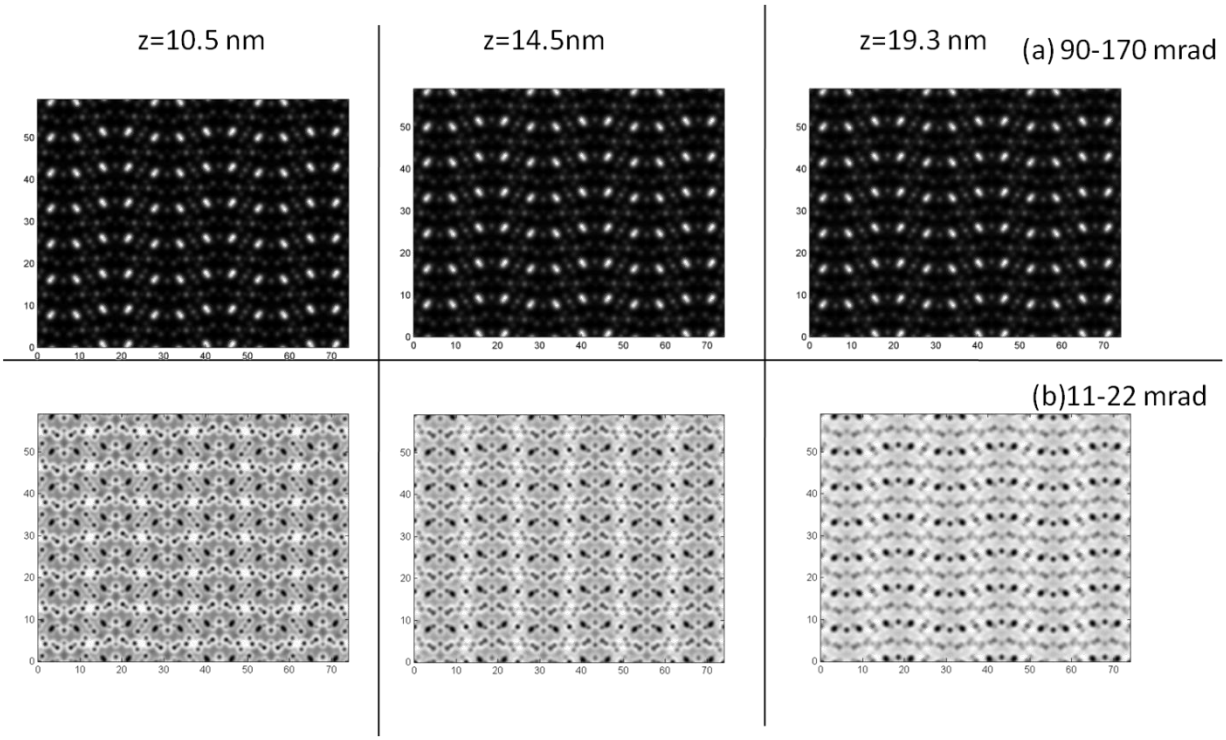

Figure 30 STEM image simulations obtained for S_4A_7 along the <010> zone axis generated by (a) the high angle annular dark field detector with 90-170 mrad angle and (b) the annular bright field detector with 11-22 mrad.

Two more supercells were generated using the JEMS software, along the <012> and <013> zone axes, containing 602 and 344 atoms respectively. Eu is known to enter the S_4A_7 crystal structure by replacing Sr atoms and becomes the optically active Eu^{2+} center upon reduction of Eu^{3+}. Since Eu atoms are heavier than strontium atoms (Z_{Sr} = 38, Z_{Eu} = 63), Eu atoms should in principle appear brighter in *Z*-contrast imaging. In order to see how the Eu dopants would appear in an S_4A_7 crystal structure using HAADF- and ABF-STEM imaging techniques, we first generated a crystal structure model containing Eu-dopant atoms, and simulated the images for a <012>-ZA-oriented supercell structure. One Sr cation at the position (x = 0.41, y = 0.62, z = 0.82) was replaced by one Eu atom, and STEM images were simulated for HAADF and ABF detectors. Because a pure S_4A_7 unit cell structure contains 86 atoms, and considering that we doped the structure with 1 mol% Eu, corresponding to 1 Eu ion per 100 atoms, each unit cell may contain only 0.86 Eu ions per

unit cell. Therefore we considered only one Eu atom in a unit cell while performing the simulations. The simulated STEM micrographs are shown in Figure 31-34.

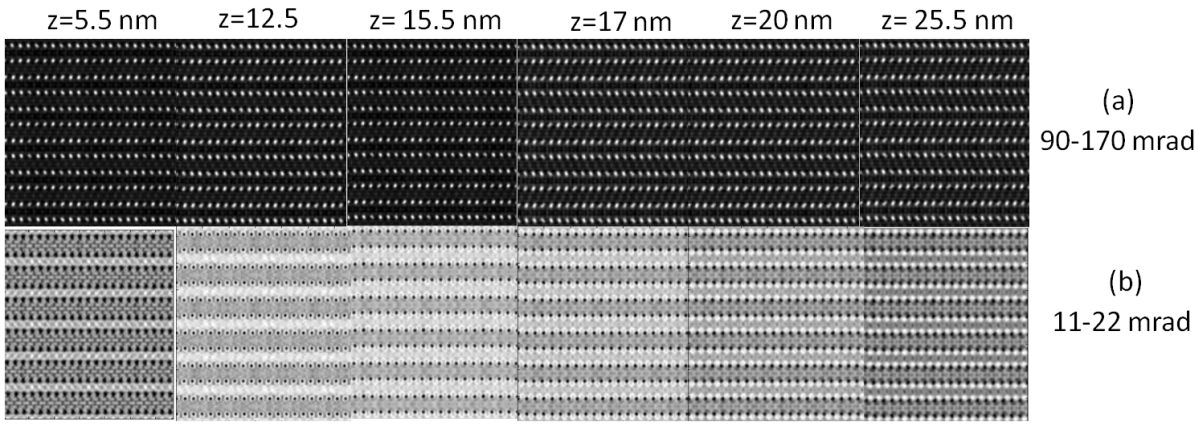

Figure 31 (a) HAADF and (b) ABF image simulations of undoped (pure) S_4A_7 structure as viewed in the (012)-projection.

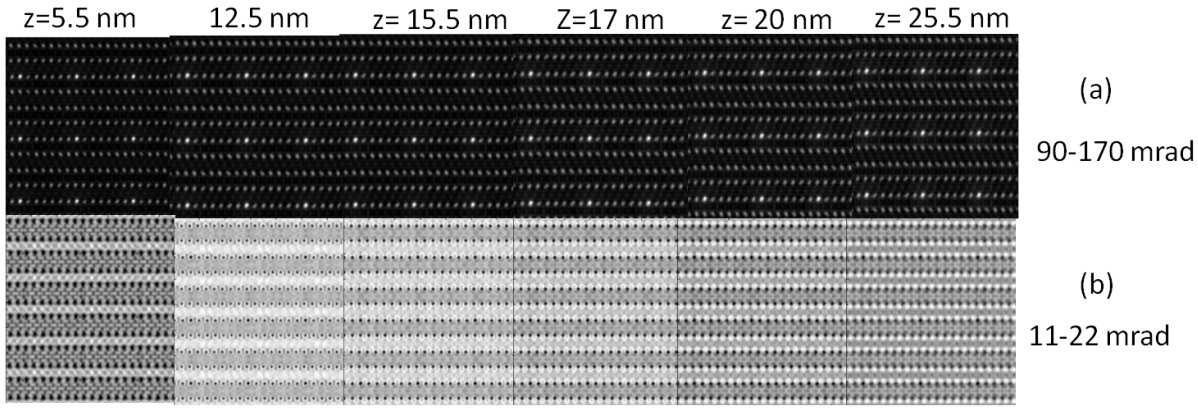

Figure 32 (a) HAADF and (b) ABF image simulations of the Eu-doped S_4A_7 structure as viewed along the (012)-projection.

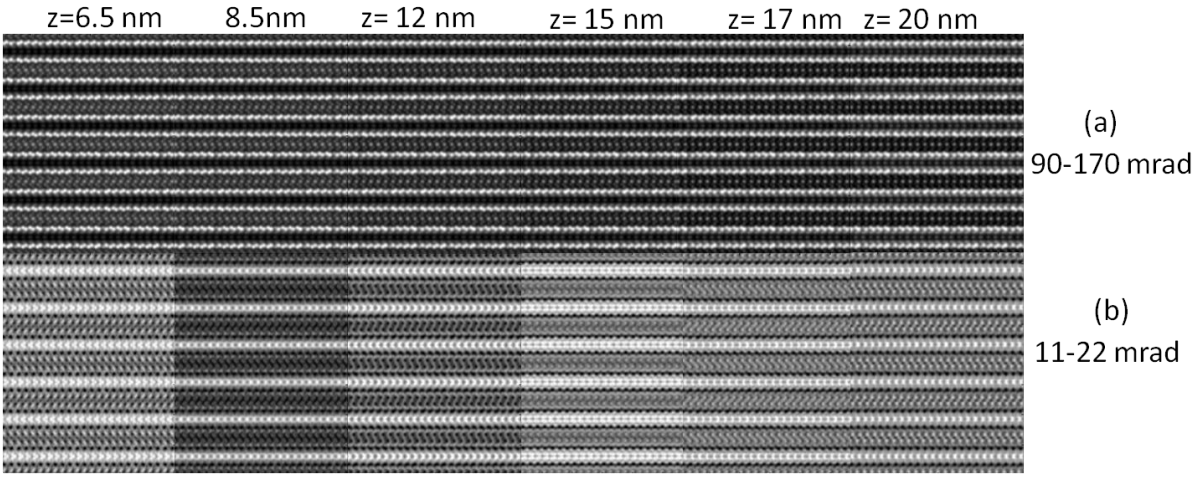

Figure 33 (a) HAADF and (b) ABF image simulations of the undoped S_4A_7 structure as viewed along the (013)-projection.

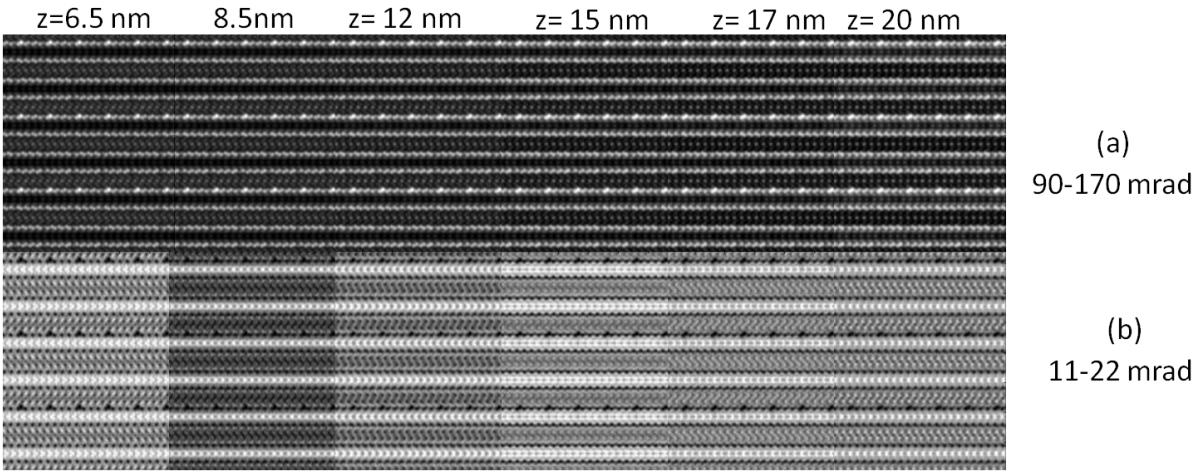

Figure 34 (a) HAADF and (b) ABF image simulations of the Eu-doped S_4A_7 structure as viewed in the (013)-projection.

The specimen was tilted onto a nearby low-index zone axis during HRTEM imaging, in order to resolve most clearly individual atomic columns. As predicted, the Sr atoms must appear brighter in the HAADF image compared to Al, O, and B, because Sr is a heavier atom thus electrons should scatter at higher angles Experimentally obtained HAADF and ABF images were compared with simulated images for interpretation and corresponding analysis results for (012) and (013) projection axes were given Figure 35 and Figure 36.

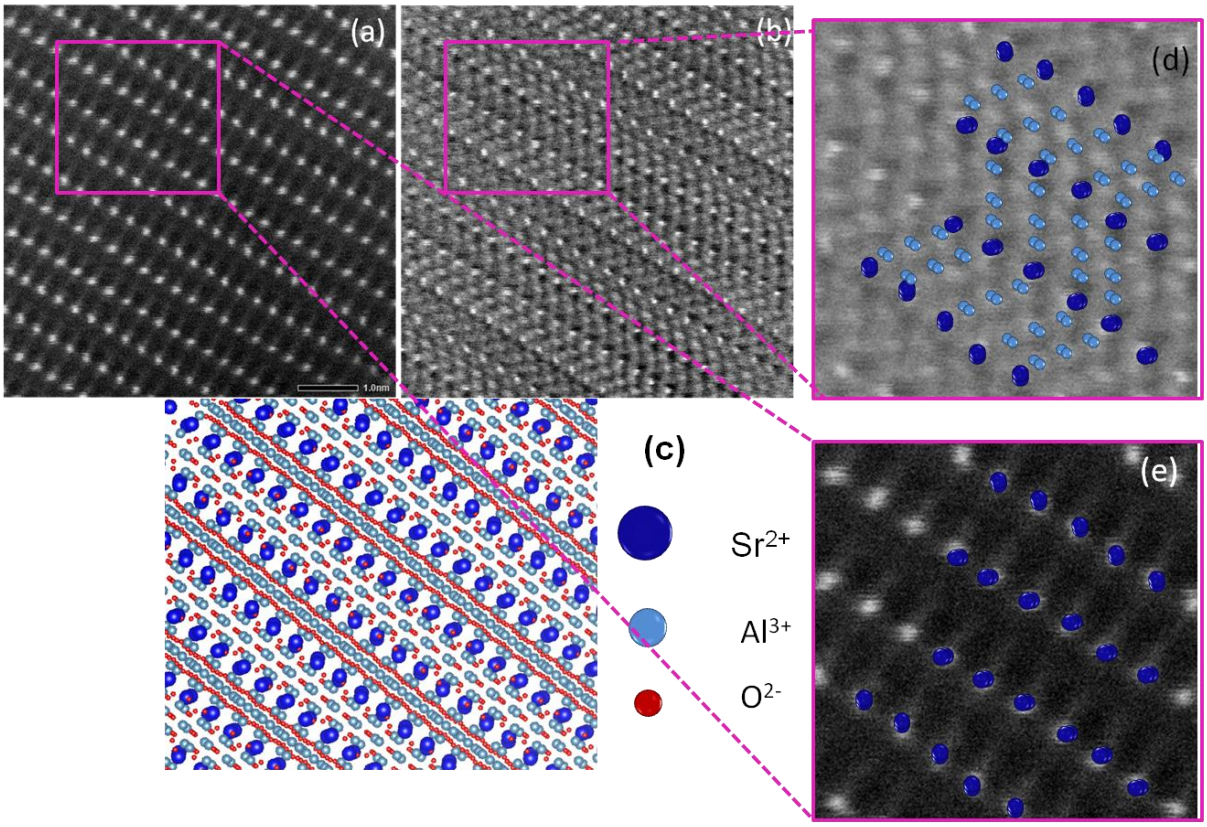

Figure 35 STEM micrograph of boron-containing S_4A_7 specimen, viewed along the <012> zone axis, obtained by (a) HAADF, and (b) ABF detectors, and (c) simulated S4A7 structure viewed along the <012>. (d) Sr and Al atoms shown on inverted ABF image, (e) Sr atoms shown on HAADF image. Note that the ABF image contrast is inverted.

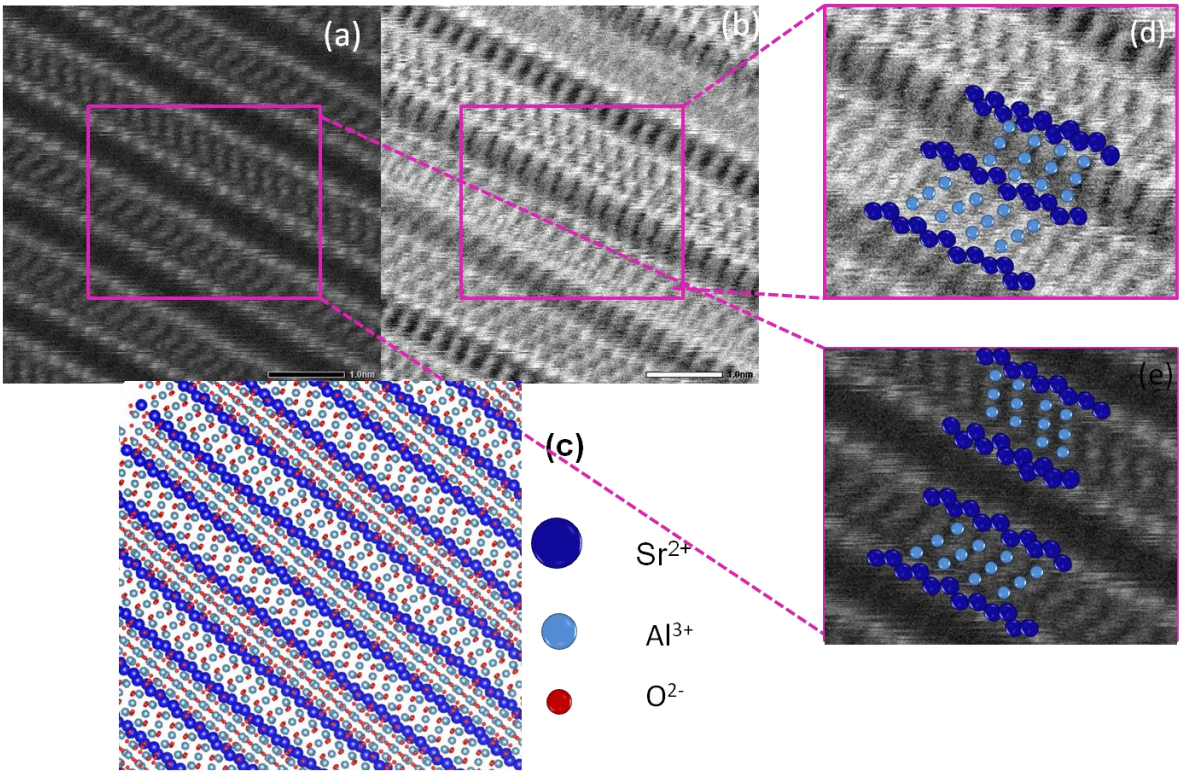

Figure 36 STEM micrograph of the boron-containing S_4A_7 specimen, viewed along the <013> zone axis, obtained by (a) HAADF, and (b) ABF detectors, and (c) simulated S_4A_7 structure viewed along the <013>, (d) Sr and Al atoms shown on the ABF image, and (e) HAADF image. Note that the ABF image contrast is inverted.

Along both the <012> and <013> zone axes, the two non-equivalent Sr sites are slightly offset, thus both sites should be identifiable, even though their projected positions are very close (see Figure 18, Figure 31, Figure 32, Figure 33, and Figure 34). Each Sr site has a different Debye-Waller factor, which in principle should be closely related to their intensities in Z-contrast imaging. When viewed along the zone-axis normal, the offset Sr sites appear as elongated (elliptical shaped) atoms on both axes. However, the <013> axis is tilted at a slightly lower angle around a-axis, and projections of neighboring Sr atoms are positioned more closely. Distance between Sr2-Sr2 (6.384 Å and 6.093 Å) atoms does not change since the crystal was only rotated around a-axis (see Figure 18). The angle between (001) and (012) planes can be found by their dot product and it is calculated to be 26.5°.

When rotated around a-axis, Sr1-Sr1 projected distance becomes closer and the distance changes from 4.27 Å to $4.27 \times \cos(26.5) = 3.82$ Å (see Figure 18 for comparison). On the other hand, for rotating the (001) plane to (013) plane, 18.4 ° is needed. When rotated around a-axis by 18.4°, distance between two Sr1 sites becomes 4.05 Å. In Figure 37, an atomically resolved *Z*-contrast image of a boron-free S_4A_7ED compound along the <013> zone axis is shown, and a row of Sr atomic columns is indicated with a red window. The corresponding intensity profile (see Figure 37) shows that, the two non-equivalent Sr sites could clearly be resolved.

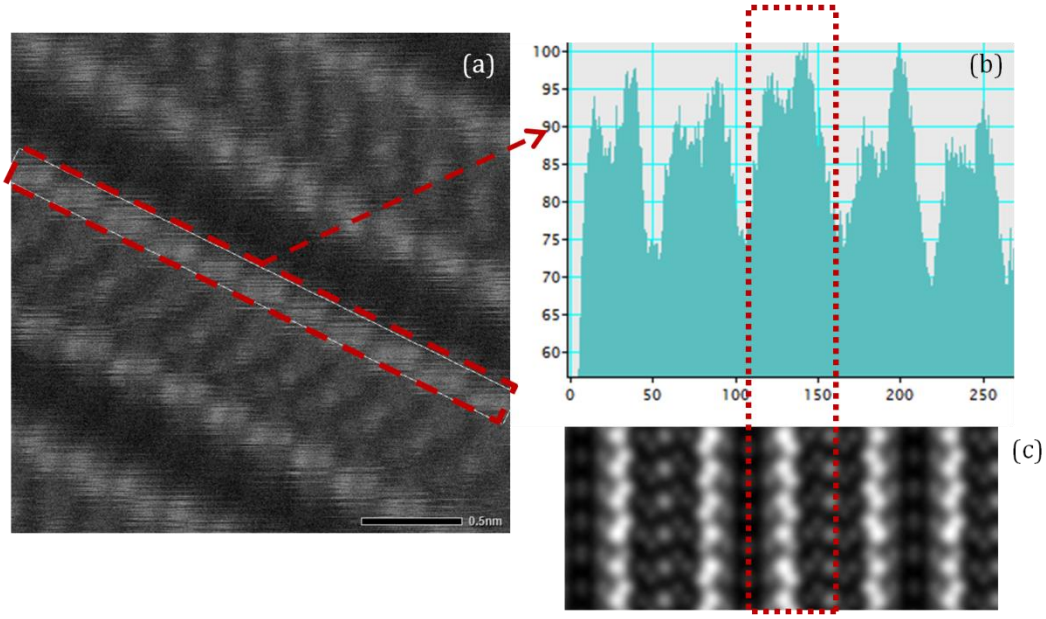

Figure 37 (a) HAADF micrograph of boron-free S_4A_7ED specimen oriented on <013> zone axis. Red highlighted region showing (b) the intensity profile Sr atomic column where two slightly off, different Sr sites could be resolved. (c) Simulated HAADF image of S_4A_7 crystal structure on <013> zone axis, to show the correlation between (a) and (b).

Experimentally obtained HAADF and ABF images were compared with simulated images for interpretation and the corresponding analysis results for the (012) and (013)-projections are shown in Figure 38 and Figure 39. The simulated HAADF images along the <012> and

<013> zone axes in Figure 38 and Figure 39, respectively, each contains one Eu atom occupying a Sr site. To facilitate identification of this Eu atom, a circle indicates the location, where the contrast difference is readily evident.

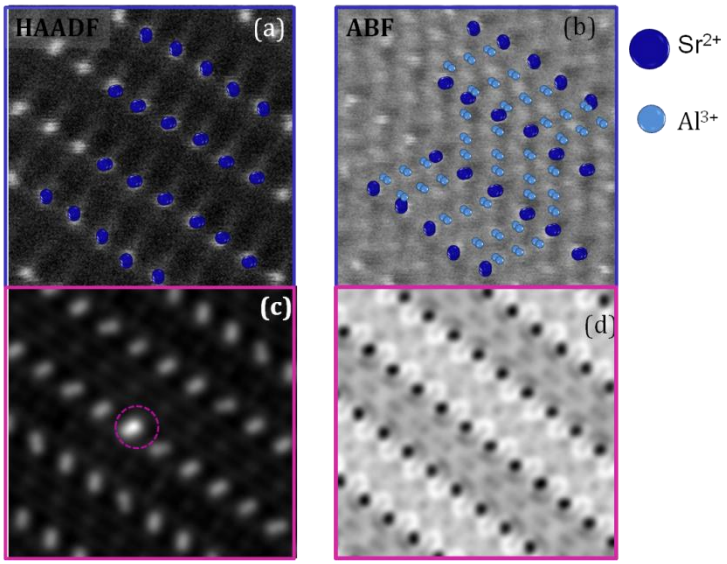

Figure 38 (a) HAADF and (b) ABF images of boron containing S_4A_7ED compound, compared with (c) HAADF and (d) ABF image simulations containing Eu-dopant atoms, all as projected along the <012>-zone axis.

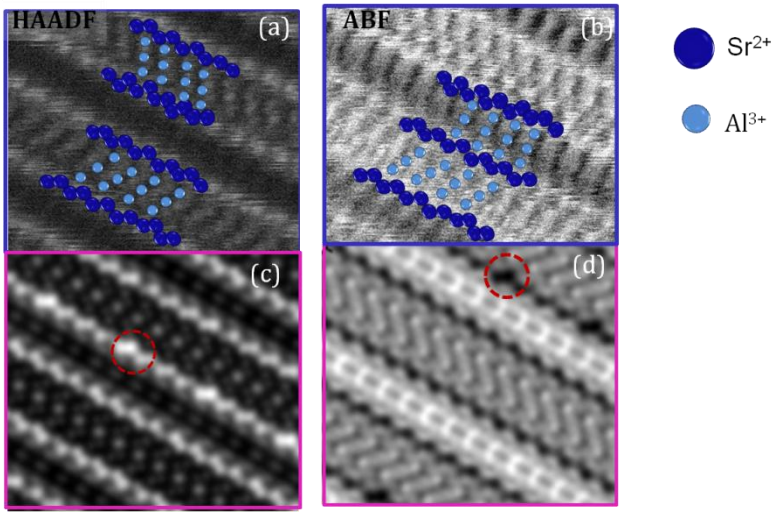

Figure 39 (a) HAADF and (b) ABF images of boron containing S_4A_7ED compound, compared with (c) HAADF and (d) ABF image simulations containing Eu-dopant atoms, all as projected along the <013>-zone axis.

We further analyzed the HAADF image of a boron-containing specimen projected on the (012) and located one atom on the Sr atomic column. The measured distances between Sr atoms on column #1 and #2 is found to be 6.4 Å which is consistent with the tabulated Sr2-Sr2 distance value of the S_4A_7 structure. Figure 39 shows the intensity profile of Sr atoms on column shown with rectangular regions #1 and #2 where column #1 contains an atom with an detectably higher intensity compared to other atoms in this and consequent column, #2. The average intensity of Sr atoms on column assigned as #1 was calculated to be 32721 ± 1362 whereas Sr atomic column assigned as #2 has an average intensity of 32393±1119.

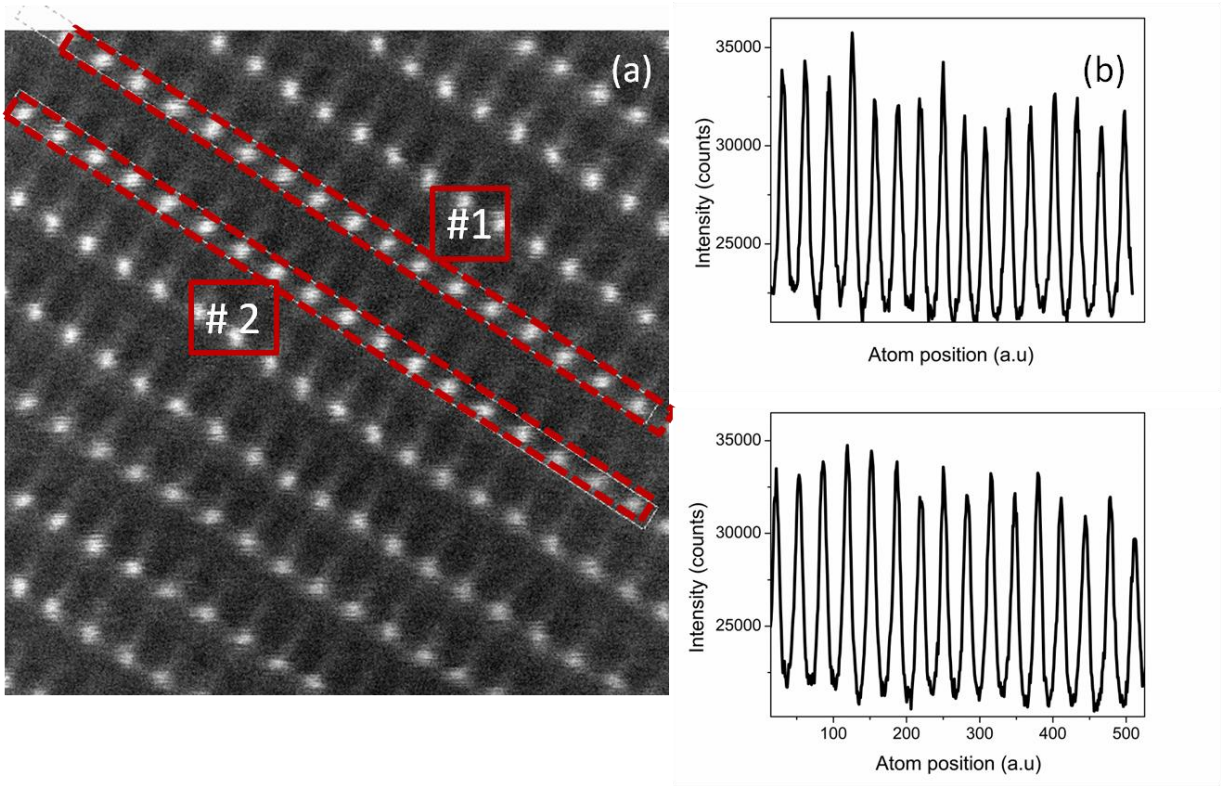

Figure 40 **(a**) HAADF image of B-containing S_4A_7ED on <012> zone axis projection. (b) Intensity count profile of rectangular region #1, and (c) #2.

To analyze the contrast difference, an intensity profile was obtained along the column #1 and assigned as ROI#1. We also compared the intensities of two other Sr-site atoms along the scanning direction that were assigned as ROI#3 and ROI#4 (see Figure 41). Close inspection of their intensity profiles revealed that atom ROI#2 also has relatively higher

intensity than the others. Since Eu (or Dy) atoms have higher atomic number compared to Sr atom, the intensity of Eu-dopant atom should appear in higher intensity, which also have been demonstrated by QSTEM simulations.

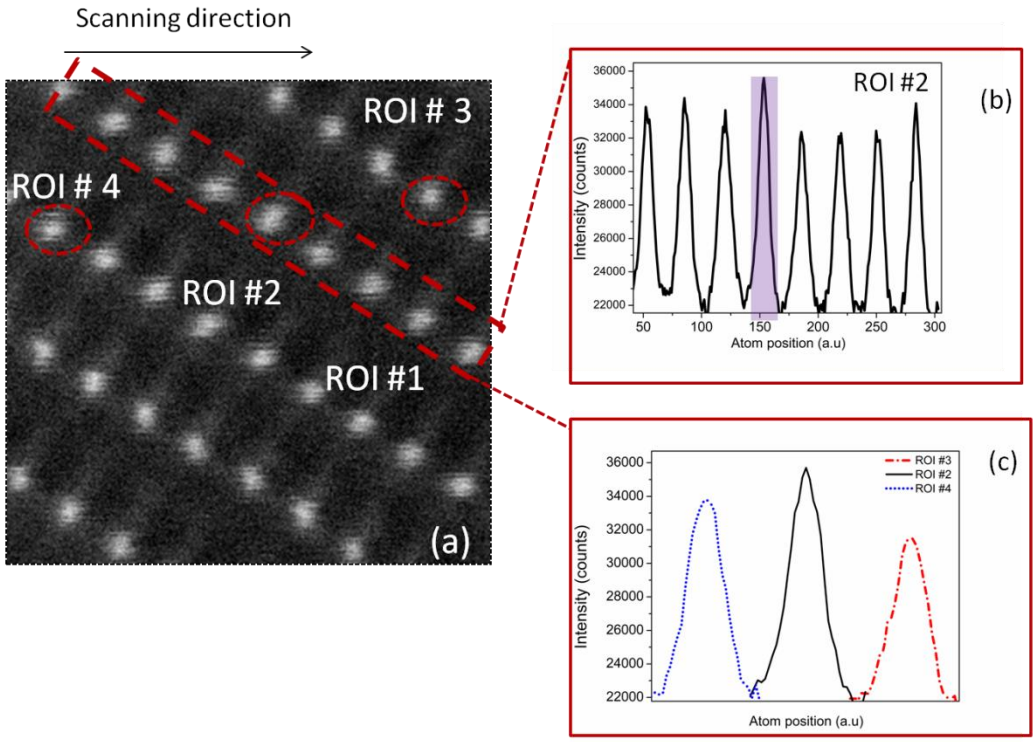

Figure 41 a) HAADF image of B-containing S_4A_7ED on <012> zone axis projection. (b) Intensity count profile of ROI#1, (c) ROI#2 which has the highest intensity among the atomic column compared with intensity count of atoms at ROI#3, and ROI#4.

3.4. Discussion

ABF Simulations on <001> showed that imaging the Sr ionic sub-lattice on this ZA should be considered, since neighboring Sr atoms are well-separated, as well as the different Sr^{2+} sites, Sr1 and Sr2. On the other hand, <010>-ZA simulations revealed that, although in projection, the two Sr sites are slightly offset, they are still distinguishable at the atomic level. On both zone axes, the Sr-sub-lattice is easily seen.

Simulations were carried out for (012)- and (013)-projections, in order to interpret the results obtained by HAADF and ABF imaging. The results showed similar, slightly offset Sr positions, when viewed along the <012> zone axis, where only Sr sub-lattice can be resolved by HAADF imaging. In <013> zone axis simulations, the Eu-doped simulations showed that, although Sr atoms are not particularly well-separated, even different Sr atomic sites are still resolvable, in addition to the Al sub-lattice. Since Eu atoms are heavier than Sr atoms, it is possible to detect a Eu dopant atom in the Sr atomic column by HAADF (*Z*-contrast) imaging as predicted by the simulations (see Figure 38 and 39).

Using diffraction mode in the TEM and HRTEM imaging, specimen were tilted onto a nearby low-index zone axis. Boron-free specimen were tilted onto a nearby ZA and corresponding diffraction pattern analysis showed that it is <013> zone axis (see Figure 26). Then we obtained atomically resolved STEM images by HAADF and ABF detectors in order to resolve the Sr and the Al and O sub-lattices. STEM HAADF and ABF images collected from both specimen were then analyzed in order to identify possible atomic positions that may be occupied by Eu. Since Eu ions are closer in size to Sr (in contrast to Al) and much too large for entering the structure interstitially, it must be replacing Sr atoms.[3, 29] HAADF images of the Sr sub-lattice from both <012> and <013> showed that different Sr atomic sites are well-resolved, consistent with simulated images. Along the <012> ZA, although different Sr sites are very close, practically overlapping in projection, they are still distinguishable, due to the elliptical shape that they form. HAADF images of <012> ZA showed that the Sr sub-lattice has variations in strong and weaker contrast differentiable by the naked eye. As expected, the HAADF or *Z*-contrast image is sensitive to the atomic number of the element. Therefore, differences in contrast should be analyzed

in order to detect a substitutional atomic species with a higher atomic number than the host lattice, such as Eu. Intensity profile analysis on Z-contrast image of B-containing sample showed that the average intensity of Sr atomic column which is assigned as region 1 (see Figure 40) was 32721±1362. Comparing the average intensity of column 1 and 2, showed that one atom on column 1 showed substantially higher intensity compared to other ones. The same is true when we compare the intensity profile of two atoms in the neighboring atomic columns, one in the scanning direction ROI #3 and one in the opposite direction labeled with ROI #4. The atom at ROI#2 showed 35700 counts, whereas ROI#3 and ROI#4 showed 32200 and 34000, respectively. Analysis revealed that atom #2 is actually shows higher intensity compared to two other neighboring atoms (see Figure 41).

On the other hand, Sr and Al sub-lattices were able to be resolved simultaneously on <013>, due to some characteristic symmetry features. The intensity profile along a line cut from the HAADF image obtained along <013> zone axis revealed that even different Sr sites located on slightly offset positions can be distinguished more clearly than along the <012>-zone axis (see Figure 37).

3.5. Conclusions

This study showed that HAADF is a very powerful technique for resolving the heavy atomic species; however, it is not possible to resolve both heavy and light atoms at the same time. ABF is also a very powerful technique where heavy and light atoms can be resolved simultaneously. Image contrast in ABF-STEM images is known to be very sensitive to thickness and defocus of the specimen[34], which we have seen in ABF image simulations. As observed in all simulations, the ABF image focus changes with thickness. Because of each Sr site (Sr1, Sr2) coordinates differently with O ions, each has a different Debye-Waller factors which defines their thermal vibrations with respect to its position. By considering the "TDS" factor, we succeeded in differentiating two different Sr sites in image simulations and concluded that both <012>, <013> ZAs are suitable to resolve Sr sub-lattice by *Z*-contrast imaging. Analysis of the experimentally obtained diffraction patterns revealed that we were able to tilt the specimen onto <012> and <013> ZAs. Along both zone axes, Sr and Al sub-lattices were successfully resolved at the atomic scale. However, it was observed that along the <013> zone axis, HAADF imaging yielded more information on both the Sr and Al sub-lattices simultaneously. We may conclude that, <013> zone axes are actually the most suitable zone axis for resolving the Al and Sr sub-lattice simultaneously for S_4A_7. We also show direct imaging evidence that the Eu dopant substitutes into the Sr sub-lattice. The results of this work illuminate the path toward elucidating the distribution of point defects in long persistence Eu, Dy, and B co-doped S_4A_7 phosphors.

CHAPTER 4:

THE ROLE OF BORON IN DETERMINING STRUCTURE AND LUMINESCENCE IN LONG PERSISTENCE EUROPIUM AND DYSPROSIUM CO-DOPED STRONTIUM ALUMINATE PHOSPHORS

4.1. Introduction

Long afterglow materials have demonstrated attractive potential for safety applications and energy efficient building materials, and their energy-storage potential has hardly yet been exploited. Among these, strontium aluminates (SAs) show high quantum efficiency when doped with Eu^{2+},[3, 29] and increased persistence duration when additionally doped with Dy^{3+}.[5] The SAs serve as stable hosts in 5 different primary phases: $SrAl_2O_4$ (SA), $Sr_2Al_4O_7$ (SA_2), $SrAl_{12}O_{19}$ (SA_6), $Sr_3Al_2O_6$ (S_3A) and $Sr_4Al_{14}O_{25}$ ($(SrO)_4•(Al_2O_3)_7$, S_4A_7)—although only SA and S_4A_7 are associated with the extended afterglow. Each phase consists of chains of charged AlO_x polyhedral forming a scaffold and defining cavities of negative charge,

into which Sr^{2+} ions are incorporated to provide electrical charge neutrality.[36] Eu^{2+} ions are the optically active centers, emitting visible luminescence upon relaxation from $4f^6 5d^1 \rightarrow 4f^7$ levels.[3] These ions enter the crystal structure by substituting into Sr^{2+} ion sites,[6, 37] and the consequent differences in crystal-field splitting result in distinguishable radiative relaxations.[3, 36] Because the orbitals of Eu^{2+} are highly sensitive to even subtle changes in the crystal field,[17, 38, 39] the features in the emission spectra can reveal different environments of Eu dopants in crystal lattices. For example, in the crystal structure of (S_4A_7), there are two, equally abundant, crystallographically non-equivalent Sr^{2+} sites—a higher symmetry site and a lower symmetry site. The co-dopant Dy^{3+} ions situated in close proximity to the Eu^{2+} offers trap levels near the $4f^6 5d^1$ level, allowing trapping of the excited electronic charges, which are easily susceptible to thermally stimulated release[1, 5, 36] This thermally stimulated de-trapping is associated with extending the afterglow duration of Eu-doped SA compounds. [5, 6, 40]

During ceramic processing by solid-state reaction, B_2O_3 is commonly added as a sintering flux agent. In the case of SA compounds, the dramatic extension of afterglow persistence was observed as a serendipitous side effect of the addition of B, from tens of minutes to longer than 14 hours.[10, 16, 41] To explain the effect of boron, many different theories have been proposed, but no consensus has been reached in the phosphor materials community due to lack of direct experimental evidence.[1] The most convincing computational model proposed suggests that the answer may lie in the aggregation of ionic defects: the substitutional rare earth dopants, oxygen vacancies, and B point defects.[6-9] Such a model necessitates the positioning of point defects of sufficient proximity for direct energy transfer between electronic trap levels.[2, 6, 30, 42, 43] The non-uniform distribution of ionic defects is thus presumed to enable persistent luminescence.

To elucidate the impact of boron on ionic defect distribution and electronic structure, we systematically investigated the correlation between B content, thermal properties, structural formation and stability, and optical properties in long persistence S_4A_7ED phosphor compounds. We used a modified sol-gel Pechini process,[18, 24] which allows better control over the phase purity. The averaged/global elemental stoichiometry, phase composition, and optical properties were analyzed to compare our data with that reported in the

literature. In addition, we correlated the phase composition, optical properties, and elemental stoichiometry at nanoscale resolution by using selected area electron diffraction (SADP) analysis, cathodoluminescence (nano-CL), and energy dispersive x-ray spectroscopy (EDXS)

of the compounds produced was analyzed in an inductively coupled plasma using optical emission spectroscopy (ICP-OES). To determine the crystal structure, we analyzed the powders by coupled θ-2θ x-ray diffraction (XRD) and electron diffraction in an aberration-corrected scanning transmission electron microscope (STEM). We determined the phase composition by Rietveld refinement analysis of the XRD results. Using an energy dispersive x-ray spectrometer (EDXS) attached to the STEM, we also analyzed the elemental distribution.

4.2. Experimental

$Sr_4Al_{14}O_{25}$ phosphor compounds were synthesized by a modified Pechini sol-gel method which we have described in Chapter 2. Global analysis on the structural properties have been performed by XRD and performed Rietveld analysis which have been previously shown in Chapter 2. Global optical properties such as PL emission and afterglow persistence have also been investigated and shown in Chapter 2 as well. Localized phase identification in the microstructure was investigated by electron diffraction in a TEM with a C_s-aberration-corrected probe (JEOL JEM-ARM 200CF) at 200 keV. Using an energy dispersive x-ray spectrometer (EDXS, Jeol Centurio) attached to the TEM, the elemental distribution with nanoscale spatial resolution in STEM mode (probe size *ca.*2Å, probe current *ca.* 700 pA, spectrum image collection time of 1458 s). Specimen for TEM analysis were prepared in two ways: 1) by focused ion beam milling of a lamella from a single particle and 2) by cold isostatic pressing of the powders into a pellet, which was then sintered at 1150°C in varigon (96% Ar/4% H_2) for 3 hours; the pellet was sliced, so that the middle of the pellet could be mechanically thinned, then ion milled to 200 keV electron transparency. Finally, we performed nanoscale spatially resolved cathodoluminescence (CL) in a dedicated scanning transmission electron microscope (STEM, Vacuum

Generators, VG HB501) at 60keV with *ca.* 50 nA of beam current using a liquid N_2-cooled specimen and a custom-built CL system.[44]

4.3. Results

A way to investigate the distribution of Eu in the microstructure is nano-CL in a dedicated STEM, which enables the mapping of cathodoluminescence by rastering with a nanoscale probe in a dedicated STEM, *i.e.* correlating nanoscale-localized microstructure with optical properties.[44] As Eu doped in SA compounds has characteristic radiative transitions in the visible spectrum, we analyzed spectrum images formed from the CL signals arising from these known $4f^6 5d^1 \rightarrow 4f^7$ transitions of Eu^{2+} and $4f$-$4f$ transitions of Eu^{3+}. Thus, the CL spectrum images enabled us to map not only the distribution of Eu atoms, but more specifically the distribution of Eu^{2+} and Eu^{3+} ions, and even more specifically to discriminate between Eu^{2+} ions substituting into the two different types of sites in the Sr^{2+} sub-lattice of $Sr_4Al_{14}O_{25}$ (as shown in Figure 42).[17, 27, 29]

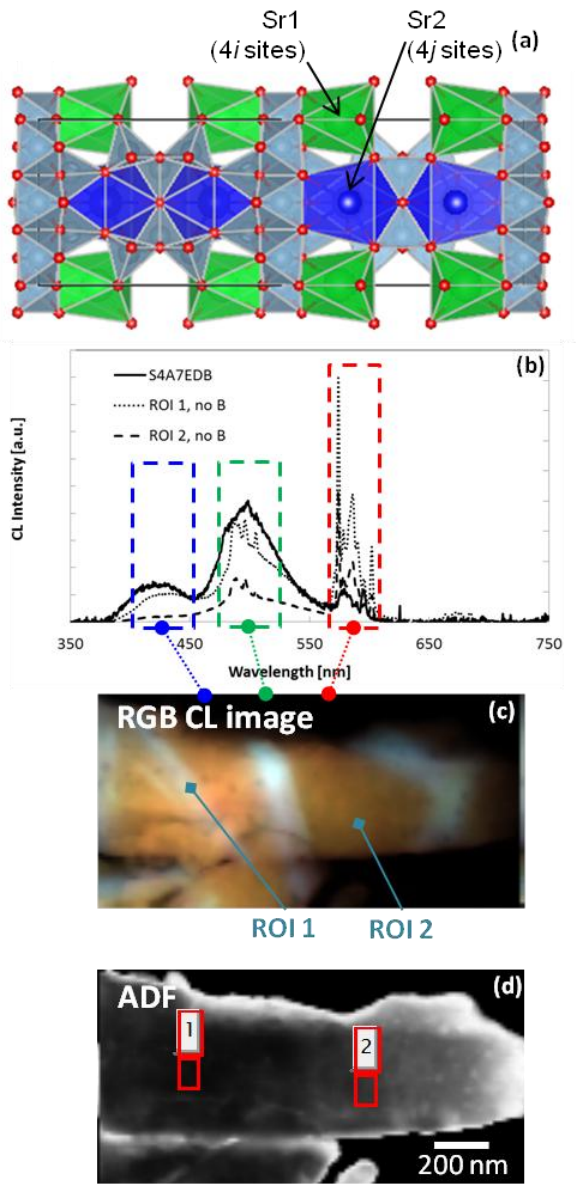

Figure 42 a) the crystal structure of $Sr_4Al_{14}O_{25}$: green = Sr^{2+} in 4i Wyckoff sites (Sr1), blue = Sr^{2+} in 4j Wyckoff sites (Sr2), gray = Al^{3+}, red = O^{2-}; (b) cathodoluminescence (CL) emission spectra from both boron-doped and boron-free S4A7ED specimen (from 2 different regions analyzed); at ca. 420 nm, emission from Eu^{2+} in the Sr2 sites (i.e., the Sr^{2+} sites in blue); at ca. 490 nm, emission: from Eu^{2+} in the Sr1 sites (i.e. the Sr^{2+} sites in green)[32]; Region 1 a plate-like grain; Region 2 equiaxed SA particles; (c) RGB image formed from CL emission from the spectral regions indicated: blue from 402-456 nm, green from 476-525 nm and red from 566-607 nm; (d) corresponding annular dark field image of the entire region analyzed by CL spectrum imaging.

The specimen containing 4.5 mol% B, a single crystal of S_4A_7, showed two broad emission bands in the CL spectrum at ca. 420 nm and 490 nm (Figure 42b, solid line). Both are consistent with $4f^6 5d^1 \rightarrow 4f^7$ radiative relaxation in Eu^{2+}, when exposed to two different crystal field potentials. This situation has been reported for Eu^{2+}, when occupying 2 crystallographically non-equivalent Sr^{2+} sites in S_4A_7. The radiative relaxation corresponding to emission at ca. 420 nm is associated with Eu^{2+} occupying an Sr2 site (i.e., the 4j Wyckoff sites), while the emission at ca. 490 nm originates from Eu^{2+} in an Sr1 site (i.e., the 4i Wyckoff sites).[11, 27, 29, 45] An additional emission band is also present at ca. 580 nm, and has been ascribed to the *4f→4f* transition of Eu^{3+},[30] although the *4f→4f* transitions of Dy^{3+} are also known to appear in that range.[46] It should be noted that the lamella was produced by FIB thinning from a single crystal particle of S_4A_7 phase (as determined from the indexed diffraction pattern in Figure 26), and that the CL spectrum is relatively uniform across the entire specimen of thickness ~113 nm.

In addition to the CL spectrum representative of the boron-doped compound, two characteristic spectra are also shown in Figure 42 from a boron-free specimen. One type of CL emission arises from the plate-like grains (the dotted line in Figure 42b), while the other is produced from the more equiaxed grains (the dashed line in Figure 42b). The CL emission from Eu^{2+} appeared to be largely confined to the crystals of platy habit, where emission from *ca.* 420 nm and 490 nm were strong. CL emission from these transitions was much weaker from the surrounding material. On the other hand emission from *ca*. 585 nm appeared more uniformly across the entire microstructure analyzed. Emission in this region is consistent with that of Eu^{3+} reported by Abbruscato in Eu-doped $SrAl_2O_4$ compound.[47] Although *4f→4f* transitions in Dy^{3+} may also appear in this spectral region, the fact that the measured spectrum bears strong resemblance to that of SA doped only with Eu suggests that the contribution of Dy^{3+} is negligible.[48, 49] Although seldom observed in room temperature PL studies of phosphor powders, due to the relatively lower probability of parity-forbidden *4f→4f* transitions in trivalent Eu and Dy, the nano-CL system has higher energy resolution and enables detection of these transitions, even in the presence of dominant emission from Eu^{2+}. With the nano-CL system, it was necessary to use a lower energy resolution, in order to collect sufficient signal from the FIB lamella of the B-doped specimen. Despite this, substantial emission ca. 585 nm was still detected (Figure 42b, solid

line). However, the relatively thicker B-free specimen luminesced more strongly, enabling use of the optics in a higher energy configuration. Hence the spectra obtain in the nano-CL system may reveal substantially more information, due to the capability for resolving the sharp, weaker emission in the red spectrum. Because CL analysis of minerals containing trivalent Eu or Dy have revealed the strongest characteristic transitions in the range 573-586 nm, detailed spectral decomposition studies will help resolve any contribution from trivalent Dy.[46]

By assigning the emission from 420 nm to the blue channel, 500 nm to green, and 585 nm to red, a red-green-blue (RGB) image demonstrates the relative distribution of CL emission sources in the microstructure (see Figure 42c and Figure 43). Regions, which appear white in the RGB image, reflect a mix of signals from the red channel, the green channel, and the blue channel with equal contribution. By contrast, the orange regions reflect a mixture of signals from the red channel predominantly with more limited contribution from the green one and none from the blue channel. Note that the polycrystalline nature of the specimen can be distinguished from the contrast in the annular dark field (ADF) image in Figure 42d. Direct comparison between the ADF and the RGB images reveals that differences in the microstructure arising primarily from a non-uniform distribution of optically active emitters between grains.

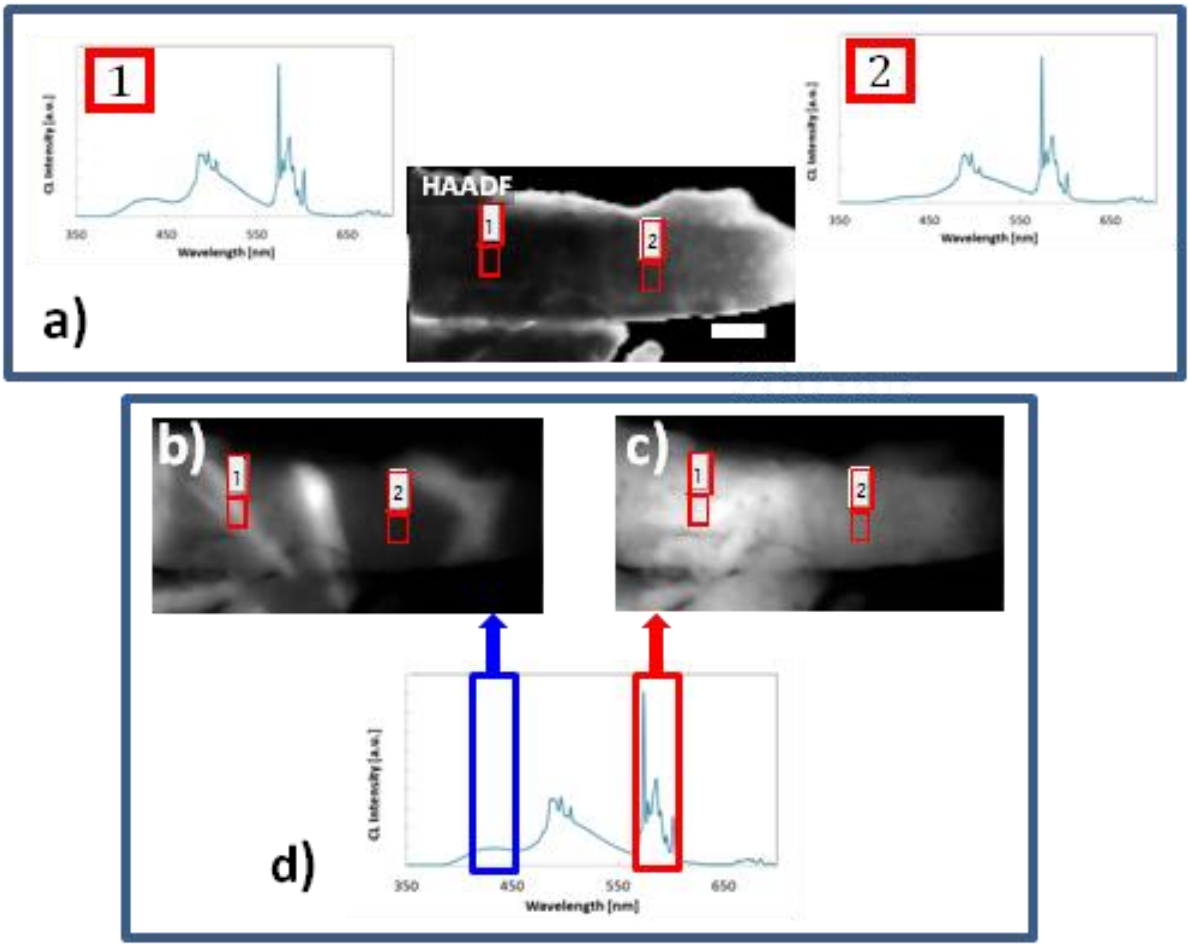

Figure 43 Cathodoluminescence (CL) spectra and spectrum images from the boron-free specimen. (a) CL emission spectra from 2 different regions analyzed: Region 1 from a crystal undergoing abnormal grain growth, Region 2 from more equiaxed SA particles; (b) spectrum image from CL emission in 402-456 nm showing differentiation between AGG particles and the surrounding microstructure; (c) spectrum image from CL emission in 566-607 nm showing uniform distribution of emission across the microstructure; (d) the CL spectrum from the entire region in the HAADF image in part *a*.

In order to evaluate the stoichiometry of different regions of the microstructure shown in Figure 28c, we performed EDXS analysis. The results summarized in Figure 44 (full spectrum shown in Figure A 1) were obtained from quantifying spectra extracted from a spectrum image. The plate-like grain contained an Al:Sr at% ratio of 8, labeled as ROI #1, and an enrichment in Eu. The surrounding equiaxed grains, represented by the spectrum from ROI #2, had an Al:Sr at% ratio of 2.3, and the Eu content was generally below the sensitivity limit of EDXS. Further analysis of microstructure from other regions of a B-free

specimen far away from the plate-like grain revealed an Al:Sr ratio *ca.* 2.3 and with a Eu content ranging 0.19-0.38 at% and a Dy content ranging 0-0.23 at%.

In the 4.5 mol% B-doped specimen, EDXS analysis revealed a uniform Al:Sr at% ratio of *ca*. 2.3 and a uniform Eu and Dy content of 0.64 at% and 0.21 at% respectively, consistent with the results of nano-CL.

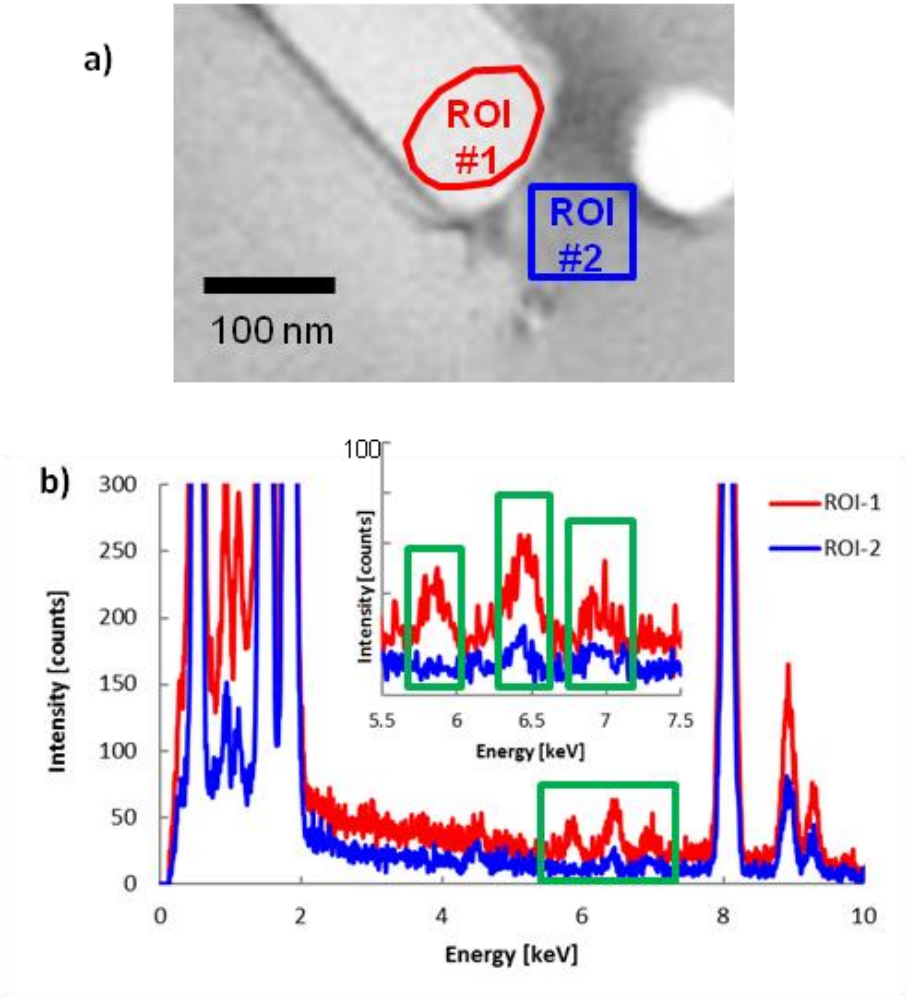

Figure 44 (a) bright-field TEM image of a boron-free S_4A_7ED specimen (zoomed in view, from Figure 28), with the two regions analyzed by EDXS indicated and b) the corresponding EDXS spectra; ROI #1 of the plate-like grain, ROI #2 of the neighboring equiaxed grain; Al-Ka at 1.49 keV and Sr-L at 1.58 keV were used for quantifying the Al:Sr ratio. Inset: Peaks for Eu-Lα at 5.85 keV, Eu-Lβ at 6.46 keV, Dy-Lα at 6.49 keV and Eu-Lβ2 at 6.84 keV revealed that Eu and Dy were predominantly concentrated in the plate-like grain. Both Eu and Dy were below the sensitivity limit in ROI #2.

4.4. Discussion

In order to assess the effect of boron on dramatically extending the afterglow in $Sr_4Al_{14}O_{25}$:Eu^{2+},Dy^{3+}, we considered its impact on the microstructure, the composition, and the luminescence properties. Combining the results of thermal analysis, XRD, and imaging and diffraction analysis in the electron microscope, we confirm that boron facilitates the microstructural evolution of the equilibrium S_4A_7 crystalline grains in ceramic powders prepared from a nominal $Sr_4Al_{14}O_{25}$ stoichiometry.

Images of the microstructure formed from signals collected by an annular dark field (ADF) detector in a dedicated STEM revealed substantial differences in microstructure, particularly comparing that between boron-free and the 4.5 mol% boron-doped compounds. The boron-free powders contained some plate-like, anisotropic grains of unusually high aspect ratio, in addition to neighboring equiaxed crystals of *ca*. 10 μm in diameter. In contrast, the 4.5 mol% boron-doped powders contained many large (*ca.* 20 μm-diameter), equiaxed crystal grains of S_4A_7 phase. These results are consistent with the long-standing use of boron as a sintering flux in ceramic powder processing[50] and with the reports that boron is necessary to stabilize the formation of the S_4A_7 phase.[11, 17] In fact, our results suggest that many of the phases present in the equilibrium SrO-Al_2O_3 binary system are metastable and are able to form due to favorable local kinetics I n the dried amorphous gel. However, the presence of boron, by lowering viscosity in the amorphous precursor, appeared to have substantially lowered the barrier for formation of the equilibrium phase S_4A_7, enabling a strong preference for that phase structure to form in the evolving microstructure, at the expense of the other SA phases: SA_6, SA, SA_2, *etc*.

Comparing the compositional variations between boron-free and 4.5 mol% boron-doped S_4A_7 compounds revealed additional insight into the substantial impact of boron. Using STEM-EDX, we observed two types of compositional variations. If the region analyzed was contained in a plate-like grain, the composition was Al-rich (Al:Sr cation ratio of 8) and contained a much higher Eu content, with an inconclusive Dy content, while the surrounding equiaxed grains did not contain enough Eu to be above the detectability limit.

In the absence of these anisotropic grains, the Al:Sr cation ratio was more uniform, ranging from 1.5-3.1, and a corresponding Eu content spanning 0.38-0.19 at%. In the B-doped S_4A_7 specimen, the TEM lamella was a single crystal with a uniform distribution of Eu. Although the Al:Sr cation ratio should theoretically be 3.5 (from 14 Al cations per 4 Sr cations per mole of $Sr_4Al_{14}O_{25}$), a cation ratio value of 2.3 was determined from EDX measurements on regions, whose SADP's had indexed to $Sr_4Al_{14}O_{25}$. Thus we consider 2.3 to be the reference value for S_4A_7.

In the boron-free compounds, Eu^{3+} was present throughout microstructure, due to incomplete reduction,[6, 41] while Eu^{2+} appeared primarily in the Sr1 sites (in the 4*i* Wyckoff sites). Only in the plate-like grains, would emission arise from the Eu^{2+} in Sr2 sites (in the 4*j* Wyckoff sites). In contrast, in the B-doped large single crystal, Eu^{2+} is uniformly present in both types of Sr sites, in addition to a homogeneous signal from Eu^{3+}. It should be noted that when using PL, the Eu^{3+} was not detectable, possibly because its emission was below the detector sensitivity limit. These results are summarized in Table 10.

Table 10 Summary of CL spectrum characteristics and the corresponding origin of transitions.

Region analyzed	Eu^{2+} in 4*j* sites (*ca.* 420 nm)	Eu^{2+} in 4*i* sites (*ca.* 490 nm)	Eu^{3+} (*ca.* 580 nm)
B-free, platy	Strong	Strong	Present
B-free, equiaxed	Weak	Weak	Present
4.5 mol% B-doped	Strong	strong	Present

Combining this evidence on the B effect on microstructure, composition, and luminescence in Eu and Dy co-doped S_4A_7 compounds, we report an association between long afterglow persistence and a uniform distribution of Eu^{2+} in Sr2 sites. When B is present, S_4A_7 is the equilibrium phase and dominates the microstructure; the composition and distribution of optically active ions are uniform; and the afterglow persists for longer than 14 hours. However, without B doping, in an SA compound of the same nominal S_4A_7 stoichiometry,

there is a broader range of inhomogeneous cation stoichiometry in the microstructure, as well as persistence abbreviated to *ca.* 10 minutes. The localized stoichiometric variation gives rise to the formation of crystalline grains of a variety of SA phase. In the Eu- and Al-rich anisotropic grains, CL suggests that the distribution of Eu^{3+} is homogenous, but Eu^{2+} is localized to the anisotropic grain and absent from the neighboring equiaxed grains. One final comment is that even though there is a high content of Eu^{2+} in Sr2 sites in B-free, Al-rich, anisotropic grains, the short afterglow may possibly be evidence of concentration quenching.[41]

Previous investigations correlating luminescence behavior with Al:Sr ratio (in B-free samples) were performed on pressed powder pellets 10 mm in diameter and 5 mm in thickness.[51] Emission was evaluated from many particles, and it was assumed that 2 phases, SA and SA_6, were the only ones present. However, electron diffraction and spatially resolved elemental spectroscopy from individual grains now reveal at the local scale a much more complicated microstructure and elemental distribution in B-free SA phosphor powders. With a broader range of cation stoichiometry, the consequent increased diversity in crystal field environments of Eu^{2+} results in a richer range of transitions arising from variation of energy level separation, accounting for the broad bandwidth at *ca.* 420 and 500 nm.

Our results are also consistent with the observations reported by Chen and co-workers—the addition of boron enhanced both the initial afterglow intensity and the persistence intensity over time in Eu and Dy co-doped SA.[41] After all, higher emission intensity would be associated with increased Eu^{2+} concentration in the crystal structure. Without boron, less Eu^{2+} would be incorporated into the SA crystal structure, whereas with B, the uptake of Eu^{2+} into the SA structure is higher and more uniformly distributed at the nano-scale than in the boron-free compounds.

4.5. Conclusions

By combining insights obtained from thermal analysis, XRD, PL/PLE, EDS and nano-CL in a STEM, we report evidence suggesting that boron improves the homogeneous distribution of optically active Eu^{2+} into 4*j* Wyckoff site in the Sr^{2+} sub-lattice, which is necessary for persistence longer than 14 hours in B, Eu^{2+} and Dy^{3+} co-doped $Sr_4Al_{14}O_{25}$ phosphors. The presence of B facilitates the evolution of a microstructural morphology consisting of large, equiaxed single-phase grains, with a uniform distribution of Eu^{3+} and Eu^{2+} ions. However, the absence of B allows the formation of multiple phases of SrO-Al_2O_3, including high aspect ratio, Al-rich and Eu-rich grains, surrounded by regions depleted in Eu content. Although Eu occurs in Eu^{3+} uniformly throughout this microstructure, the distribution of optically active Eu^{2+} depends on the local Sr site coordination, of which there are two in the S_4A_7 phase. Eu^{2+} occupying the higher symmetry 4*i* Wyckoff site of Sr were distributed uniformly. However, Eu^{2+} appeared in the lower symmetry 4*j* Wyckoff site of Sr only in the platelike grains. Thus we conclude that a necessary condition for extended afterglow in S_4A_7ED is the homogeneous incorporation of Eu^{2+} into the microstructure.

CHAPTER 5:

LOCAL AREA ELECTRONIC STRUCTURE INVESTIGATIONS BY ELECTRON ENERGY-LOSS SPECTROSCOPY

5.1. Introduction

In order to elucidate the effect of boron on the crystal structure and electronic structure of SA phosphors, the position of boron incorporated into the S_4A_7 could be elucidated by fingerprinting with electron energy loss near edge spectra (ELNES). The shape of the B-K edge reflects the local bonding environment of boron in a crystal. For example, one sharp π^* peak positioned at 194 eV and a wider σ^* peak at 203 eV were the characteristic features indicating that the compound of interest contains three-fold coordinated boron, whose bonding electrons are in $2p$ and sp^2-hybridized orbitals.[52] When boron is coordinated by 4 oxygens, the bonding electrons are in sp^3 hybridized orbitals only, and only σ^* transitions occur when excited by the probe electrons. Previous studies of B in minerals have reported the B-K edge ELNES for B in trigonal and tetragonal coordination by oxygen,[52] and the use of such fingerprints to determine the type of coordination in B-containing minerals.[53]

The core-loss region of electron energy loss spectra contains a wealth of information on the bonding environment of ions.[54]The energy loss of an incident electron stems from an

electronic transition induced by inelastic interaction with an electron in the sample, often the ones involved in bonding with neighboring lattice atoms. For an ion coordinated by 6 oxygen anions in an octahedral configuration, the amount of energy loss should reflect an underlying symmetry in the distribution of effective charge, such as for an incident (probe) electron interacting with electrons in each of the six bonds. Accordingly, a defect in such a system, such as an oxygen vacancy, a change in interstitial site occupancy, or a change in next nearest neighbor site occupancy, could be reflected by a change in the shape of an electron energy loss near-edge spectrum (ELNES) region.[55-58] Therefore, examination of the ELNES may elucidate how boron is incorporated into the S_4A_7 crystal structure. XRD has shown that synthesis of a stoichiometric S_4A_7 compound doped with 1 mol% Eu, 1 mol% Dy, and 30 mol% B_2O_3 retains the crystal structure of S_4A_7.[58] Given the fact that B is a much smaller cation compared to Al and Sr, B could be incorporated into interstitial sites, or substitutionally into the Al sub-lattice, or a mixture of both. If B is incorporated by substituting into an Al site, then B would be replacing a 4-, 5-, or 6-fold coordinated Al. In the case of B incorporation into interstitial sites, a mixture of 4-fold and 3-fold coordination may be possible, as reported for the case of B incorporation in to the sodium alumino silicate structure of synthetic tourmaline.[53] The ELNES of the B K-edge for B in 3-fold and 4-fold coordination was reported by Garvie [52] as shown in Figure 45 for a variety of compounds containing BO_3 and BO_4. In the same report, the B-K ELNES was also presented for a compound containing B in both 4-fold and 3-fold coordination. The application of these fingerprints were used by Schreyer *et al* to identify the coordination polyhedra units of B in two B-containing minerals.[53]

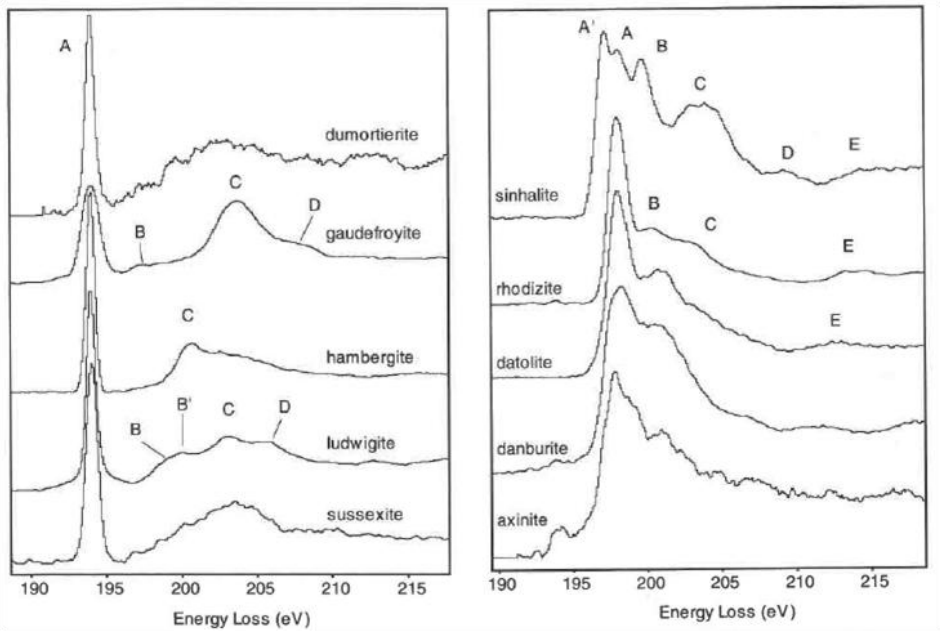

Figure 45 ELNES B-K edge of various minerals with three-fold and four-fold coordinated boron.[52]

The objective of this study is to apply the fingerprinting method to determine the coordination of B in boron-doped S_4A_7ED. For fingerprinting, 2 reference minerals were used. Ludwigite contains B in pure 3-fold coordination, while rhodizite has B in only 4-fold coordination.[52]

Determination of the fraction of boron coordination could be obtained by using a method previously described by Sauer et.al.[59] According to this study, either for a three-fold or a four-fold coordinated boron, there is a ratio between the integrated intensity of the π^* peak, $I(\pi^*)$, and the integrated intensity of a large energy window above the edge onset, $I(\Delta E)$. By comparing this fraction to a compound that has both three-fold and four-fold coordinated boron, it is possible to determine the relative fraction of each present inside the compound, according to Equation 3:

$$F = \frac{\left[I(\pi^*)/I(\Delta E)\right]}{\left[I(\pi^*)/I(\Delta E)\right]_{ref}} \qquad \text{Equation 3}$$

5.2. Experimental

To investigate the changes in electronic structure upon boron incorporation into SA-type phosphors, we synthesized the phosphor powders with a modified Pechini sol-gel sytnesis method as described in Chapter 2. We performed XRD investigations in order to determine the phase of the final compound, which considered in detail in Chapter 2. We then performed electron energy-loss spectroscopy analysis in order to determine the local bonding environment of B in S_4A_7EDB, by using a scanning transmission electron microscope (JEOL JEM-2010 F). EELS spectra were acquired using a probe convergence angle of 22 mrad and a collection semi-angle of 17.5 mrad with 200 keV beam energy. We analyzed the B-K edge ELNES in boron-containing S_4A_7ED and in the reference minerals, ludwigite, and rhodizite. The ELNES B-K edge was simulated for weighted mixtures of 3-fold and 4-fold B-coordinated alloys and then compared with the B-K edge of S_4A_7EDB compounds.

5.3. Results

B-K edge ELNES from reference minerals ludwigite and rhodizite are shown in Figure 46.

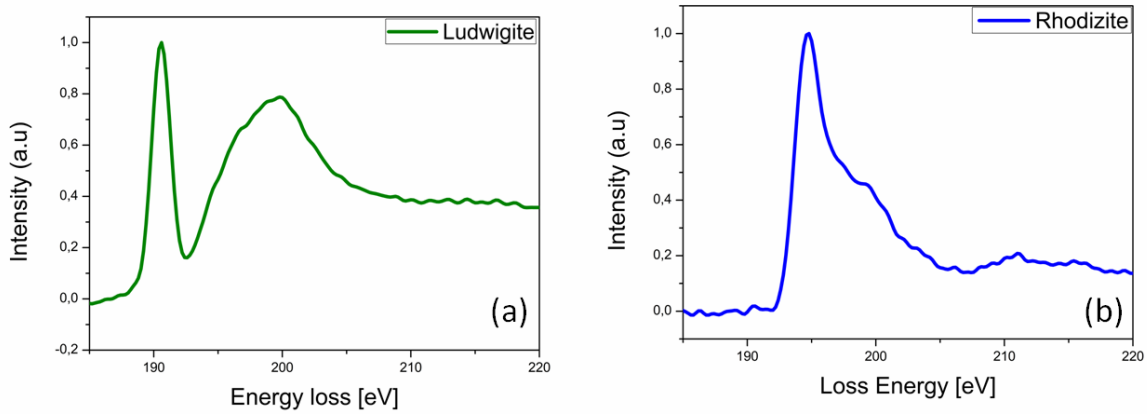

Figure 46 ELNES B-K edge of (a) ludwigite mineral having 3-fold coordinated boron and (b) rhodizite mineral having 4-fold coordinated boron.

Using these B-K edges as references, we simulated the B-K edge ELNES for weighted mixtures of 3-fold and 4-fold B-coordinated alloys. The simulated ELNES are shown in Figure 47.

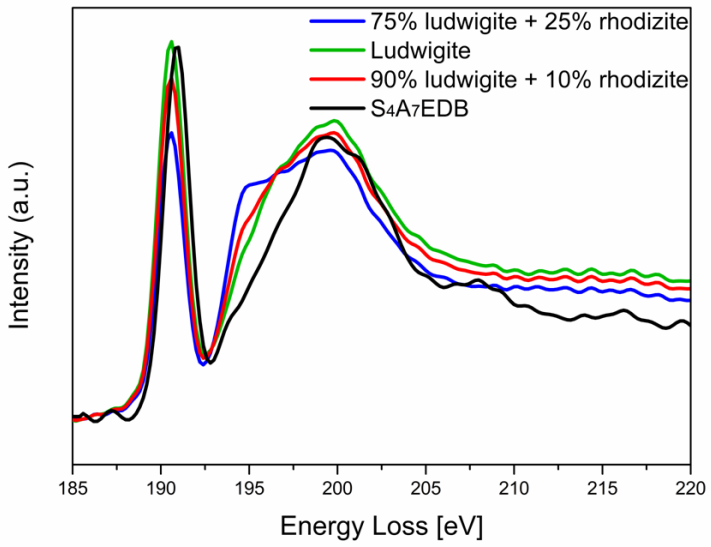

Figure 47 Comparison between the ELNES B-K edges of only ludwigite, alloy of 75% ludwigite and 25% rhodizite, 90% ludwigite and 10% rhodizite, and ELNES B-K edge of S_4A_7EDB compound.

Out of 20 measurements, not all of them gave the B-K edge ELNES structure or only very weak signals were detected. This lack of compositional homogeneity can be attributed to a non-uniform or inhomogeneous distribution of boron content in the crystal structure.

For seven different B-K ELNES measurements for ludwigite were calculated and summarized in Table 11.

Table 11 Ratio of integrated intensity of π^* peak to the the integrated intensity energy window above the edge onset $I(\Delta E)$ for ludwigite.

Sample number	$I(\pi^*)/I(\Delta E)$
1	0.22
2	0.18
3	0.19
4	0.21
5	0.23
6	0.24
7	0.19
average	**0.21**

The average $I(\pi^*)/I(\Delta E)$ ratio for ludwigite, which contains only trigonal coordinated boron, was determined to be 0.21, which will serve as the reference ($I(\pi^*)/I(\Delta E)_{ref}$) fraction for pure trigonal B. This analysis was then applied to the EELS of S_4A_7EDB, and an average value was obtained for the $I(\pi^*)/I(\Delta E)$. The values summarized in Table 12 were calculated against the average value from the ludwigite sample. . The total fraction indicates the amount of three-fold boron inside the S_4A_7EDB compound.

Table 12 Fraction of 3-fold coordinated boron in S_4A_7EDB compound.

Sample no	$I(\pi^*)$	$I(\Delta E)$	$I(\pi^*)/I(\Delta E)$	**Fraction**
1	274	1244	0.22	1.04
2	86	476	0.18	0.87
3	138	753	0.19	0.91
4	171	819	0.21	1.00
5	250	1079	0.23	1.09

5.4. Discussion

Investigations into the coordination of boron in the crystal structure were conducted by electron energy-loss spectrometry for SA_2ED compounds with varying boron content. B-K ELNES of these compounds were compared with two reference standards that contain only three-fold coordinated boron (ludwigite) and only four-fold coordinated boron (rhodizite). Comparison of the shape of the B-K ELNES of S_4A_7EDB with the three-folded boron containing mineral ludwigite clearly indicates the presence of BO_3 units in the corresponding compounds, the lack of resemblance with the B-K ELNES of rhodizite confirms the lack of tetrahedral-coordinated B. Thus the resulting B-K edge data shows that boron enters the structure only as three-fold coordinated in every SA compound. We quantified the ELNES B-K edge data of every SA compound by implementing the method used by Sauer *et.al*.[59] to quantify the total number of transitions characteristic of trigonal and tetrahedral coordination states of boron. The results of this quantification suggested that three-fold coordinated boron is present in S_4A_7EDB compounds.

5.5. Conclusions

In this part of the study we show that boron enters the structure of longer persistence Eu, Dy, and B co-doped S_4A_7 in 3-fold coordination, by comparing the B-K ELNES using two reference minerals, one containing only three-fold coordinated boron (ludwigite) and only four-fold coordinated boron units (rhodizite). This comparison was performed both qualitatively by inspecting the fingerprint B-K ELNES of the EEL spectra and quantitatively by summing the contributions to the signal in the ELNES arising from π^* and the σ^* transitions of B.

CHAPTER 6:

SUMMARY AND FUTURE WORK

The objective of this dissertation is to apply nanoscale and atomic scale-resolved imaging and spectroscopy techniques to elucidate the role of B in extending persistence in Eu, Dy, and B co-doped $Sr_4Al_{14}O_{25}$. Our study has revealed many insights into the equilibrium phase evolution and ionic point defect presence and distribution related to the dramatic extension of afterglow.

In Chapter 2, a structural investigation was performed globally, to compare our phosphor properties to those in the literature, and to elucidate the microstructural evolution. Analyses by TG-DTA and XRD revealed that the presence of B facilitates the formation of S_4A_7 phase, while lowering the kinetic barrier for the high-temperature equilibrium phase formation. We observed that the presence of B is necessary for long afterglow persistence, although its presence alone does not ensure afterglow. Elemental analysis investigations by ICP-OES showed that boron actually enters the structure, although it differs from the

nominal value significantly. However, enhanced persistence could still be observed as boron entered the structure.

In Chapter 3, we used advanced TEM techniques to evaluate the microstructure with atomic-sale resolution. Selected area electron diffraction patterns revealed the dominant presence of equiaxed S4A7 grains, which is one of the two long persistence phases in the strontium aluminates phosphor family. Experimentally obtained HAADF and ABF images on <012> and <013> zone axes were interpreted by using simulations of the images. The STEM images obtained by HAADF and ABF imaging technique showed that Sr and Al sub-lattices could be resolved on <013> zone axis simultaneously, and STEM image simulations were consistent with the experimental results. Simulations obtained by Eu-doped S_4A_7 structure showed that Eu dopant could be easily observed such that Eu dopants would appear at Sr sub-lattice as brighter atoms. Experimental HAADF image of boron-containing specimen showed signs of Eu dopant atom, as we have observed atoms having brighter intensity than the rest of the Sr column.

In Chapter 4, the results of diffraction analysis, nanoscale cathodoluminescence, and energy-dispersive x-ray spectroscopy in a STEM combined established that the uniform distribution of Eu^{2+} in the Sr sub-lattice is another necessary condition for extended persistence. We confirm that boron facilitates the dominance of equilibrium S_4A_7 grains in the microstructure, exceeding 97%, and uniform stoichiometry throughout the grain. Without boron doping, it is clear that multiple phases form, and the Al-rich one with plate-like grains acts as a sponge, collecting rare-earth dopants from neighboring grains. While EDXS revealed the distribution of elements, nano-CL was shown to be a pivotal tool in differentiating the spatial distribution of divalent versus trivalent Eu. Moreover, we were able to distinguish between Eu^{2+} ions occupying the 2 crystallographically non-equivalent Sr sites. We observed a strong luminescence in the B-free compounds from Eu^{2+} in the lower symmetry site only in the plate-like grains, against a background of uniformly distributed Eu^{3+}. By sharp contrast, the long persistence compounds containing boron had large single-phase S_4A_7 grains with a uniform presence of Eu^{2+} throughout the Sr sub-lattice, and distributed in both types of Sr sites. Clearly an

important condition for long afterglow is the uniform distribution of Eu^{2+} throughout the microstructure of equiaxed S_4A_7ED grains, and boron play 2 key roles: 1) facilitating a more uniform distribution of Eu^{2+} and Eu^{3+} and 2) promoting the formation of single phase S_4A_7.

In Chapter 5, we have analyzed the coordination of boron in S_4A_7EDB compounds by fingerprint comparison with the B-K ELNES in 2 boron-containing minerals, ludwigite and rhodizite. The resemblance solely with ludwigite, which contains boron only in three-fold coordination proves that boron enters the S_4A_7EDB structure only in three-fold coordination.

Our results mandate substantial revision to the existing point defect clustering model of extended persistence in Eu, Dy, and B co-doped strontium aluminate phosphors. We have determined the conditions for interrogating these compounds at the nanoscale and atomic scale, by using advanced TEM techniques, such as HAADF-STEM imaging, ABF-STEM imaging, EELS, and STEM-EDXS. With nano-CL, we can further distinguish between divalent and trivalent Eu, and the site occupation of Eu^{2+}. The obvious next steps include deeper investigation of the bonding environment of boron by electron energy loss spectroscopy (EELS), correlated to AR-STEM; moreover by using ABF-STEM imaging techniques, we can look for spatial correlation between the positions of B with the Eu and Dy ions, to further validate the point defect clustering mechanism.

APPENDIX

Table A1 ICP-OES elemental analysis result of samples collected after TG-DTA analysis. Weight percentage of Eu and Dy and corresponding SD (absolute standard deviation) values.

Sample No	Boron Content (mol% B2O3)	Heating rate/ Atmosphere	Eu mg/kg	SD (mg/kg)	Dy mg/kg	SD (mg/kg)
1	B-free	10°C min^{-1}/N2	1266.437	8.58	1289.915	18.29
2	B-free	10°C min^{-1}/air	1142.879	6.21	1220.768	7.43
3	B-free	5°C min^{-1}/N_2	1228.351	9.63	1243.082	9.53
4	B-free	5°C min^{-1}/air	1144.484	9.76	1211.498	12.71
5	B-free	1°C min^{-1}/ N_2	1265.261	6.89	1278.841	9.19
6	B-free	1°C min^{-1}/air	1277.136	15.05	1319.868	263.71
7	10	10°C min^{-1}/N2	1387.713	9.98	1458.784	5.69
8	10	10°C min^{-1}/air	1475.294	11.43	1580.231	18.54
9	10	5°C min^{-1}/ N_2	1402.974	140.52	1487.726	20.59
10	10	5°C min^{-1}/air	1444.622	2.23	1562.991	4.40
11	10	1°C min^{-1}/ N_2	1416.667	18.10	1515.031	18.91
12	10	1°C min^{-1}/air	1448.719	19.14	1563.352	20.58
13	20	10°C min^{-1}/ N_2	1572.245	18.11	1554.481	22.95
14	20	10°C min^{-1}/air	1434.535	9.56	1499.573	9.30
15	20	5°C min^{-1}/ N_2	1578.501	26.29	1562.998	28.47
16	20	5°C min^{-1}/air	1476.675	5.27	1513.871	3.92
17	20	1°C min^{-1}/ N_2	1516.122	7.91	1567.646	11.63
18	20	1°C min^{-1}/air	1496.885	17.01	1541.281	14.51
19	30	10°C min^{-1}/ N_2	1784.985	10.83	1806.228	16.42
20	30	10°C min^{-1}/air	1657.416	9.88	1874.243	11.38
21	30	5°C min^{-1}/ N_2	2234.487	15.72	2566.686	45.40
22	30	5°C min^{-1}/air	1209.447	15.09	1241.529	15.34
23	30	1°C min^{-1}/ N_2	1661.504	17.08	1867.216	19.08
24	30	1°C min^{-1}/air	1675.518	17.33	1905.245	16.46

Table A2 ICP-OES elemental analysis result of samples collected after TG-DTA analysis. Weight percentage of B and corresponding SD (absolute standard deviation) values.

Sample No	Boron Content (mol% B2O3)	Heating rate/Atmosphere	Boron mg/kg	SD (mg/kg)
1	B-free	10°C min^{-1}/N_2	0	0.00
2	B-free	10°C min^{-1}/air	0	0.00
3	B-free	5°C min^{-1}/N_2	0	0.00
4	B-free	5°C min^{-1}/air	0	0.00
5	B-free	1°C min^{-1}/N_2	0	0.00
6	B-free	1°C min^{-1}/air	0	0.00
7	10	10°C min^{-1}/N_2	747.3805	11.74
8	10	10°C min^{-1}/air	856.0063	28.65
9	10	5°C min^{-1}/N_2	844.7882	22.14
10	10	5°C min-1/air	974.9459	18.31
11	10	1°C min^{-1}/N_2	797.8333	56.39
12	10	1°C min^{-1}/air	1024.274	69.04
13	20	10°C min^{-1}/N_2	3377.263	54.82
14	20	10°C min^{-1}/air	3163.444	33.78
15	20	5°C min^{-1}/N_2	3072.787	151.11
16	20	5°C min-1/air	2822.903	112.33
17	20	1°C min^{-1}/N_2	3100.354	55.45
18	20	1°C min^{-1}/air	3152.49	59.58
19	30	10°C min^{-1}/N_2	5834.305	49.13
20	30	10°C min^{-1}/air	6422.981	43.86
21	30	5°C min^{-1}/N_2	9364.472	58.78
22	30	5°C min^{-1}/air	4129.879	71.92
23	30	1°C min^{-1}/N_2	6345.343	89.82
24	30	1°C min^{-1}/air	6457.18	87.19

Table A3 ICP-OES elemental analysis result of samples collected after TG-DTA analysis. Weight percentage of Al and Sr, and corresponding SD (absolute standard deviation) values.

Sample No	Boron Content (mol% B_2O_3)	Heating rate/ Atmosphere	Al mg/kg	Al SD (mg/kg)	Sr mg/kg	Sr SD (mg/kg)
1	B-free	10°C min^{-1}/N2	272547.62	803.30	294155.61	594.26
2	B-free	10°C min^{-1}/air	257183.84	3001.98	279695.96	294.93
3	B-free	5°C min^{-1}/N_2	264405.91	2420.04	280893.37	1748.55
4	B-free	5°C min^{-1}/air	254961.09	6665.12	277144.94	1494.43
5	B-free	1°C min^{-1}/ N_2	270869.34	1469.25	279711.67	463.81
6	B-free	1°C min^{-1}/air	280247.64	4815.09	286527.41	1593.39
7	10	10°C min^{-1}/N2	285485.45	1830.75	275401.25	835.85
8	10	10°C min^{-1}/air	306699.16	3968.73	294228.51	1008.05
9	10	5°C min^{-1}/ N_2	292229.28	2046.04	280948.43	1369.06
10	10	5°C min^{-1}/air	304759.46	1652.13	294341.44	132.14
11	10	1°C min^{-1}/ N_2	295935.42	237.74	281953.13	2222.44
12	10	1°C min^{-1}/air	306596.25	5601.96	293163.95	1766.23
13	20	10°C min^{-1}/ N_2	290130.59	2562.25	287404.29	2079.37
14	20	10°C min^{-1}/air	276262.81	2541.14	275201.14	1701.14
15	20	5°C min^{-1}/ N_2	284970.73	4854.51	292181.50	2755.06
16	20	5°C min^{-1}/air	274198.51	4225.88	278178.66	493.05
17	20	1°C min^{-1}/ N_2	286740.24	4576.34	292623.17	1131.09
18	20	1°C min^{-1}/air	285108.61	5633.01	284210.04	1311.37
19	30	10°C min^{-1}/ N_2	245312.13	4521.33	270995.56	926.48
20	30	10°C min^{-1}/air	268325.72	1360.58	285531.25	763.22
21	30	5°C min^{-1}/ N_2	374029.33	2975.40	398414.96	888.20
22	30	5°C min^{-1}/air	172474.85	2429.52	187529.18	1601.56
23	30	1°C min^{-1}/ N_2	260343.01	2955.54	278141.16	8184.43
24	30	1°C min^{-1}/air	255825.61	2643.39	277647.14	1078.32

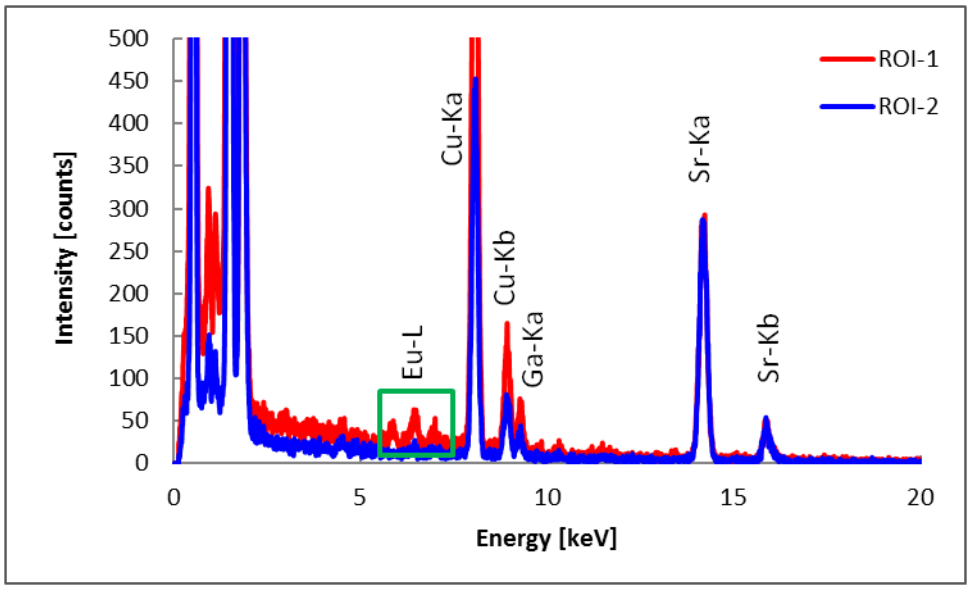

Figure A 1 Full-scale EDX spectrum for the analyzed regions shown in Figure 44.

REFERENCES

1 T. Matsuzawa, Y. Aoki, N. Takeuchi and Y. Murayama, *Journal of the Electrochemical Society*, 1996, **143**, 2670.

2 E. Nakazawa and T. Mochida, *Journal of Luminescence*, 1997, **72–74**, 236.

3 F. C. Palilla, A. K. Levine and M. R. Tomkus, *Journal of the Electrochemical Society*, 1968, **115**, 642.

4 J. Garcia Sole, L. E. Bausa and D. Jaque, *An Introduction to the Optical Spectroscopy of Solids*, John Wiley and Sons, 2005.

5 Y. Lin, Z. Tang and Z. Zhang, *Materials Letters*, 2001, **51**, 14.

6 F. Clabau, X. Rocquefelte, S. Jobic, P. Deniard, M. H. Whangbo, A. Garcia and T. Le Mercier, *Chemistry of Materials*, 2005, **17**, 3904.

7 F. Clabau, X. Rocquefelte, T. Le Mercier, P. Deniard, S. Jobic and M.-H. Whangbo, *Chemistry of Materials*, 2006, **18**, 3212.

8 J. Hölsä, T. Laamanen, M. Lastusaari, J. Niittykoski and P. Novák, *Journal of Rare Earths*, 2009, **27**, 550.

9 M. Buijs, A. Meyerink and G. Blasse, *Journal of Luminescence*, 1987, **37**, 9.

10 A. Nag and T. R. N. Kutty, *Journal of Alloys and Compounds*, 2003, **354**, 221.

11 A. Nag and T. R. N. Kutty, *Materials Research Bulletin*, 2004, **39**, 331.

12 M. Capron, F. Fayon, D. Massiot and A. Douy, *Chemistry of Materials*, 2003, **15**, 575.

13 M. L. Capron and A. Douy, *Journal of the American Ceramic Society*, 2002, **85**, 3036.

14 A. Douy and M. Capron, *Journal of the European Ceramic Society*, 2003, **23**, 2075.

15 D. Wang, Q. Yin, Y. Li and M. Wang, *Journal of the Electrochemical Society*, 2002, **149**, H65.

16 J. Niittykoski, T. Aitasalo, J. Holsa, H. Jungner, M. Lastusaari, M. Parkkinen and M. Tukia, *Journal of Alloys and Compounds*, 2004, **374**, 108.

17 J. T. C. Van Kemenade and G. P. F. Hoeks, 1983.

18 M. G. Eskin, MSc Thesis, Sabanci University, 2011.

19 G. Inan Akmehmet, S. Sturm, L. Bocher, M. Kociak, B. Ambrozic and C. W. Ow-Yang, submitted to Journal of the American Ceramic Society.

20 P. Stadelmann, *Lausanne: Interdisciplinary Centre for Electron Microscopy*, 2012.

21 C. T. Koch, PhD thesis, Arizona State University, 2002.

22 H. Rietveld, *Journal of Applied Crystallography*, 1969, **2**, 65.

23 A. Belsky, M. Hellenbrandt, V. L. Karen and P. Luksch, *Acta Crystallographica Section B: Structural Science*, 2002, **58**, 364.

24 C. W. Ow-Yang, 2014.

25 B. H. Toby, *Powder Diffraction*, 2006, **21**, 67.

26 C. K. Chang, L. Jiang, D. L. Mao and C. L. Feng, *Ceramics International*, 2004, **30**, 285.

27 D. Dutczak, C. Ronda, T. Jüstel and A. Meijerink, *The Journal of Physical Chemistry A*, 2014, **118**, 1617.

28 T. Nadezhina, E. Pobedimskaya and N. Belov, *Kristallografiya*, 1976, **21**, 826.

29 B. Smets, J. Rutten, G. Hoeks and J. Verlijsdonk, *Journal of the Electrochemical Society*, 1989, **136**, 2119.
30 G. Blasse, *Journal of Solid State Chemistry*, 1986, **62**, 207.
31 R. D. Shannon, *Acta Crystallographica Section A: Crystal Physics, Diffraction, Theoretical and General Crystallography*, 1976, **32**, 751.
32 K. Momma and F. Izumi, *Journal of Applied Crystallography*, 2011, **44**, 1272.
33 S. D. Findlay, N. Shibata and Y. Ikuhara, *Theory for Annular Bright Field STEM Imaging," Scanning Transmission Electron Microscopy of Nanomaterials Basics of Imaging and Analysis*, Imperial College Press, London, 2015.
34 S. D. Findlay, N. Shibata, H. Sawada, E. Okunishi, Y. Kondo and Y. Ikuhara, *Ultramicroscopy*, 2010, **110**, 903.
35 D. Wang, M. Wang and G. Lü, *Journal of Materials Science*, 1999, **34**, 4959.
36 T. Nakamura, K. Kaiya, N. Takahashi, T. Matsuzawa, M. Ohta, C. Rowlands, G. Smith and P. Riedi, *Physical Chemistry Chemical Physics*, 2001, **3**, 1721.
37 D. Wang, Y. Li, Q. Yin and M. Wang, *Journal of the Electrochemical Society*, 2005, **152**, H15.
38 S. H. M. Poort and G. Blasse, *Journal of Luminescence*, 1997, **72–74**, 247.
39 M. Nazarov, M. G. Brik, D. Spassky, B. Tsukerblat, A. Nor Nazida and M. N. Ahmad-Fauzi, *Journal of Alloys and Compounds*, 2013, **573**, 6.
40 T. Aitasalo, J. Holsa, H. Jungner, M. Lastusaari and J. Niittykoski, *Journal of Luminescence*, 2001, **94**, 59.
41 I. Chen and T.-M. Chen, *Journal of Materials Research*, 2001, **16**, 644.
42 T. Aitasalo, P. Dereń, J. Hölsä, H. Jungner, J. C. Krupa, M. Lastusaari, J. Legendziewicz, J. Niittykoski and W. Stręk, *Journal of Solid State Chemistry*, 2003, **171**, 114.
43 E. Nakazawa, Y. Murazaki and S. Saito, *Journal of Applied Physics*, 2006, **100**, 113.
44 L. F. Zagonel, S. Mazzucco, M. Tencé, K. March, R. Bernard, B. Laslier, G. Jacopin, M. Tchernycheva, L. Rigutti, F. H. Julien, R. Songmuang and M. Kociak, *Nano Letters*, 2011, **11**, 568.
45 J. Holsa, T. Aitasalo, H. Jungner, M. Lastusaari, J. Niittykoski and G. Spano, *Journal of Alloys and Compounds*, 2004, **374**, 56.
46 P. Blanc, A. Baumer, F. Cesbron, D. Ohnenstetter, G. Panczer and G. Rémond, in *Cathodoluminescence in Geosciences*, eds. M. Pagel, V. Barbin, P. Blanc and D. Ohnenstetter, Springer Berlin Heidelberg, 2000, DOI: 10.1007/978-3-662-04086-7_5, ch. 5, pp. 127.
47 V. Abbruscato, *Journal of the Electrochemical Society*, 1971, **118**, 930.
48 W. Jia, H. Yuan, L. Lu, H. Liu and W. Yen, *Journal of Luminescence*, 1998, **76**, 424.
49 M. Kamada, J. Murakami and N. Ohno, *Journal of Luminescence*, 2000, **87–89**, 1042.
50 Y. T. Chiang, D. P. Birnie and W. D. Kingery, *Physical Ceramics*, John Wiley&Sons, 1997.
51 I.-C. Chen and T.-M. Chen, *Journal of Materials Research*, 2001, **16**, 1293.
52 L. A. Garvie, A. J. Craven and R. Brydson, *American Mineralogist*, 1995, **80**, 1132.
53 W. Schreyer, U. Wodara, B. Marler, F. Seifert and J.-L. Robert, *European Journal of Mineralogy*, 2000, **12**, 529.

54 R. Egerton, *Reports on Progress in Physics*, 2009, **72**, 016502.
55 L. Garvie and P. R. Buseck, *American Mineralogist*, 1999, **84**, 946.
56 M. A. Gülgün, S. Šturm, R. M. Cannon and M. Rühle, *International Journal of Materials Research*, 2008, **99**, 1324.
57 M. Peiteado, S. Sturm, A. Caballero and D. Makovec, *Acta Materialia*, 2008, **56**, 4028.
58 V. Uluç, MSc Thesis, Sabanci University, 2008.
59 H. Sauer, R. Brydson, P. N. Rowley, W. Engel and J. M. Thomas, *Ultramicroscopy*, 1993, **49**, 198.